Lille University

Doctoral School 104 – Science of the Matter, of the Radiation, and of the Environment

Doctoral Thesis

by

Daria STEPANIUK

to obtain the degree of

Doctor of Lille University

Discipline: Physical, analytical and theoretical chemistry

Molecular dynamic simulation of structural- electronic characteristics and spectral properties of dyes and solutions based on them for DSSC

Date of Defense 6 March

Taras	**BRYK** *Professor, Institute for Condensed Matter Physics of NASU (Ukraine)*	**Referee**
Francesca	**INGROSSO** *Associate professor, HDR, University of Lorraine*	**Referee**
Abdenacer	**IDRISSI** *Professor, University of Lille*	**Supervisor**
François-Alexandre	**MIANNAY** *Assistant professor, HDR, University of Lille*	**Co-supervisor**
Oleg	**KALUGIN** *Professor, V.N.Karazin Kharkiv National University (Ukraine)*	**Co-supervisor**
Olexandr	**KYRYCHENKO** *Professor, V.N.Karazin Kharkiv National University (Ukraine)*	**President jury**
Emeline	**DUDOGNON** *Assistant professor, University of Lille*	**Examinator**
Kamil	**POLOK** *Assistant professor, University of Warsaw (Poland)*	**Examinator**

Université Lille

Ecole Doctorale 104 – Sciences de la Matiére, du Rayonnement, et de l'Environment

Thése de Doctorat

par

Daria STEPANIUK

pour l'obtention du titre de

Docteur de l'Université de Lille

Discipline: Chimie physique, analytique et théorique

Simulation de la dynamique moléculaire des caractéristiques structurelles et électroniques et des propriétés spectrales des colorants utilisés dans les cellules solaires

Soutenue le 6 Mars devant le jury:

Taras	**BRYK** *Professeur, Institut de physique de la matière condensée du NAS d'Ukraine (Ukraine)*	**Rapporteur**
Francesca	**INGROSSO** *Maîtresse de conférences, HDR, Université de Lorraine*	**Rapporteur**
Abdenacer	**IDRISSI** *Professeur, Université de Lille*	**Directeur de thèse**
François-Alexandre	**MIANNAY** *Maître de conférences, HDR, Université de Lille*	**Co-directeur de thèse**
Oleg	**KALUGIN** *Professeur, Université nationale de Kharkiv V. N. Karazin (Ukraine)*	**Co-directeur de thèse**
Olexandr	**KYRYCHENKO** *Professeur, Université nationale de Kharkiv V. N. Karazin (Ukraine)*	**Président du jury**
Emeline	**DUDOGNON** *Maîtresse de conférences, Université de Lille*	**Examinateur**
Kamil	**POLOK** *Maître de conférences, Université de Varsovie (Pologne)*	**Examinateur**

ACKNOWLEDGEMENTS

My deepest gratitude is indeed due to my supervisors, Professor Abdenacer IDRISSI, Professor Oleg KALUGIN, Professor François-Alexandre MIANNAY for their patience, scientific experience and fruitful discussions during all the work.

The first part of work was performed at the my alma mater V. N. Karazin Kharkiv National University (Ukraine). My special thanks to the colleagues from the V. N. Karazin Kharkiv National University: to professor Volodymyr IVANOV and professor Serhii KOVALENKO for the help in creation the library of molecules and the discussion according the results in the first part and Olexander KORSUN for the help in quantum chemistry calculation of D205 dye. I also thank the School of Inorganic Chemistry of my alma mater for their fully support during my studies as a bachelor, master and PhD students.

The second part of work was performed at the University of Lille, Laboratory of Infrared and Raman Spectrochemistry (LASIR UMR 8516). I express my thank to this institution and its director, Dr. Hervé VEZIN, for the possibility to pursue my PhD studies here. I thank Lille University and the Erasmus+ and Moblilex program for the scholarship.

The referees of this thesis: Professor Taras BRYK and associate professor Francheska INGROSSO, and the members of the jury: assistant professor Emeline DUDOGNON, Professor Olexandr KYRYCHENKO and assistant professor Kamil POLOK are gratefully acknowledged for their extra time and effort to read this work.

I would like also to gratefully acknowledge the Biological and Chemical Research Centre of the University of Warsaw for providing computing time on the supercomputer FunK and assistant professor Kamil POLOK for the providing access to this resource.

I would like to thank for the support and understanding my friends: Olena MOSKAIEVA, Dmytro DUDARIEV, Vitalii HUKOV, Kateryna GOLOVIZNINA, Dmytro NIKOLAIEVSKYI, Darya BURTSEVA and my Kharkiv quiz team, namely Stanislav MERLIAN, Konstantin PANDORIN, Oksana LUTSENKO and Yevhenii LUPANOV. Finally, my deepest gratitude is given to my family for all their love and strength.

RESUME

L'objectif de cette thèse est d'une part d'analyser les propriétés électroniques de plusieurs modèles de colorants potentiellement utilisables dans les cellules solaires et d'autre part de caractériser l'effet du solvant sur la structure locale du colorant D205 en solution et à l'interface du TiO_2. Ces recherches ont été réalisées à l'aide de calculs de chimie quantique et de simulation de dynamique moléculaire (MD).

Dans le premier chapitre de la thèse, nous avons essayé de résoudre deux problèmes importants pour décrire et prédire les propriétés spectrales des colorants pour les DSSCs. Les géométries optimisées du colorant D205 dans l'état fondamental S0 et l'état excité S1, ont été réalisées en utilisant respectivement les méthodes DFT et TDDFT. les fonctions B3LYP and CAM-B3LYP (or M06-2X) ont été utilisées dans ce travail avec la base 6-31++G(d,p). Nous avons montré que ce niveau de calcul peut être recommandée pour la prédiction des spectres d'absorption de ces colorants. Nous avons également proposé un algorithme pour prédire de nouvelles structures moléculaires avec des paramètres spectraux électroniques améliorés et avons prédit la structure de trois nouveaux colorants pour les DSSC.

Dans la deuxième partie de la thèse, nous avons analysé l'effet de la composition du mélange de colorants D205/Acétonitrile/$BmimBF_4$. Le D205 est un colorant organique utilisé dans les cellules solaires. Pour réaliser cette analyse, nous avons effectué des calculs de chimie quantique afin de paramétrer la partie intramoléculaire du champ de force du colorant D205. Les charges décrivant l'état fondamental et l'état excité du colorant D205 ont également été déterminées tandis que les paramètres de Lennard-Jones ont été tirés de la bibliothèque OPLS(AA). Les fonctions de distribution radiales des plus proches voisins ont été utilisées pour caractériser l'environnement autour des parties donneur, accepteur, pont et chaîne butyle du colorant D205 dans les états fondamental et excité.

Dans la troisième partie de cette thèse, des simulations conjointes de dynamique moléculaire (MD) et des calculs de théorie fonctionnelle de la densité (DFT) ont été utilisés pour étudier la structure et la dynamique d'un colorant indoline D205 ancré à l'interface solide-liquide de petites nanoparticules de TiO_2 anatase en mélange avec des solvants tels que l'acétornitrile, et des liquides ioniques à base de 1-butyl-3-méthylimidazolium avec des anions hexapluorophate et trifluorométhanesulfonate. Des calculs DFT ont été effectués pour estimer la géométrie d'équilibre d'une petite nanoparticule d'anatase Ti30O62H4 et pour déduire les paramètres d'interaction pour la liaison bidentate d'un colorant D205 avec le TiO_2. L'effet de différents solvants sur la conformation du colorant D205 ancré dans l'anatase a été analysé par des simulations MD, démontrant qu'une représentation explicite du solvant est vitale pour reproduire les spectres optiques d'un colorant D205.

Mots-clés : colorants, simulation de dynamique moléculaire, structure microscopique, état excité, calcul chimique quantique, liquides ioniques

ABSTRACT

The objective of this thesis is on the one hand to analyze the electronic properties of several dye models that can potentially be used in solar cells and on the other hand to characterize the effect of the solvent on the local structure of the dye D205 in solution and at the TiO_2 interface. These investigations were carried out using quantum chemistry and molecular dynamics (MD) simulation calculations.

In the first chapter of the thesis we tried to solve two problems important for describing and predicting the spectral properties of dyes for DSSCs. It was shown that the Time-Dependent DFT (TDDFT) approximation with a combination of B3LYP and CAM-B3LYP (or M06-2X) functionals with the 6-31++G(d,p) basis set can be recommended for the prediction of dye absorption spectra. We also proposed an algorithm to predict new molecular structures with improved electron spectral parameters and predicted the structure of three new dyes for DSSC.

In the second part of the thesis we analyzed the effect of the composition of the D205/Acetonitrile/$BmimBF_4$ dye mixture. D205 is an organic dye used in solar cells. To perform this analysis, we performed quantum chemical calculations to parameterize the intramolecular part of the D205 dye force field. The charges describing the ground state and excited state of the D205 dye were also determined while the Lennard-Jones parameters were taken from the OPLS(AA) library. Radial nearest neighbor distribution functions were used to characterize the environment around the donor, acceptor, bridge and butyl chain moieties of the D205 dye in the ground and excited states.

In the third part of this thesis joint molecular dynamics (MD) simulations and density functional theory (DFT) calculations were used to study the structure and dynamics of an indoline dye D205 anchored at the solid-liquid interface of small TiO_2 anatase nanoparticles in admixture with solvents such as acetornitrile , and 1-butyl-3-methylimidazolium-based ionic liquids with hexapluorophate and trifluoromethanesulfonate anions. DFT calculations were performed to estimate the equilibrium geometry of a small $Ti_{30}O_{62}H_4$ anatase nanoparticle and to deduce the interaction parameters for the bidentate bonding of a D205 dye with TiO2. The effect of different solvents on the conformation of the anatase-anchored D205 dye was analyzed by MD simulations, demonstrating that an explicit solvent representation is vital to reproduce the optical spectra of a D205 dye.

Keywords: dyes, molecular dynamics simulation, microscopic structure, excited state, quantum chemical calculation, ionic liquids.

Contents

LIST OF ABBREVIATIONS

ADF	angular distribution function
AN	acetonitrile
Bmim$^+$	1-*n*-butyl-3-methylimidazolium
DFT	density functional theory
DSSC	dye sensitized solar cells
HOMO	highest occupied molecular orbital
IL	ionic liquid
LJ	Lennard-Jones
LR.	Linear response
LUMO	lowest unoccupied molecular orbital
MD	molecular dynamics
MO	molecular orbital
NNA	nearest neighbor aproach
PBC	periodic boundary conditions
PES	potential energy surface
PME	Particle-Mesh-Evald
RDF	radial distribution function
RTIL	room temperature ionic liquid
SS	State specific
TDDFT	time dependent density functional theory
TFO$^-$	trfluoromethylsulfonate, triflate, $CF_3SO_3^-$

General introduction

Dye-sensitized solar cells (DSSCs) based on π-conjugated organic dyes covalently anchored on the TiO_2 surface have many attractive characteristics, such as high solar energy conversion efficiency and low cost of the components [1-8]. Dye-sensitizers are the most important component in DSSCs because they affect key processes that regulate energy conversion efficiency, such as light absorption, charge injection, dye regeneration, and charge recombination, respectively[5, 9, 10]. Therefore, the rapid development of DSSC technologies requires constant tuning of the chemical properties of organic dyes since the light conversion efficiency is largely determined by the photophysics of the dye [1].

Indoline-based dyes is a promising class of free-metal dyes for various applications due to their photophysical and photochemical properties. They exhibit high photon-to-current conversion efficiency combined with high molar absorption coefficients and quantum yields [11-14]. The D205 dye was built according to the scheme Donor – π-bridge – Acceptor [15, 16]. Several studies suggest that the sensitizing efficiency of the D205 dye can be enhanced by chemical binding to the active layer of the TiO_2 semiconductor [17, 18].

In addition to proper dye-TiO_2 interface design, the DSSC performance is also affected by the environment. Due to the standing out properties of ionic liquids (ILs), such as low vapor pressure, high conductivity, non-combustibility, chemical and thermal stability, ILs have become good electrolytes, capable of passivating the active surfaces of DSSC devices [19]. With the aim to reduce the viscosity of the electrolyte the polar molecular solvent (e.g. AN) is commonly added to the DSSC.

However, understanding the microstructure of the liquid/electrode interface requires studies of the interaction between the electrolyte and the electrode surface at the atomic level.

Current quantum chemical approaches especially time-dependent extension of the density functional theory (TDDFT) can provide a theoretical basis for describing most of the properties of individual dye molecule or dye-surface components, such as dye geometry, optical absorption spectra, and semiconductor bandgap [10, 20-23]. However, accurate prediction of the absorption spectra and solvatochromic shifts of organic dyes in liquid media and attached to the TiO_2 surface and solvated by polar liquids is still a challenging task. On the other hand, the solvent-induced conformational changes of the dye molecule due to the nature of the solvent, dye aggregation, and specific hydrogen-bonded interactions with solvent molecules must also be correctly accounted for [24-26].

The classical molecular dynamics (MD) simulation is a powerful computational instrument to investigate microscopic environment of a dye in the bulk and within the solvent/surface interfaces, which can guide rational dye design and save synthetic and experimental resources[27-31]. Moreover, MD simulations can complement the experimental results of the conformational dynamics and spectroscopic properties of the dye anchored to TiO_2[19]. However, the local structure of the D205 dye in the mixture of ILs with molecular polar solvent as well as the phenomena and mechanisms related to the interaction between TiO_2 and dye have not been well studied, especially at the microscale and nanoscale levels.

Accordingly, the objectives of this thesis were formulated as following:

(i) first, to analyze the existing quantum chemical approaches and develop an algorithm capable to predict new molecular structures of the dyes with improved electron spectral parameters for DSSC application;

(ii) to investigates the effect of the composition of the acetonitrile/$BmimBF_4$ mixtures on the local environment of D205 dye in the ground and excited state;

(iii) to study the structure and dynamics of the D205 dye anchored at the solid-liquid interface of small TiO_2 anatase nanoparticles in admixture of acetonitrile with $Bmim^+$-based ionic liquids.

Organization of the thesis

In this thesis the complex theoretical investigation of π-conjugated organic dyes in mixture and on the TiO_2 has provided. The discussion of the obtained results organized as follows.

Chapter 1 presents the proposition of the algorithm for the predicting dyes structures with the desired properties, in particular the absorption spectra. In additional to it, the validation of the existing quantum chemical method (semi-empirical and TDDFT ones) to calculate the electronic properties of dyes was provided.

The force field parametrization of indoline dye D205 with the further MD simulation in $BmimBF_4$/AN mixture is provided in Chapter 2. Radial distribution function, corresponding nearest neighbor distribution functions and coordination numbers were used to characterize the environment around the donor, acceptor, bridge and chain moieties of the D205 dye in the ground and excited states.

Chapter 3 is focused on behavior D205 on TiO_2. There is the joint MD simulation and DFT study D205 dye anchored at the solid-liquid interface of TiO_2 solvated with AN provided. As well the effect of the various environments, such as 1-butyl-3-methylimidazolium-based ionic liquids with hexapluorophophate and trifluoromethanesulfonate anions and acetonitrile on the microscopic structure and dynamics of a D205 dye bonded covalently into the TiO_2-anatase surface were examined by using MD simulations in terms of radial distribution function.

Finally, conclusions, summarizing the key findings of the work, and future perspectives are outlined.

References for general introduction

1. Fan, W., et al., *Computational study of diketopyrrolopyrrole-based organic dyes for dye sensitized solar cell applications.* Journal of Molecular Graphics and Modelling, 2015. **57**: p. 62-69.
2. Prachumrak, N., et al., *Improvement of D–π–A organic dye-based dye-sensitized solar cell performance by simple triphenylamine donor substitutions on the π-linker of the dye.* Materials Chemistry Frontiers, 2017. **1**(6): p. 1059-1072.
3. Selvaraj, A.R.K. and S. Hayase, *Molecular dynamics simulations on the aggregation behavior of indole type organic dye molecules in dye-sensitized solar cells.* Journal of Molecular Modeling, 2012. **18**(5): p. 2099-2104.
4. Suzuka, M., et al., *A Quasi-Solid State DSSC with 10.1% Efficiency through Molecular Design of the Charge-Separation and -Transport.* Sci Rep, 2016. **6**: p. 28022.
5. Cao, D., et al., *Enhanced Performance of the Dye-Sensitized Solar Cells with Phenothiazine-Based Dyes Containing Double D−A Branches.* Organic Letters, 2011. **13**(7): p. 1610-1613.
6. Cheng, H.-M. and W.-F. Hsieh, *High-efficiency metal-free organic-dye-sensitized solar cells with hierarchical ZnO photoelectrode.* Energy & Environmental Science, 2010. **3**(4): p. 442-447.
7. Grätzel, M., *Dye-sensitized solar cells.* Journal of Photochemistry and Photobiology C: Photochemistry Reviews, 2003. **4**(2): p. 145-153.
8. Gratzel, M., *Photoelectrochemical cells.* Nature, 2001. **414**(6861): p. 338-344.
9. Ambade, S.B., et al., *Indoline-dye immobilized ZnO nanoparticles for whopping 5.44% light conversion efficiency.* Journal of Photochemistry and Photobiology A: Chemistry, 2011. **222**(2–3): p. 366-369.
10. Barone, V., et al., *Fluorescence spectra of organic dyes in solution: a time dependent multilevel approach.* Physical Chemistry Chemical Physics, 2011. **13**(6): p. 2160-2166.
11. El-Zohry, A.M., D. Roca-Sanjuán, and B. Zietz, *Ultrafast Twisting of the Indoline Donor Unit Utilized in Solar Cell Dyes: Experimental and Theoretical Studies.* The Journal of Physical Chemistry C, 2015. **119**(5): p. 2249-2259.
12. Huang, L., L. Jiang, and M. Wei, *Metal-free indoline dye sensitized solar cells based on nanocrystalline Zn2SnO4.* Electrochemistry Communications, 2010. **12**(2): p. 319-322.
13. Ito, S., et al., *High-conversion-efficiency organic dye-sensitized solar cells with a novel indoline dye.* Chemical Communications, 2008(41): p. 5194-5196.
14. Kim, J.Y., Y.H. Kim, and Y.S. Kim, *Indoline dyes with various acceptors for dye-sensitized solar cells.* Current Applied Physics, 2011. **11**(1): p. S117-S121.
15. Dessì, A., et al., *D–A–π–A organic dyes with tailored green light absorption for potential application in greenhouse-integrated dye-sensitized solar cells.* Sustainable Energy & Fuels, 2021. **5**(4): p. 1171-1183.
16. Liu, P., et al., *Novel and Stable D–A−π–A Dyes for Efficient Solid-State Dye-Sensitized Solar Cells.* ACS Omega, 2017. **2**(5): p. 1812-1819.
17. Archana, J., M. Navaneethan, and Y. Hayakawa, *Solvothermal growth of high surface area mesoporous anatase TiO2 nanospheres and investigation of dye-sensitized solar cell properties.* Journal of Power Sources, 2013. **242**: p. 803-810.
18. Li, N., et al., *Operando Study of Structure Degradation in Solid-State Dye-Sensitized Solar Cells with a TiO2 Photoanode Having Ordered Mesopore Arrays.* Solar RRL, 2022. **6**(9): p. 2200373.
19. Kuang, D., et al., *Organic Dye-Sensitized Ionic Liquid Based Solar Cells: Remarkable Enhancement in Performance through Molecular Design of Indoline Sensitizers.* Angewandte Chemie International Edition, 2008. **47**(10): p. 1923-1927.

20. Jacquemin, D., et al., *TDDFT Performance for the Visible Absorption Spectra of Organic Dyes: Conventional versus Long-Range Hybrids.* Journal of Chemical Theory and Computation, 2008. **4**(1): p. 123-135.
21. Kacimi, R., et al., *Theoretical design of D-π-A system new dyes candidate for DSSC application.* Heliyon, 2021. **7**(6): p. e07171.
22. Le Bahers, T., et al., *A TDDFT investigation of ground and excited state properties in indoline dyes used for dye-sensitized solar cells.* Phys Chem Chem Phys, 2009. **11**(47): p. 11276-84.
23. Nazeeruddin, M.K., et al., *Combined Experimental and DFT-TDDFT Computational Study of Photoelectrochemical Cell Ruthenium Sensitizers.* Journal of the American Chemical Society, 2005. **127**(48): p. 16835-16847.
24. El-Zohry, A., A. Orthaber, and B. Zietz, *Isomerization and Aggregation of the Solar Cell Dye D149.* J Phys Chem C Nanomater Interfaces, 2012. **116**(50): p. 26144-26153.
25. Monti, S., et al., *Theoretical Investigation of Adsorption, Dynamics, Self-Aggregation, and Spectroscopic Properties of the D102 Indoline Dye on an Anatase (101) Substrate.* The Journal of Physical Chemistry C, 2016. **120**(5): p. 2787-2796.
26. Oliveira, C.S., et al., *Solvent and concentration effects on the visible spectra of tri-para-dialkylamino-substituted triarylmethane dyes in liquid solutions.* Spectrochim Acta A Mol Biomol Spectrosc, 2002. **58**(13): p. 2971-82.
27. Barone, V., et al., *Fluorescence spectra of organic dyes in solution: a time dependent multilevel approach.* Phys Chem Chem Phys, 2011. **13**(6): p. 2160-6.
28. Graen, T., M. Hoefling, and H. Grubmüller, *AMBER-DYES: Characterization of Charge Fluctuations and Force Field Parameterization of Fluorescent Dyes for Molecular Dynamics Simulations.* J Chem Theory Comput, 2014. **10**(12): p. 5505-12.
29. Martins, L., et al., *Solvation dynamics of coumarin 153 in dimethylsulfoxide-water mixtures: Molecular dynamics simulations.* The Journal of Chemical Physics, 2003. **118**: p. 5955-5963.
30. Sánchez-de-Armas, R., et al., *Real-Time TDDFT Simulations in Dye Sensitized Solar Cells: The Electronic Absorption Spectrum of Alizarin Supported on TiO2 Nanoclusters.* Journal of Chemical Theory and Computation, 2010. **6**(9): p. 2856-2865.
31. Selvaraj, A.R. and S. Hayase, *Molecular dynamics simulations on the aggregation behavior of indole type organic dye molecules in dye-sensitized solar cells.* J Mol Model, 2012. **18**(5): p. 2099-104.

Chapter 1. Quantum-chemical methods for prediction of the spectral properties of dyes and virtual screening

The material presented in this chapter is based on the publication:

1. Ivanov, V., Trostianko, P., Kovalenko, S., Volodchenko, A., Chernozhuk, T., Stepaniuk, D., & Kalugin, O. (2021). Quantum-chemical calculations of electronic spectra absorption: ab initio or semiempirical methods?. *Kharkiv University Bulletin. Chemical Series*, (36), 33-43. https://doi.org/10.26565/2220-637X-2021-36-06

In order to predict the spectral properties of organic dyes for solar cells the series of the calculations of the typical π-conjugate systems with various structural fragments, have been performed.

A significant discrepancy in the estimations of electronic excitations is demonstrated by the density functional theory for the different functionals. It is concluded that TDDFT calculations should be performed by using both B3LYP and CAM-B3LYP (or M06-2X) functionals with the basis set 6-31++G(d,p). It was found that semi-empirical approaches especially π-electron method PPP/CIS and all valence method ZINDO/S can provide adequate estimates of excitation energies of π-conjugated dyes for moderate computer resources.

With the help of method CAM-B3LYP and using different basis set the spectral properties of indoline dye D205 were calculated. It was shown that using State Specific (SS) or Linear responce (LR) PCM model for describing spectral properties of the D205 molecule in AN media are far from the experimental results. Only the basis sets with the diffusion orbitals can predict the shape of absorption spectra, which consist of 2 bands.

An attempt was made to build a systematic procedure for the selection / prediction of organic π-conjugate molecules with certain parameters of the electronic structure suitable for DSSC application. More than four thousands of π-conjugated compounds were generated by using benzene, oxazole, oxadiazole, thiophene and coumarin fragments with nitro-, methoxy-, dimethylamino- and diethylamino-groups as substitutes. The careful screening by using semi-empirical methods (PPP/CIS and ZINDO/S) followed by application of TDDFT methods with B3LYP and CAM-B3LYP functionals allowed us to deduce the relation between structure and spectral properties of the dyes and predict for the first time a new promising candidates for DSSC application.

1.1. Introduction

Considering the unlimited variety of molecular structures based on organic dyes, the development of methods for forecasting their spectral properties based on their structure is an important problem. The modern state of computer technology has brought computational chemistry to new heights. Today, a multifaceted theoretical study of various systems from atoms and molecules to complex complexes including "heavy" transition elements has become possible. The arsenal of theoretical methods available to chemists includes a wide variety of approaches from the construction of empirical statistical "structure-property" laws to the methods of molecular dynamics and quantum chemistry. In particular, the methods of quantum chemistry, implemented in many popular computer programs, can provide valuable information about the geometry of the ground state, charge distribution, characteristics of reactivity, etc.

However, calculations of excited states remain a difficult problem today. This especially applies to theoretical studies of electronic excitations (UV and visible spectroscopy) of rather large organic π-conjugated dyes, which may include a significant number of non-hydrogen atoms, including carbon, nitrogen, oxygen, sulfur, etc. Dyes, built on the scheme of Donor(D)–π-bridge-Acceptor(A) are attracted the huge attention like an alternative for the Ru-complexes dyes for using in DSSC due to their easily tuning optical properties (thanks to the possibility change the different parts of dye to obtained the necessary properties), high molar extension coefficient [15, 16, 21, 22, 30, 32, 33].

Density functional theory (TDDFT) [34] is usually used to calculate different properties of such molecules. Dozens of TDDFT functionals are implemented in the popular quantum chemical packages Gaussian [35] and GAMESS[36]. Of course, the presence of a large number of TDDFT functionals, different in nature, also poses a problem of choice. Fortunately, the well-known B3LYP functional [36, 37] and hybrid meta exchange-correlation functionals of the M06 class[38] are largely show the high accuracy in studies of the ground state of molecules.

At the same time, current studies showed that the accuracy of the description of electronic excitations within the TDDFT frameworks is not always satisfactory ([37]). Meantime, it should be emphasized that, unlike ground state calculations, choosing a functional to describe electronic excitations is not a simple problem. In particular, it was shown that even calculations of valence and Rydberg excitations for certain molecules require different functionals [23, 39, 40]!

Therefore, the choice of a DFT functional, and even a quantum chemical method, for calculations of excited states is an open problem. This problem is especially acute when there is a need for "virtual screening" of dyes, which is implemented on databases that include hundreds of thousands of molecules, from which it is necessary to select several hits with given spectral properties. It is clear that in this case computationally expensive *ab initio* methods are not applicable. Simpler calculation schemes are needed, which also include semi-empirical methods. To justify the use of such approximate methods, it would be interesting to conduct a comparative analysis of the results of various approaches that have been developed to date.

Screening of libraries of molecules, to identify such structures that would have given properties, is intensively used in modern chemistry [41-44]. Usually, this procedure is used to find "hits" of compounds that correspond to a pharmacophore in the problem of finding structures with a certain bioactivity[44, 45]. In this chapter, an attempt was made to build a systematic procedure for the selection of organic conjugated molecules with certain parameters of the electronic structure. Finding such compounds is a key point in a number of molecular electronics tasks, in particular, in the development of dye-sensitized solar cells. In this case, the most important parameters are the absorption wavelength at the maximum intensity (λ, nm), the absorption intensity parameter (oscillator strength, f).

Thus, the purpose of this chapter is to choose quantum-chemical TDDFT method and PCM model, which can accurately describe the spectral properties of organic π-conjugated dyes. In addition, an attempt to build the procedure of finding hits, suitable for DSSC application was performed.

1.2. The choosing of the method for quantum chemical calculation

1.2.1. Calculations of electronic absorption spectra

To clarify the possibilities of quantum-chemical methods in the problem of describing the electron absorption spectra (EAS) of π-conjugated systems, we used a number of approaches that cover a significant part of the available approximations. However here it should be noted that the problem of describing the spectral properties of conjugated systems in general, and organic dyes in particular, is divided into two significantly different parts. The first one of them consists in choosing such a quantum-chemical approach that is capable of adequately describing the system in a vacuum (or gas phase). The obvious complexity of such a study is connected with the lack of a sufficient amount of experimental data. The second problem is an adequate description of the system in the environment. It should be noted that polarization-continuum approaches (PCM) [46, 47], which are usually used to describe the non-specific effects of solvatochromism, are too model-based and, generally speaking, do not guarantee a strict correspondence to any real spectroscopic experiment.

Taking into account the above mentioned factors, in the presented work a number of approaches were used that make up a certain hierarchy of quantum-chemical approximations, for which appropriate models for taking into account the non-specific effects of solvatochromism were implemented. In particular, the following methods were selected.

1. The semi-empirical Pariser-Parr-Pople method with account of configuration interaction (PPP/CI) is a fairly simple approach to the description of spectra within the framework of the π-electron approximation. Standard averaged bond lengths and angles characteristic of conjugated systems are used to describe the geometry in the PPP/CI calculation [48, 49]. The electronic parameters of the PPP Hamiltonian are tabulated values.

2. ZINDO/S [50] is the full valence semi-empirical method, which is focused on the description of absorption spectra. But the method is not adapted to geometry optimization in the ground state. Thus, it is first necessary to optimize the geometry of the ground state, for example, by using the AM1 method, or using standard force fields of molecular mechanics (Python module rdkit [51] allows this to be done). Only then one can calculate the spectrum using the ZINDO/S method.

3. Full valence semi-empirical method AM1 in combination with CIS (AM1/CI) represents a more consistent calculation scheme than the previous one. After all, a single parameterization is used for both the ground and excited states. AM1/CI is a definite alternative to the ZINDO/S method.

4. Time-dependent DFT (TDDFT) calculations with functionals found in contemporary spectral studies: B3LYP, CAM-B3LYP, M06-2X, PBE1PBE, wB97XD. A brief description of the functionals can be found for instance in [52]. For TDDFT calculations we used basis set of atomic orbitals - 6-31++G(d,p).

This part presents the experimental and calculated results of electronic absorption spectra (hereinafter) of some typical π-conjugated systems (Fig. 1.1), which are usually the components of the effective dyes and phosphors. These molecules were chosen due to small size to reduce the computational time for the calculations and for all them there are the experimental data in different solvents are available to comparing.

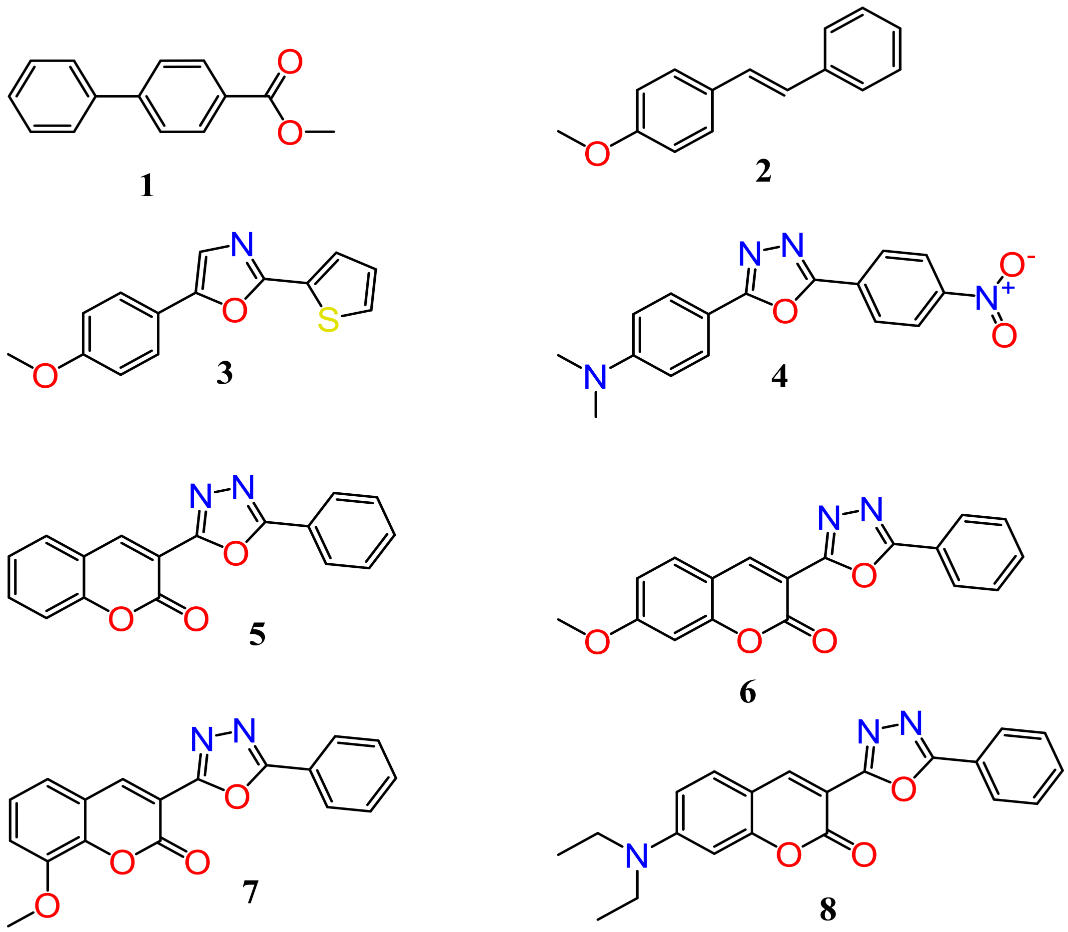

Figure 1.1. The structures of the analyzing dyes: methyl [1,1'-biphenyl]-4-carboxylate (1), 1-methoxy-4-[(E)-2-phenylethenyl]benzene (2), 5-(4-methoxyphenyl)-2-(thiophen-2-yl)-1,3-oxazole (3), N,N-dimethyl-4-[2-(4-nitrophenyl)-1,3-oxazol-5-yl]aniline (4), 3-(2-phenyl-1,3-oxazol-5-yl)-2H-1-benzopyran-2-one (5), 7-methoxy-3-(2-phenyl-1,3-oxazol-5-yl)-2H-1-benzopyran-2-one (6), 8-methoxy-3-(2-phenyl-1,3-oxazol-5-yl)-2H-1-benzopyran-2-one (7), 7-(diethylamino)-3-(2-phenyl-1,3-oxazol-5-yl)-2H-1-benzopyran-2-one (8).

In the given compounds, the donor groups are represented by methoxy-, diethylamino- and N,N-dimethyl. In the compounds 5-8 coumarin is π-conjugate bridge, while the benzene is acceptor part.

The results of preliminary calculations of absorption wavelengths are given in Table 1.1. The TDDFT method is represented by two functionals - B3LYP and CAM-B3LYP, which, according to the previous studies, give certain limits of theoretical estimates of absorption spectra. Results of calculations corresponding to molecules in vacuum are compared with available experimental values for systems in different solvents to present the overall picture. Of course, experimental data obtained in a solvent and calculations of systems in a vacuum (even for different levels of theory) cannot be directly compared in absolute terms.

Table 1.1. Results of absorption wavelength calculations (nm, vacuum) in comparison with available experimental data for these systems. Experimental data for dyes were taken from [53]. For TDDFT calculation, 6-31++G(d,p) basis set was used.

№	**PPP/CIS**	**AM1/CIS**	**ZINDO/S**	**B3LYP**	**CAM-B3LYP**	**Exp** [53]
1	305	336	291	282	253	270 (**AN**)
2	327	277	324	334	301	302 (heptan)
3	330	414	430	359	313	330 (toluene)
4	380,	418,	412,	511,	339,	390
	306	346	313	333	269	307 (toluene)
5	360	410	415	380	322	349 (**AN**)
6	364	428	420	381	329	362 (**AN**)
7	327	416	413	377	322	330 (**AN**)
8	382	449	436	400	351	426 (**AN**)

Table 1.2. shows the linear correlation between each of the semi-empirical methods with all used TDDFT method. The comparison between theoretical results with the experimental ones provide as well.

Table 1.2. Correlation coefficients (R) and standard deviations (SD) of absorption wavelengths (semi-empirical methods – TDDFT – experiment). For TDDFT calculations, 6-31++G(d,p) basis set was used.

Semi-empirical	TDDFT	R	SD (nm)
PPP/CIS	B3LYP	0.81	50
PPP/CIS	CAM-B3LYP	0.90	34
PPP/CIS	Exp.	0.93	–
AM1/CIS	B3LYP	0.78	53
AM1/CIS	CAM-B3LYP	0.72	86
AM1/CIS	Exp	0.77	–
ZINDO/S	B3LYP	0.66	48
ZINDO/S	CAM-B3LYP	0.91	78
ZINDO/S	Exp	0.90	–
B3LYP	Exp	0.78	–
CAM-B3LYP	Exp	0.90	–

The data presented in the table 1.1. shows that the approximate semi-empirical schemes PPP/CIS and ZINDO/S correspond quite well to the results of the TDDFT calculation. Thus, the correlation coefficients (Table 1.2) are quite large for PPP/CIS – TDDFT.

At the same time, the values of standard deviations (SD), although reveal noticeable deviations of λ_{max} absorption. It demonstrates the suitability of estimates by the PPP/CI and ZINDO/S methods. The AM1/CIS method exhibits slightly worse agreement with TDDFT results and experimental data. In general, it is noticeable that the ZINDO/S and AM1/CI methods significantly overestimate the absolute values of λ_{max}. Since the λ_{max} absorption data is correspond to the system in the solvent, and the calculated values correspond to the vacuum, we do not indicate the SD as a characteristic of the absolute "theory-experiment" deviation.

Analysis of the table 1.2 also demonstrated a certain drawback of the B3LYP method for molecule 4, which is a system with pronounced charge transfer. Here, the overestimation of the absorption wavelengths for the two bands is associated with unbalanced inclusion of long-range Coulomb effects [16]. However, it has already been noted that the CAM-B3LYP method corrects this problem. Indeed, according to the presented data (Table 1.1 and Table 1.2), CAM-B3LYP gives the best agreement with the experimental data and with the PPP/CIS and ZINDO/S methods. At the same time, the closest to the experimental λ_{max} absorption data were found in the PPP/CI method.

1.2.2. Solvatochromism of the dyes with π-conjugation

Another important issue is PCM estimations of solvato- and fluorochromy of π-systems. Despite the long history, which begins with the works of Onsager and Kirkwood [54] and continues in the works of Tomasi, Menucci, and others.[46, 47, 55], this problem is still far from being solved. Starting from PCM estimates of the equilibrium solvation of the ground state of the molecule, spectral transitions can be described as processes with non-equilibrium solvation conditions. Among a number of approaches for describing non-equilibrium solvation, currently two main approaches used [56]. The method of linear response (LR) makes it possible to estimate directly the excitation energies of the system. In the State Specific (SS) method, the energy of the system in a certain excited state is calculated by taking into account the self-consistent charge distribution with the reactive field. It should be noted that SS calculation is formally more correct. However, since the PCM calculations are only model calculations, which approach (LR or SS) will be closer to the experimental data is an open question. It is also worth to note that the LR calculation is much simpler and requires significantly less computer resources than the SS method. It is believed that the theory should be sufficient in procedures for finding dyes with the necessary LR parameters. However, this issue still needs detailed investigation. The tables 1.3 and 1.4 provide the comparison between the results, obtained for the selected structures in different solvents. For this analysis and comparison the molecules 5, 6 and 8 were chosen because they consist of the same cumarine-derivative fragment (5 molecule) and for obtaining molecule 6 and 8 there are just different substituent in the same position are added.

Table 1.3. Calculation of the absorption wavelength (nm) of π-systems taking into account the effects of the environment within the framework of the LR-model and SS model in cyclohexane. For TDDFT calculations, 6-31++G(d,p) basis set was used.

Cyclohexane	**CAM-B3LYP**		**M06-2X**		**Experimental**
	LR	**SS**	**LR**	**SS**	
5	328	322	327	321	350
6	335	329	335	329	
8	368	366	364	363	415

From the presented tables it is clear, that the results obtained with both methods are close to each other, but still quite far from the experimental data. Therefore, the LR approach is used for further calculations due to its simplicity and computation time and recourses saving.

Table 1.4. Calculation of the absorption wavelength (nm) of π-systems taking into account the effects of the environment within the framework of the LR-model and SS model in acetonitrile. For TDDFT calculations, 6-31++G(d,p) basis set was used.

Acetonitrile	**CAM-B3LYP**		**M06-2X**		**Experimantal**
	LR	SS	LR	SS	
5	325	315	316	307	323; 339, 342
6	330	326	334	328	362
8	373	380	370	378	433

In the next part, within the framework of LR, using a number of TDDFT functionals, the λ_{max} absorption estimates were made for compounds 5-8 in various environments (Table 1.5) utilizing the method from the previous part.

According to the data in table 1.5 for acetonitrile, the obtained results generally characterize the B3LYP and CAM-B3LYP methods well. It can also be seen that the realistic results for the given functionals lie between the B3LYP and CAM-B3LYP functionals. The M06-2X results are quite close to CAM-B3LYP. At the same time, the B3LYP functional sometimes gives overestimates, while CAM-B3LYP gives slightly underestimated estimates. Thus, it can be expected that the values will be closer to the experimental data on average. The PBE1PBE functional falling into this interval ($\lambda_{\mathrm{B3LYP}} - \lambda_{\mathrm{CAM-B3LYP}}$) gives a fairly good match to the experimental data. The wB97XD functional gives too low absorption wavelengths. Interestingly, for system 5, the calculations of λ in the CAM-B3LYP method turn out to be close to each other, on average, within 2 nm, which corresponds to the experimental data. Although the ZINDO/S method gives obviously overestimates of the absorption wavelengths, it reproduces the relative shifts quite well.

Table 1.5. The absorption wavelength (nm) of π-systems taking into account the effects of the environment within the framework of the LR-model. For TDDFT calculations, 6-31++G(d,p) basis set was used.

No	Media	ZINDO /S	B3LYP	CAM-B3LYP	M06-2X	PBE1 PBE	wB97 XD	Exp
5	Vacuum	415	379	322	320	346	319	–
	CH	451	385	328	322	369	322	328 349
	THF	444	380	326	318	360	313	324 343
	AN	438	376	324	318	361	322	322 341
	DMSO	443	378	326	317	357	311	263 346
6	Vacuum	420	381	329	327	366	324	–
	CH	462	384	338	333	375	334	–
	AN	450	381	337	331	368	331	362
7	Vacuum	413	376	322	320	361	320	–
	CH	377	381	327	325	366	325	–
	AN	372	374	324	322	360	306	330
8	Vacuum	435	400	351	348	386	346	–
	CH	484	418	367	364	402	360	415 420
	AN	489	423	376	377	410	369	426

1.2.3. Spectral properties of D205

With the goal to check the proposed approach, the indoline – derivative D205 dye was chosen (figure 1.2).

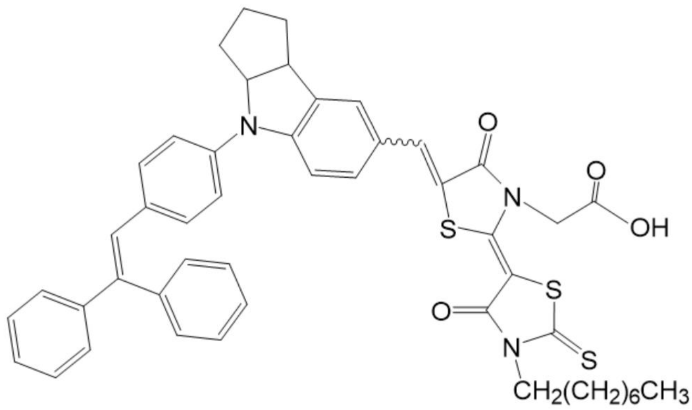

Figure 1.2. Structural formula of dye D205

On the table 1.7. the calculated the absorption wavelength maximum on different level of theory and solvation model are presented.

Table 1.7. Calculation of the absorption wavelength (nm) of D205 in vacuum and in AN with LR and SS approaches

Level of theory	Wavelength, nm	Level of theory	Wavelength, nm
CAM-B3LYP/6-31G	518	CAM-B3LYP/6-31++G(d,p)	386; 541
CAM-B3LYP/6-311G	527	CAM-B3LYP/6-31++G(d,p) in AN LR	432; 576
CAM-B3LYP/6-31G(d,p)	510	CAM-B3LYP/6-31++G(d,p) in AN SS	347; 450
CAM-B3LYP/6-311++G(d,p)	378; 540		

In the work [57] was shown, that these is 2 maximum for spectrum in acetonitrile: 390 nm and 525 nm. The table shows that the results, obtained for both LR and SS approaches are far from experimental one. It means, that the calculation of spectrum of D205 in polar solvent does not well describe the spectral properties. However, there is the second peak appears in basis set with the diffuse functions on heavy atoms and hydrogen, so these results are in good agreement with the shape of spectrum. Meanwhile, the increasing of electronic level splitting from 2 to 3 not improve the results. The results obtained in vacuum on the level of theory CAM-B3LYP/6-311G are close to the spectrum in solvent, like cyclohexane with the small dielectric constant of this solvent (2.02) and equal to 527 nm and 524 nm respectively. [57]

1.3. The virtual screening of π-conjugated systems

The virtual screening is the computation procedure of looking over the set of molecules aiming to search for those with certain physical and chemical properties. This set can consist of both existing molecules as well as designed in silico. The last approach allows to perform the physical synthesis and laboratory analysis only of the promising candidates.

The semi-automatic procedure has been developed to create a library of chemical compounds from the initial set of molecular fragments (see fig. 1.2) was proposed by professor V. Ivanov, V.N. Karazin Kharkiv National University. This set includes a number of π-conjugated molecular units like oxazole, oxadiazole, thiophene, several heterocycles and coumarin fragments to be used for generation of a large number of compounds. As not all of these “molecules” are chemically meaningful or can be synthesized (due to restrictions or the difficulty of the procedure), a specially developed semi-automatic algorithm of initial fragments sequential joining was utilized. It significantly reduces a number of possible output compounds restricting by the chemical sense. Figure 1.3 depicts the sketch of the π-conjugated compound construction procedure. The active positions of these molecules are indicated on fig. 1.3, chosen from structural and chemical considerations. For the obtained systems, the geometry optimization was carried out utilizing molecular mechanics methods. Totally, the library at our disposal contains about four thousand entities, which are formed by various structural fragments, in various combinations.

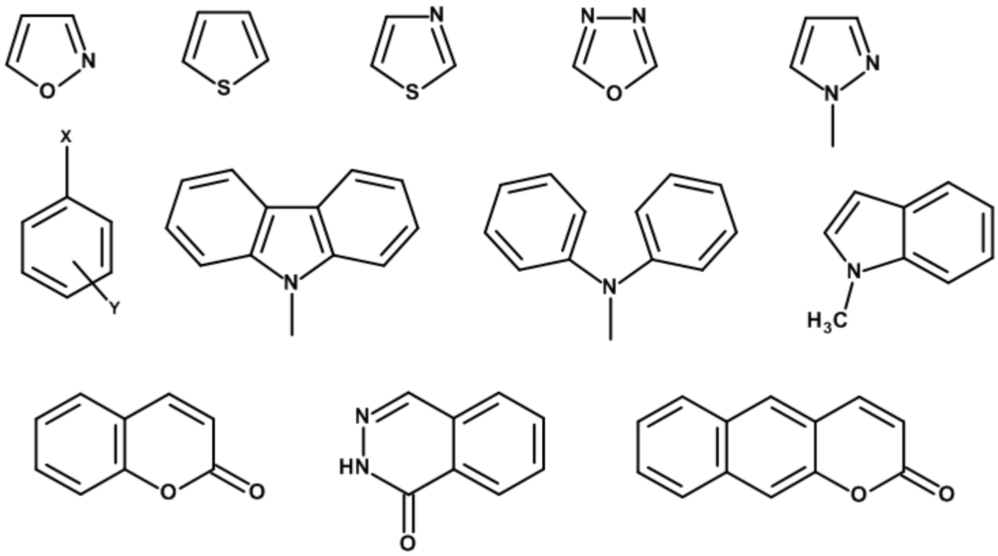

Figure 1.3. Molecular fragments which have been used for the construction of dyes.

Preliminary screening using the PPP method for absorption spectra calculations gave the following picture of the determined set of molecules distribution over their λ_{max} absorption (Fig. 1.5).

In order to identify the most suitable structures, a preliminary calculation of the absorption wavelength of π-conjugated systems was carried out using semi-empirical methods (the PPP/CI [48, 49] and ZINDO/S [50]. For further geometry optimization at semi-empirical quantum chemistry level, we used AM1 method[58]. After it the results were compared with the TDDFT methods. In the table 1.1. was shown that the results, obtained with the semi-emperical methods are close to the TDDFT ones, so it is possible to use them for the for primary selection.

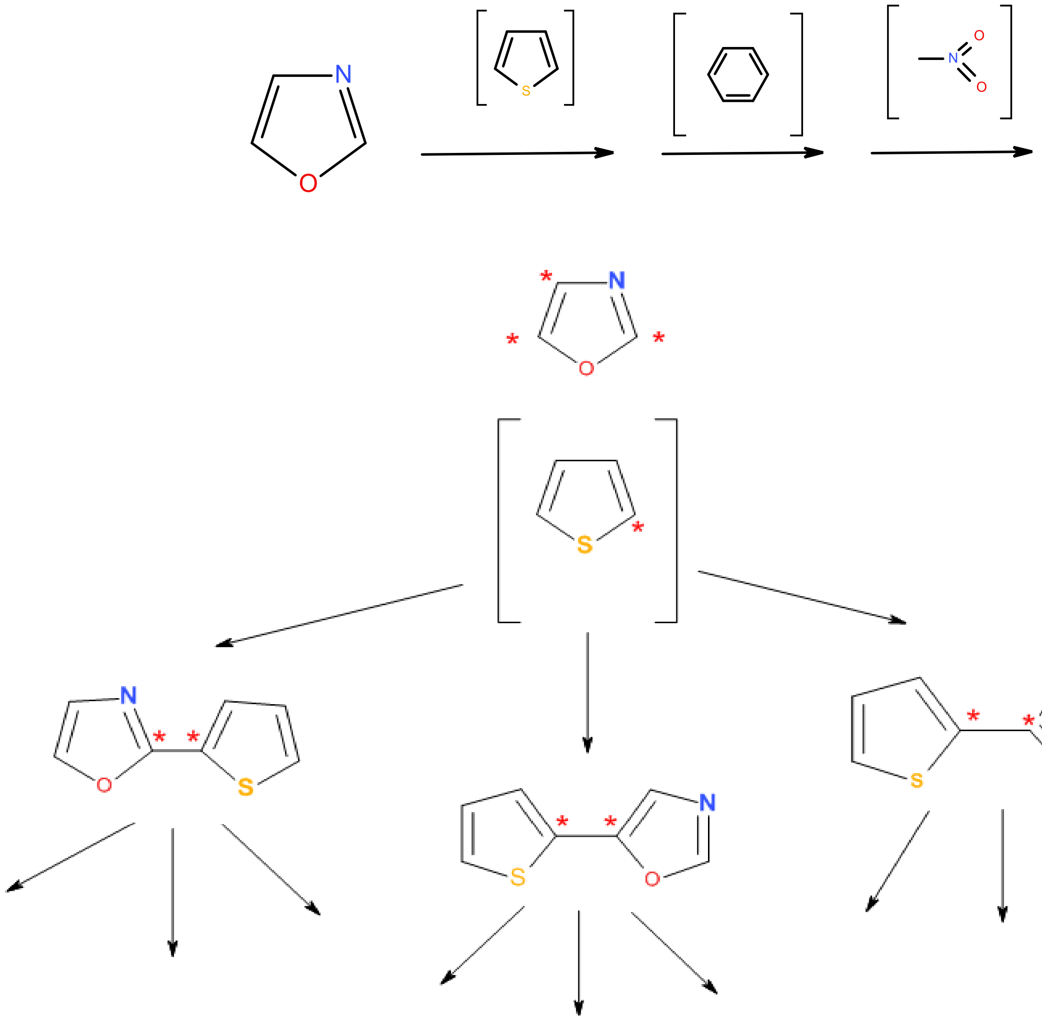

Figure 1.4. Scheme of formation of π-conjugated compounds from the initial set of fragments.

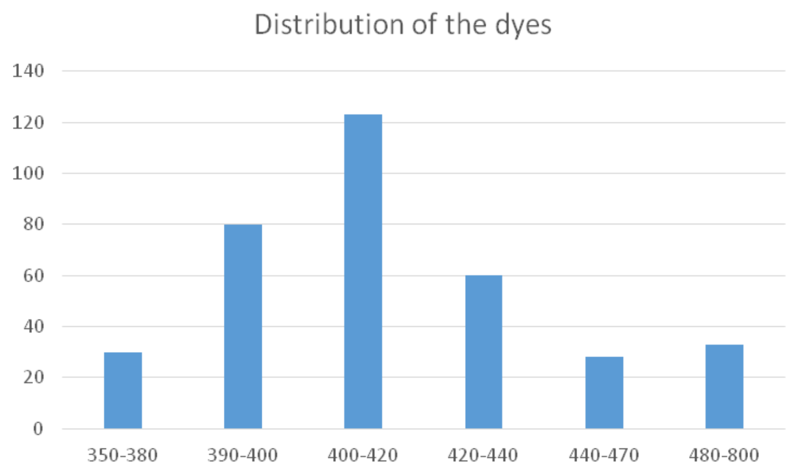

Figure 1.5. Histogram of distribution of molecules by absorption wavelength (nm).

After checking the methodology and screening a number of promising candidates was proposed. It was noticed that it is possible to generate the structure of dyes by using only four typical molecular fragments (Fig. 1.6). Such fragments are widely used as components of organic dyes and luminophores.

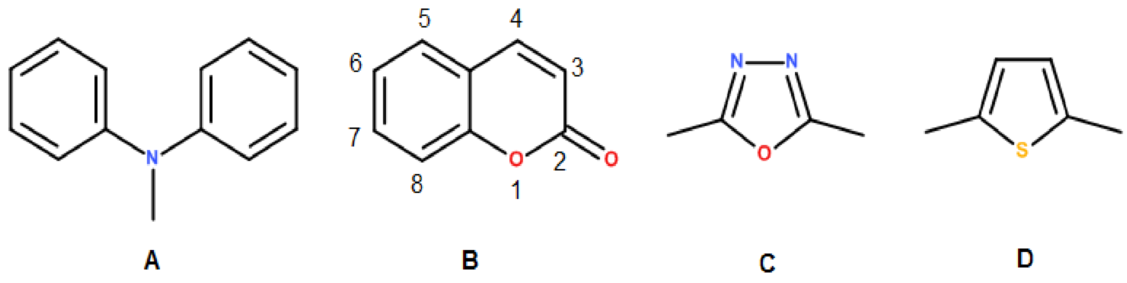

Figure 1.6. Molecular fragments for automated generation of dyes.

For instance diphenylamine (structure A) present a structure that is common to a set of organic dyes. Among them the Metanil Yellow, Disperse Orange, Acid Orange *etc*. Diphenylamine was treated as a strong π-donor substituent with wide conjugated system. The coumarin molecule (structure B) is an aromatic compound which intensively used as active laser dyes and sensitizer in DSSC. Of course for the structure B one can suppose a large number of different substituents in different position of molecule. However from practical point of view the most interesting are linear (non branched) structures with definite, clearly pronounced, donor-acceptor character. This why the restriction existed on only double substituted structures which designated as nBm. Numbers n and m are corresponding positions of coumarin (see Fig. 1.6, B). The structures C (oxadiazole) and D (tiophene) are also popular components of dyes and luminophores (see for instance [53]). In addition, to be used in DSSC the anchoric group (e.g. COOH-) should be presented as well.

Combinatorial generation of possible chain structures based on fragments A-B-C-D can be enumerated (see table 1.8). Question mark – there is no exact data about the possibility to synthesis this structure.

Table 1.8. Possible structures which generated from molecular fragments from Fig. 1.6, where the “?” – there is no exact information about the possibility of synthesis.

Chain	Steric effects filter	Possibility of synthesis
A-5B4-C-D	–	–
A-5B3-C-D	?	?
A-6B5-C-D	–	–
A-6B4-C-D	?	?
A-6B3-C-D	A-6B3-C-D	A-6B3-C-D
A-7B6-C-D	–	–
A-7B5-C-D	?	?
A-7B4-C-D	A-7B4-C-D	?
A-7B3-C-D	A-7B3-C-D	A-7B3-C-D
A-8B3-C-D	A-8B3-C-D	?
....	....	....

From initially generated structures a number structures are correspond to sterically difficult structures. These structures removed from consideration. Finally, only several structures (“hits”) were selected by the group of Prof. Kovalenko (Department of Organic Chemistry of V. N. Karazin Kharkiv National Uinversity) as perspective for synthetic work (Fig. 1.7). Corresponding wavelength for these dyes provided in table 1.9.

From table 1.9 one can note that, that the increasing of the number of thiophene rings (Ia-Ib-Ic) has effect on the bathochromic shift and the maximum transfer from 397 nm for 1 ring to 424 nm for three of them. Changing the thiophene ring to phenil decreases the wavelength of the maximum.

(I)

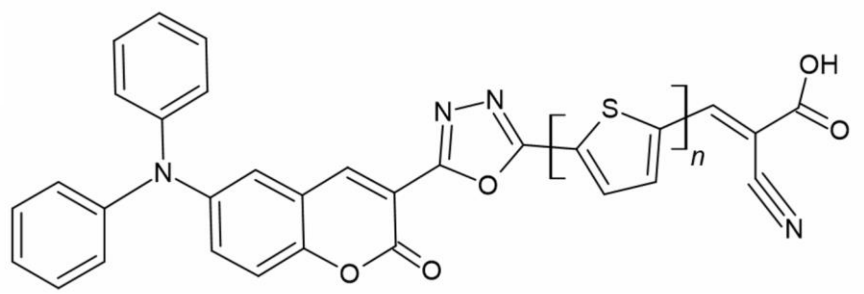

(II)

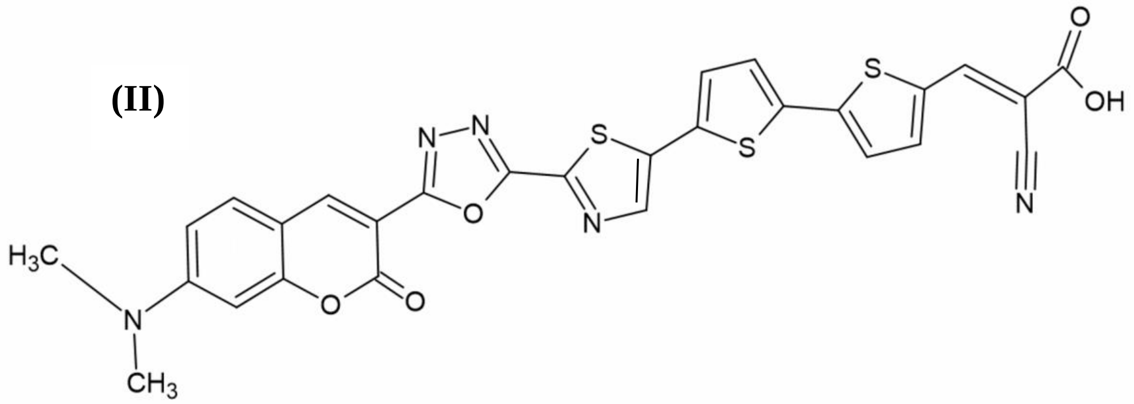

(III)

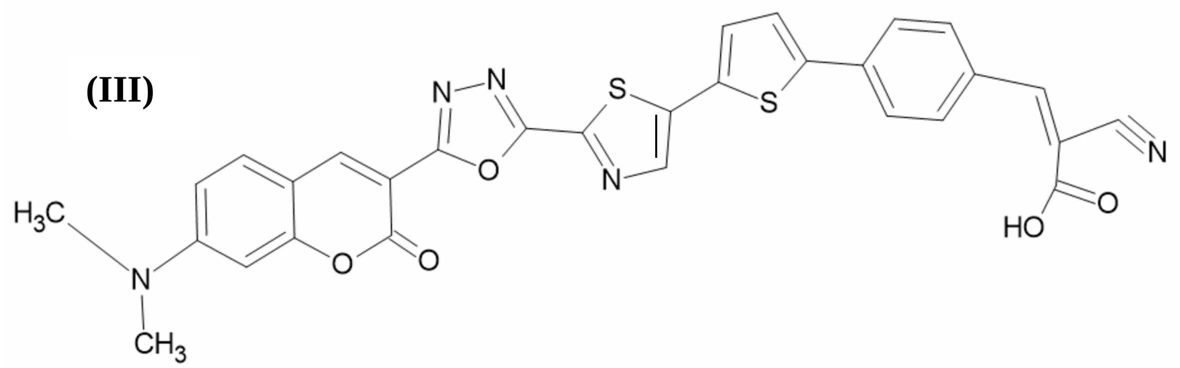

Figure 1.7. The promising structures of dyes **I (a,b,c), II, III:** E)-2-cyano-3-(5-(5-(6-(diphenylamino)-2-oxo-2H-chromen-3-yl)-1,3,4-oxadiazol-2-yl)thiophen-2-yl)acrylic acid (Ia, n=1); (E)-2-cyano-3-(5'-(5-(6-(diphenylamino)-2-oxo-2H-chromen-3-yl)-1,3,4-oxadiazol-2-yl)-[2,2'-bithiophen]-5-yl)acrylic acid (Ib, n=2); (E)-2-cyano-3-(5''-(5-(6-(diphenylamino)-2-oxo-2H-chromen-3-yl)-1,3,4-oxadiazol-2-yl)-[2,2':5',2''-terthiophen]-5-yl)acrylic acid (Ic, n=3); (E)-2-cyano-3-(5'-(2-(5-(7-(dimethylamino)-2-oxo-2H-chromen-3-yl)-1,3,4-oxadiazol-2-yl)-4,5-dihydrothiazol-5-yl)-[2,2'-bithiophen]-5-yl)acrylic acid (II); (Z)-2-cyano-3-(4-(5-(2-(5-(7-(dimethylamino)-2-oxo-2H-chromen-3-yl)-1,3,4-oxadiazol-2-yl)-4,5-dihydrothiazol-5-yl)thiophen-2-yl)phenyl)acrylic acid (III)

Table 1.9. Absorption wavelengths (λ, nm) and oscillator strength of the "hits" molecules obtained at the M06-2X/6-31++G(d,p) level of theory

Structure	n	λ(nm)	Oscillator strength
Ia	1	397	1.856
Ib	2	410	2.201
Ic	3	424	2.556
II		418	2.02
III		376	1.768

1.4. Conclusions

Despite the wide range of available quantum chemical methods, calculations of electronic excitations of organic π-systems (in particular, dyes) remain a rather difficult problem. Quantitative estimates of such parameters as absorption wavelength and corresponding intensities are still far from ideal for a number of reasons. The results presented in this chapter showed that well-known semi-empirical approaches allow to describe spectral transitions with accuracy comparable with the TDDFT theory, but they are much less computation and time consuming. In particular, in a situation where it is necessary to carry out virtual screening, the PPP/CI and ZINDO methods can provide the necessary information at the cost of a small computer resources.

According to our estimates, it makes sense to use three functionals with the basis set 6-31++G(d,p) in TDDFT calculations of π-conjugated systems. Namely, the results of the B3LYP and CAM-B3LYP (M06-2X) methods give the upper and lower limits of the absorption wavelength, respectively.

With the help of selected CAM-B3LYP method the absorption spectra of indoline dye D205 was calculated both in vacuum and AN PCM model in terms of LR and SS methods. It was established that only the basis sets with the diffusion orbitals can reproduce the experimental shape of absorption spectrum with 2 band, while the increasing of electronic level splitting from 2 to 3 not improve the results.

As a results of scanning the library of π-conjugated dyes the 6 promising candidates was proposed. All these molecules consist of coumarin fragment. It was shown that the maximum of the absorption spectrum increases with the increase of the amount of thiophene rings.

1.5. References for Chapter 1

1. Xia, H.-Q., et al., *Design of D–A–π–A organic dyes with different acceptor and auxiliary acceptor for highly efficient dye-sensitized solar cells: a computational study*. RSC Advances, 2014. **4**(92): p. 50338-50350.
2. Dessì, A., et al., *D–A–π–A organic dyes with tailored green light absorption for potential application in greenhouse-integrated dye-sensitized solar cells.* Sustainable Energy & Fuels, 2021. **5**(4): p. 1171-1183.
3. Kacimi, R., et al., *Theoretical design of D-π-A system new dyes candidate for DSSC application.* Heliyon, 2021. **7**(6): p. e07171.
4. Le Bahers, T., et al., *A TDDFT investigation of ground and excited state properties in indoline dyes used for dye-sensitized solar cells.* Phys Chem Chem Phys, 2009. **11**(47): p. 11276-84.
5. Liu, P., et al., *Novel and Stable D–A−π–A Dyes for Efficient Solid-State Dye-Sensitized Solar Cells.* ACS Omega, 2017. **2**(5): p. 1812-1819.
6. Sánchez-de-Armas, R., et al., *Real-Time TDDFT Simulations in Dye Sensitized Solar Cells: The Electronic Absorption Spectrum of Alizarin Supported on TiO2 Nanoclusters.* Journal of Chemical Theory and Computation, 2010. **6**(9): p. 2856-2865.
7. Srinivas, K., et al., *D-π-A organic dyes with carbazole as donor for dye-sensitized solar cells.* Synthetic Metals, 2011. **161**(1): p. 96-105.
8. Selsby, R.G., C. Machin, and M.L. Hernandez, *A semi-empirical MO theory for ionization potentials and electron affinities.* International Journal of Quantum Chemistry, 1977. **11**(1): p. 149-161.
9. Frisch, M.J., et al., *Gaussian 16 Rev. C.01*. 2016: Wallingford, CT.
10. Barca, G.M.J., et al., *Recent developments in the general atomic and molecular electronic structure system.* The Journal of Chemical Physics, 2020. **152**(15): p. 154102.
11. Leang, S.S., F. Zahariev, and M.S. Gordon, *Benchmarking the performance of time-dependent density functional methods.* The Journal of Chemical Physics, 2012. **136**(10): p. 104101.
12. Silva-Junior, M.R., et al., *Benchmarks for electronically excited states: Time-dependent density functional theory and density functional theory based multireference configuration interaction.* The Journal of Chemical Physics, 2008. **129**(10): p. 104103.
13. Lambert, C., et al., *Characterization of high-performance organic dyes for dye-sensitized solar cell: a DFT/TDDFT study.* Canadian Journal of Chemistry, 2016. **94**(12): p. 1109-1118.
14. Nazeeruddin, M.K., et al., *Combined Experimental and DFT-TDDFT Computational Study of Photoelectrochemical Cell Ruthenium Sensitizers.* Journal of the American Chemical Society, 2005. **127**(48): p. 16835-16847.
15. Patil, M.K., M.G. Kotresh, and S.R. Inamdar, *A combined solvatochromic shift and TDDFT study probing solute-solvent interactions of blue fluorescent Alexa Fluor 350 dye: Evaluation of ground and excited state dipole moments.* Spectrochimica Acta Part A: Molecular and Biomolecular Spectroscopy, 2019. **215**: p. 142-152.
16. Ackloo, S., et al., *CACHE (Critical Assessment of Computational Hit-finding Experiments): A public–private partnership benchmarking initiative to enable the development of computational methods for hit-finding.* Nature Reviews Chemistry, 2022. **6**(4): p. 287-295.
17. Maity, N., et al., *Effect of the Mixture Composition of BmimBF4–Acetonitrile on the Excited-State Relaxation Dynamics of a Solar-Cell Dye D149: An Ultrafast Transient Absorption Study.* The Journal of Physical Chemistry C, 2021. **125**(32): p. 17841-17852.

18. McCloskey, K., et al., *Machine Learning on DNA-Encoded Libraries: A New Paradigm for Hit Finding.* Journal of Medicinal Chemistry, 2020. **63**(16): p. 8857-8866.
19. Yan, X.C., et al., *Augmenting Hit Identification by Virtual Screening Techniques in Small Molecule Drug Discovery.* Journal of Chemical Information and Modeling, 2020. **60**(9): p. 4144-4152.
20. Cheeseright, T., et al., *Molecular field technology applied to virtual screening and finding the bioactive conformation.* Expert Opinion on Drug Discovery, 2007. **2**(1): p. 131-144.
21. Mennucci, B., et al., *How the environment controls absorption and fluorescence spectra of PRODAN: a quantum-mechanical study in homogeneous and heterogeneous media.* J Phys Chem B, 2008. **112**(2): p. 414-23.
22. Tomasi, J., B. Mennucci, and R. Cammi, *Quantum Mechanical Continuum Solvation Models.* Chemical Reviews, 2005. **105**(8): p. 2999-3094.
23. Ohno, K., *Some remarks on the Pariser-Parr-Pople method.* Theoretica chimica acta, 1964. **16**: p. 247-248.
24. Pople, J.A., *Electron interaction in unsaturated hydrocarbons.* Transactions of the Faraday Society, 1953. **49**(0): p. 1375-1385.
25. Da Motta Neto, J.D. and M.C. Zerner, *New parametrization scheme for the resonance integrals (Hμν) within the INDO/1 approximation. Main group elements.* International Journal of Quantum Chemistry, 2001. **81**(3): p. 187-201.
26. *RDKit: Open-source cheminformatics*. Available from: http://www.rdkit.org.
27. Mardirossian, N. and M. Head-Gordon, *Thirty years of density functional theory in computational chemistry: an overview and extensive assessment of 200 density functionals.* Molecular Physics, 2017. **115**(19): p. 2315-2372.
28. Krasovitsky B.M., A.L.M., *Preparative chemistry of organic phosphors*. 1997, Kharkiv: Folio. 205.
29. Kirkwood, J.G., *Theory of Solutions of Molecules Containing Widely Separated Charges with Special Application to Zwitterions.* The Journal of Chemical Physics, 1934. **2**(7): p. 351-361.
30. Mennucci, B., *Continuum Solvation Models: What Else Can We Learn from Them?* The Journal of Physical Chemistry Letters, 2010. **1**(10): p. 1666-1674.
31. Caricato, M., *A comparison between state-specific and linear-response formalisms for the calculation of vertical electronic transition energy in solution with the CCSD-PCM method.* The Journal of Chemical Physics, 2013. **139**(4): p. 044116.
32. Smortsova, Y., *Thèse de Yevheniia Smortsova*. 2018, Université de Lille,.
33. Ivanov V., S.L., *Quantum Chemistry*. 2007, Kharkiv: Folio.

Chapter 2. Force field parametrization and the local structure of D205 in $BmimBF_4$/AN mixture

The photophysical properties of the dyes, e.g. the position of maximum on the absorption or emission spectrum, the stoke shift depends on the composition of the mixture. For the investigation of the spectral properties experimental studies can be combined with the molecular dynamic simulations. For the theoretical studies indoline dye D205 was chosen, due to the promising efficiency.

On the first step, the parametrization of force field was done. Partial charges were calculated both in ground and excited states with the method CHelpG. The force constants for the all degree of freedom were calculated in the frame of the rigid PES scanning. MD simulation in the mixture with the different composition of Ionic liquid and molecular solvent was performed. The competition between dye, cation, anion and solvent was analyzed in the terms of nearest neighbor approach, radial distribution function and coordination numbers. It was shown that interaction between cation and anion between cation and anion of IL stronger, than with dye D205.

2.1. Introduction

Several reports were made regarding the mixture composition of the photophysical properties of several dyes. [1-9] As the physical chemical properties of the mixture such as the polarity, the viscosity, the dielectric constant as well as the hydrogen bond, dipole-dipole, π-π interactions are modulated by the change in the mixture composition, the photophysical properties of the dye are affected consequently. For instance, the position of maximum on the absorption or emission spectrum, the stoke shift, the quantum yield and the excited state relaxation times undergo a nonlinear behavior. The most striking result is that the distribution of the H^m atom of the cation methyl around the electronegative atoms of the D205 is the most affected when the charge distribution is changed from that mimicking the ground state to that of the excited state. Interestingly, this behavior is used to assess about the local organization such as microheterogeneity of the mixtures.

Considerable progress towards understanding the solvation dynamics of dyes in mixtures has been made in recent years, through molecular dynamics (MD) [1, 10-13] and quantum-chemical calculations[1, 12, 14-20]. For instance, using MD simulation the solvation dynamics of Coumarin C153 was analyzed in DMSO and water mixture spanning the entire composition range. It was shown that the solvation of C153 is predominantly determined by its interaction with the DMSO molecules, even at low 0.25 mole fraction DMSO content while the water molecules are only mildly coupled to the charge transfer in C153, resulting in a small water relaxation component. [21] In another MD study, the anomalous behavior of two alcohol−water (TBA−water and ethanol−water) binary mixtures were investigated by collecting ultrafast solvation response around the C480 dye. It was found that in a specific mole fraction of these mixtures the average solvation time rises while in the mixture of ethanol-water, this behavior is totally absent. It was suggested that the structural transition from water like tetrahedral network to zigzag alcohol like structure is the probable reason for slow solvation dynamics.[22] In another work, in order to understand the molecular reorganization and relaxation behavior of aqueous binary mixtures, the solvation dynamics of tryptophan over a wide range of DMSO concentration was studied using MD simulation. A remarkable slow-down in the solvation dynamics around 0.10-0.20 and again around 0.40-0.50 mole fraction of DMSO was observed. The authors of this paper suggest that the slowdown is a reflection of various structural transformation in water-DMSO mixture that is driven by a cooperative aggregation of DMSO molecules aided by water in the above mentioned concentration ranges. In another MD simulation work, the solvatochromism and the dynamic stokes-shift of coumarin C153 in mixtures of benzene-acetonitrile and of benzene-methanol. The MD results allowed to interpret these dynamics in benzene-acetonitrile mixtures in terms of motions of benzene around the coumarin. More interestingly, they show that the role of benzene in the solvation process of CI53 seems to be more important than usually assumed.

Furthermore, the solvation dynamics of dyes was also investigated in neat ionic liquids and in their mixtures ILs with a molecular solvent [23]. By investigating the solvation properties of solvatochromic probe dye molecules dissolved in mixtures of large number protic ionic liquids with various molecular solvents using multi-parameter solvation scales, the authors of the previously cited papers demonstrate the high solvation capability of protic ionic liquids which open the way to their use in applications which require high polarity and H bonding ability.

Experimental methods, were combined with MD simulation to investigate the solvation dynamics of 3 organic dyes (coumarine-derivative) in [pMIM][Br]/water system. It was suggested that the coumarin dyes preferably interact with the IL. [24-26] The authors investigate how the water in small concentration affect the solvation dynamics of the C153 in [HMIM][PF6] IL [27]. It was found that water screens the direct Coulombic interactions between cations and anions and that it facilitates rotational and translational motion. Furthermore, the relaxation of solvent environments to local minima is considerably faster in the presence of small amounts of water. The fact that it is possible to choose the IL that the dynamics or kinetics of relaxation of the solvent can be controlled (selected) by adjusting the absorption frequency is one of the main advantages of these systems.

Indoline-based dyes form a promising class of compounds for various applications because of their photophysical and photochemical properties. They reveal high photon-to-current efficiency in combination with high molar absorption coefficients and quantum yields [6, 14, 18, 28-40]. One of particularly intriguing applications of these molecules is the photosensitive dyes in dye-sensitized solar cells (DSSCs) [30, 41]. In these devices, molecular dyes are typically used in the mixtures of IL and molecular solvents, described below. The photophysics in the system of indoline derivated dyes in molecular solvents (MS) and in IL/MS mixtures, making use of the favorable properties of both, MSs and ILs was also investigated[42-44]. For this purpose, these mixtures were investigated using the spectroscopic properties of four indoline derivates (D131, D102, D149 and D205) dyes encompassing steady-state UV-vis absorption and fluorescence spectroscopy and time-resolved spectroscopy for understanding the photophysics of these dyes and its mixture composition dependence. It was shown that the solvation dynamics is crucial for the excited state dynamics of the dyes. Furthermore, the obtained relaxation times values, that describe the relaxation of these dye from the excited state to the ground, were found to decrease with dilution of the ionic liquid and the slowest one among them go through a minimum around 0.1 mole fraction of the ionic liquid. This interpreted as an indication of the the presence of different specific and non-specific interactions between the dye and the surrounding mediums.

Furthermore, the solvation of the indoline dyes was also investigated at the interface e.g TiO_2 [6, 7, 45-49]. It was shown that D205 with the longer alkyl chains shows larger mobility and consequently higher diffusion coefficient than

D149 dye with shorter alkyl chain. In the work [50] the combined solvatochromic shift and TDDFT study of ground and excited state was performed for Alexa Fluor 350 dye in various solvents like alcohols and some general ones. It was shown that if dipole moment of solute increases during the excitation, a positive solvatochromism normally observed. The value of Stokes shift varies with the solvent polarity as evidenced by the considerable change of geometry of dye in excited state upon electronic transition. It might be influenced by solvent parameters like hydrogen bond donor and acceptor and solvent polarity. With the help of experimental study the group [51] show that the behavior of the dye is dictated by solute–solvent and solvent–solvent interactions, which are effected by the solvent polarity.

It should be mentioned that in the investigation of the solvation dynamics of dyes using molecular dynamics simulation, the choice of the force field is crucial. To our best knowledge, forced field based on Amber library for describing dyes were reported, especially tuning the partial charges, what is extremely important for π-conjugated systems [10]. The same class of dyes, like Alexa Fluor (rhodamine-derivative), Atto (zwitterionic dyes) and Cyanine families, their force filed parameters were described on the basis of CHARMM force field with the sequential application for high accuracy diffusion coefficient, comparatively with the existed force fields [52] e.g. UFF[53], OPLS-AA[54], Amber[55], etc. The accuracy of their application for the bigger molecules is low. However, there is the lack of the investigation of the solvation dynamics of these dyes using a force filed parametrized that is specifically derived for the indoline dyes. Consequently, in this work we aim to investigate the structural properties of dye D205 (the structural formula is shown on Fig. 2.1) in the system of ionic liquid $BmimBF_4$ and molecular solvent acetonitrile (AN) using combined molecular dynamics and quantum-chemical calculations approaches. Thus, mixture was chosen because it was the previous experimental works, performed in the group[42, 44]. Due to the lack of the D205 structure experimental investigations, we chose the M06-2X quantum-chemical calculation method in basis 6-311+G(d) to optimize and calculate the force constants to describe the intramolecular part of the force field. We also derive the charge distribution in the ground and excited states. Based on this force field, molecular dynamics simulations of the mixture of the D205/BmimBF4/AN were carried out.

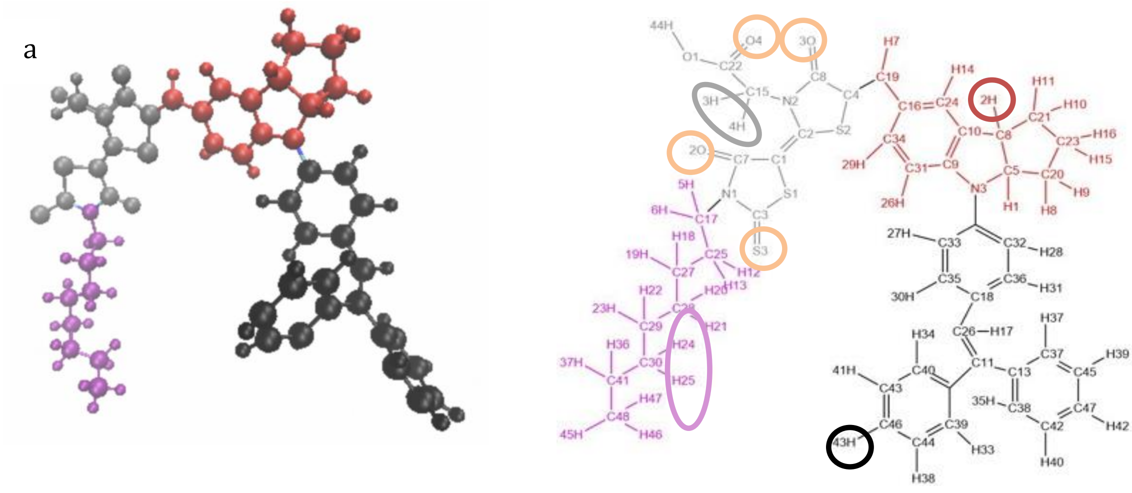

Figure 2.1. Molecule D205 (black – donor part, red – bridge, grey - acceptor part and purple – chain), b – D205 with the selected atoms for further calculations

2.2. Force Field development of D205

The force field of a polyatomic molecule is a mathematical expression that describes the dependence of the intramolecular and intermolecular potential energy of the system as a function of interatomic distances and intramolecular coordinates:

$$U = E_{\text{intra}} + E_{\text{inter}}, \tag{2.1}$$

where the first term describe the intramolecular contributions to the potential energy), and the second - intermolecular contributions.

The structure, absorption and electronic properties of the dyes and adsorption on surfaces may be affected by the isomerism of the dye molecule.[19, 45, 56] For dye D205 possible 4 isomers: dihedrals ψ_1 (C8-C4-C19-C16) and $\psi 2$ (S2-C2-C1-S1) can be in cis- and trans- positions. For all the further calculations the most energetically favorable isomer trans-trans were used (Fig 2.1).

2.2.1. Intramolecular force field of D205

The intramolecular potential energy can be described by the equation 2.2:

$$E_{\text{intra}} = U(r,\theta,\psi) = \sum_{bond}\frac{k_r}{2}(r-r_0)^2 + \sum_{angle}\frac{k_\theta}{2}(\theta-\theta_0)^2 + \sum_{dihedrals}\frac{k_\phi}{2}(\psi-\psi_0)^2, \quad (2.2)$$

where $U(r,\theta,\psi)$ is - the sum of the potential energies of the internal coordinates of the bonds, angles and dihedral angles, respectively; k-force constant; r,θ,ψ- values at a given scan step, where the index "0" corresponds to the values in the local energy minimum.

The optimal geometry was obtained under very tight optimization convergence criteria implemented in the software and tested to be true minima by the absence of imaginary frequencies in the corresponding vibration spectra. The quantum chemical calculations of a single D205 dye molecule in gas phase were carried out using M06-2X/6-311+G(d) level of theory. After that, calculations of force constants associated with the bond lengths and angles stretching were used within the concept of rigid potential energy surface (PES) scanning.[1, 57-61] Using this approach, the minimum potential energy along a given internal coordinate is calculated, without simultaneous optimization of internal degrees of freedom at each scanning step, which means, that the conformer transition is impossible.

To calculate the force constants, the dye molecule was divided into separate fragments (different colors on Fig. 2.1) to reduce the computation time. In total, 20 configurations of D205 fragments with a step of 0.0005 nm for bonds, 0.5° for angles and 0.8° for dihedral angles were analyzed with the help of rigid PES scanning. As a result of this calculation, the energy profiles obtained are well described by a second-order polynomial, which is shown on Fig 2.2. For the dihedrals the harmonic approximation was used, because the molecule is stable only for the small range of radian, so it’s better describe with the same polynomial form.

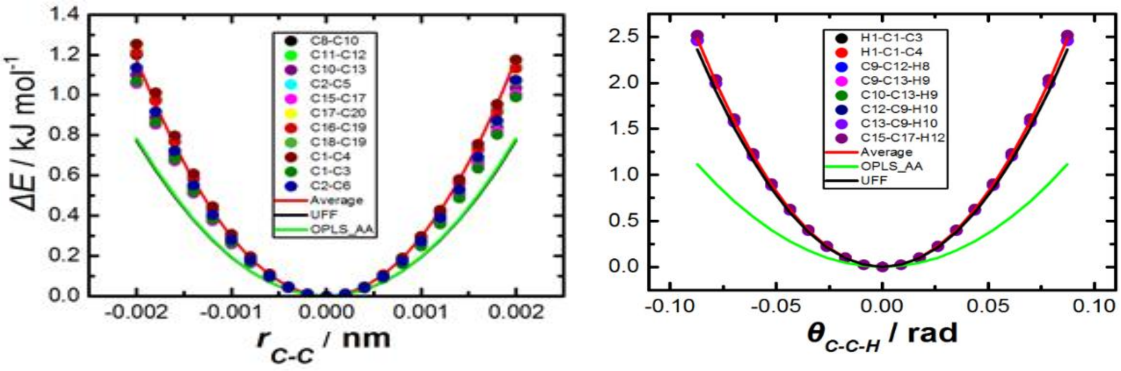

Figure 2.2. Examples of PES profiles for C-C bond (left) and C-C-H angle (right), lines – harmonic approximation from OPLS_AA[62]), UFF[53] and averaged from this work

For each atom were chosen corresponding types of atom from the field OPLS[54] and after it all force constant, as well as geometry parameters were averaged (table S1-S2) for the possibility to use it for another molecules, especially, indoline dyes. From fig 2.2 it is noticeable that corresponding constants from the standard force fields (UFF [53], OPLS-AA[62]) not in all cases correctly reproduced geometry behavior in this molecules.

2.2.2. Intermolecular force field of D205

The formula 2.3 describes the intermolecular terms.

$$E_{\text{inter}} = \sum_{LJ} 4\epsilon_{ij} \left(\frac{{\sigma_{ij}}^{12}}{{r_{ij}}^{12}} - \frac{{\sigma_{ij}}^{6}}{{r_{ij}}^{6}}\right) + \sum_{i,j} \frac{q_i q_j}{r_{ij}}\,, \qquad (2.3)$$

Where the first term describes the Lennard-Jones potential and second - Coulomb interactions.

For the current force field model of the D205 dye, data from the OPLS[54] force field was utilized for the describing Lennard-Jones parameters.

The spectral properties of the dye depend on its excited state. For the calculation the method (CHelpG) in vacuum on the M06-2X/6-311++G(d,p) level of theory was used. The schematic representation of this process is seen on the Figure 2.3. Point (1) correspond to the optimized Ground state of the dye, point

(2) is the excited state with the geometry, optimized on the ground state, (3) – excited state with the geometry, optimized on this excited state level, (4) – is transfer back to the ground state with the geometry, optimized on the excited state.

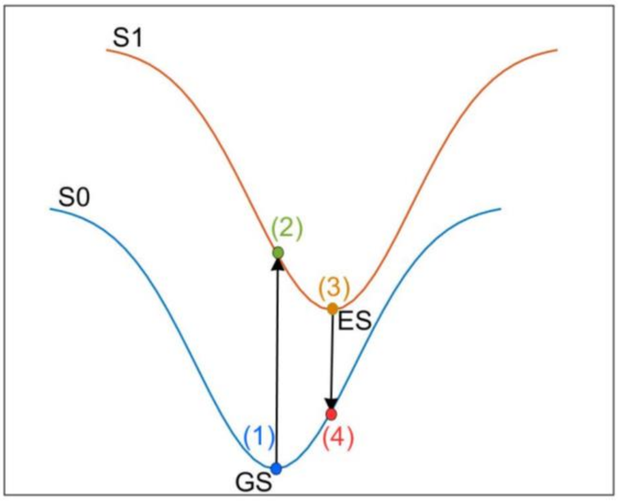

Figure 2.3. Schematic representation of the dye excitation

Table 2.1. Comparison of the dipole moment for the different states of dye

No	Geometry	Singlet	μ_x, D	μ_y, D	μ_z, D	μ, D	Comment
(1)	GS	S_0	-7.99	-2.07	-0.36	8.26	Ground state
(2)		S_1	-15.85	-2.31	-0.81	16.03	Excited state, optimized on ground state
(3)	ES	S_1	-15.42	-2.23	-1.02	15.61	Excited state
(4)		S_0	-9.20	-2.77	-0.58	9.63	Ground state, optimized on excited state

Table 2.1 shows, that the difference in the dipole moments in the excited states with the geometry optimized on the Ground state (GS) and Excited state (ES) levels is small, so we can neglect this difference and with the aim not to change intramolecular parameters in excited state use the partial charges, obtained on the Excited state, optimized on ground state level. In fig. 2.4 the HOMO and LUMO states of molecule D205 is provides. It is shown that the electron density moves

from donor to acceptor part. The π-bridge part has the electron density in both cases, while no density observed around chain. This illustrate, why the calculation of ground and excited state is so important for local structure, so it is necessary to create the force field, which can reproduce well the properties of both states.

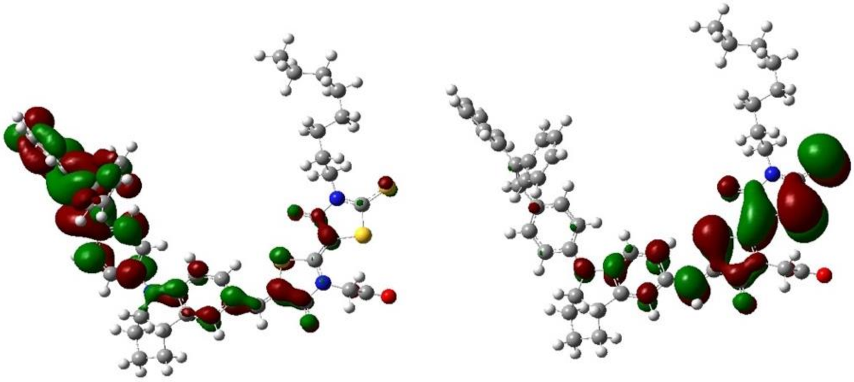

Figure 2.4. HOMO (left) and LUMO (right) spectrum of D205 dye

For the obtaining the partial charges the quantum-chemical calculations on level of theory M06-2X/6-311++G(d,p) with the CHelpG method in vacuum were utilized. CHelpG method has already been used for dye description[63, 64]. In this method atomic charges are fitted to reproduce the molecular electrostatic potential (MESP) at several points around the molecule. Due to the idea of making the force field universal, vacuum charges were used for all further simulations. The comparison of the partial charges is provided in the appendix A, table A1.

2.3. Force field models of the mixture

For the simulation of $BmimBF_4$, the Mondal and Balasubramanian model was used [65] (fig 2.6). The AN force field model was described by Koverga [61] (fig 2.5). Both these models show adequate representation of the experimental properties.

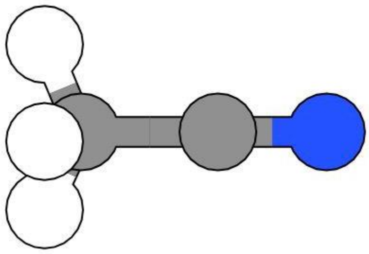

Figure 2.5. AN molecule

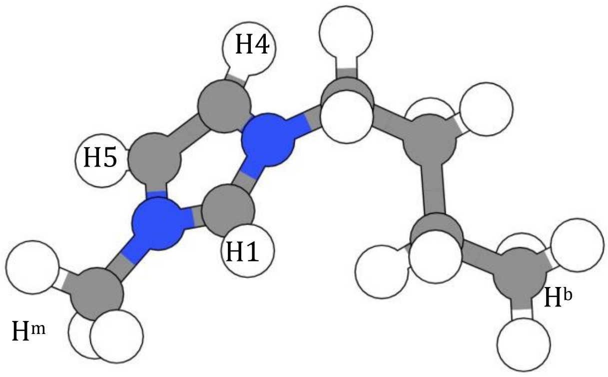

Figure 2.6. Selected atoms of $Bmim^+$

2.4 MD simulation

For understanding local structure around dye D205 in solvent MD simulations was performed. For understanding solvate and structural properties it necessary to carry out MD simulations using the large number of solvent molecule (due to big size of D205). Initially, 1 molecule D205 and 2048 ion pairs BmimBF4 or AN were placed in cubic box and energy was minimized. Cut-off radiuses were equal to 1.4 nm. For long-range electrostatic interactions, the particle mesh Ewald (PME) method with a spacing of 0.12 nm, periodic boundary condition in all direction were used. On the first step of equilibration NVT ensemble at T=398 K, controlled by v-rescale thermostat with relaxation time equal to 0.1 ps, was carried out during 5 ns (integrator time step Δt=0.5 fs). After, the transition to NPT ensemble at T=298 K, P=1 Bar, using Parrinello-Rahman barostat with relaxation time 0.5 ps was made for the correct reproduction of volume fluctuations. The time step was equal to 0.05 fs, during the first 5 ps and after was increased by a factor of 10 for further calculations for 5 ns. In total 4 consecutive productive runs of a duration 5 ns (A, B, C, D) were done for every system. Table 2.2 is represented the composition of all the mixtures. In the range 0-0.2 there is the small step of the ionic liquid mole fraction, because it was shown that in this range there is the specific interactions occurs for the ionic liquid/molecular solvent system.[44]

Table 2.2. The composition of the mixture

Ionic liquid mole fraction	Number of D205	Number of AN	Number of $BmimBF_4$
0	1	2048	0
0.005	1	2037	11
0.05	1	1945	103
0.10	1	1843	205
0.15	1	1741	307
0.20	1	1638	410
0.50	1	1024	1024
0.80	1	410	1638
0.90	1	205	1843
1.00	1	0	2048

2.5. Results and discussions

The local structure around the dye was assessed using the radial distribution function, $g(r)$, (RDF) Due to the large number of atoms of dye, we decided to select atoms from the donor, bridge and acceptor parts of the D205.These atoms are either hydrogen atoms or electronegative ones. The numbering of these atoms is shown in Fig 1,b. As a consequence in our analysis of the locale structure around the dye, the following radial distribution were calculated:

1) The $g(r)$ of the N of the AN around the donor $H^{(43)}$, bridge $H^{(2)}$, the acceptor $H^{(3\text{-}4)}$ and butyl chain $H^{(24\text{-}25)}$ parts of the dye D205 dye.
2) The $g(r)$ of H atoms of cation $Bmim^+$, namely $H^{(1)}$, $H^{(4)}$, $H^{(5)}$, $H^{(m)}$ and $H^{(b)}$ around the electronegative atoms of D205 dye: $O^{(2)}$, $O^{(3)}$, $O^{(4)}$, $S^{(3)}$.
3) The $g(r)$ of the F of the anion BF_4^- around the donor $H^{(43)}$, bridge $H^{(2)}$, the acceptor $H^{(3\text{-}4)}$ and butyl chain $H^{(24\text{-}25)}$ parts of the dye D205 dye.

In order to capture insight into the local structure at the level of the neighbors, the nearest neighbor radial distributions, $g^1(r)$ corresponding to the previously cited RDFs also were calculated. In order to obtained statically reliable $g(r)$ and $g^1(r)$, we carried out 4 subsequent calculations, named A, B, C, D, lasting each 5ns. Two situations were obtained: In the first one, as it is illustrated in Figure 2.7, the subsequent $g^1(r)$, describing the nearest radial neighbor distribution of the F atom of the anion around the hydrogen atom $H^{3\text{-}4}$, are showing the same trend. As a consequence we averaged these distributions and calculated the average value using the equation: $< r_{H^{3-4}-F}\ (n) > = \int_0^\infty dr' r'\, g^1(r')$. This distance was taken as observable to quantify the distribution of the F atoms around these hydrogen atoms of the D205 dye.

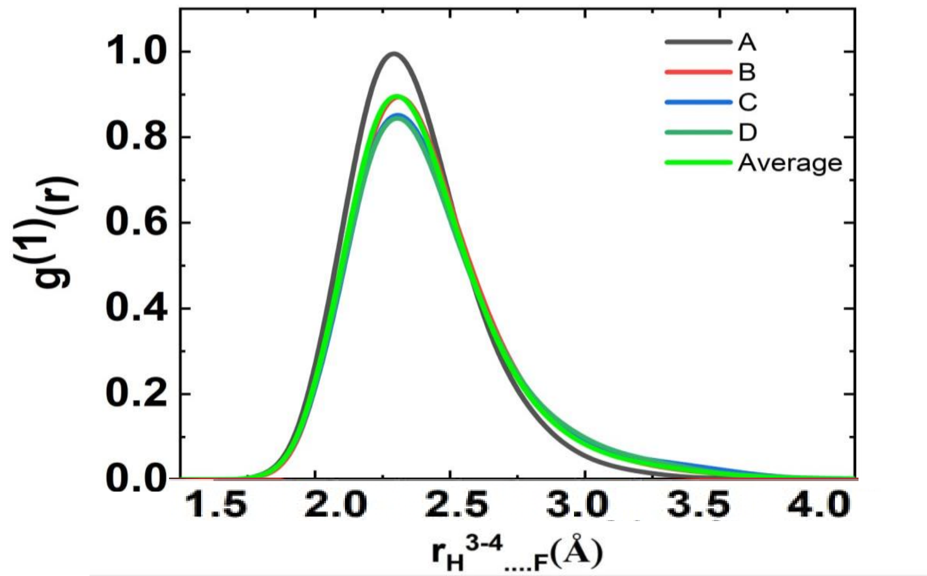

Figure 2.7. Nearest neighbor radial distribution of F atoms of the anion, BF4$^-$, around the H atoms number 3 and 4 of the D205 dye. A, B, C, D refer to the subsequent calculations, lasting 5ns each. The average distribution of these distributions is also shown in this figure.

In a second situation, we found a large evolution between subsequent calculations of the $g^1(r)$. This illustrated, in Figure 2.8, in the case of the nearest neighbor distribution of the oxygen atom, O^1 (see figure 1 for the numbering) around the H^4 of the cation $Bmim^+$.

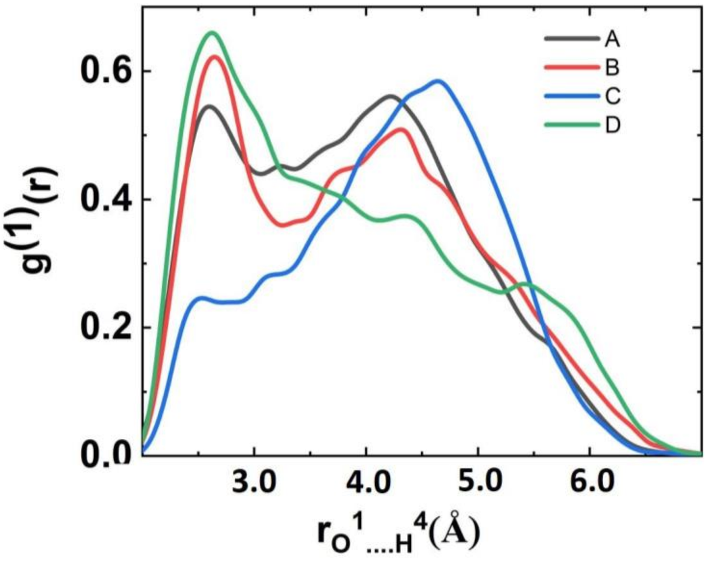

Figure 2.8. Nearest neighbor radial distribution of O^1 atoms of the D205 dye around the H atom number 4 of the cation $Bmim^+$. A, B, C, D refer to the subsequent calculations, lasting 5ns each.

Fig. 2.8 shows clearly a large statistical change in the shape of the $g^1(r)$. Indeed, the first 5 ns calculations shows clearly that there are two preferential radial positions of the nearest neighbor O^1 of the D205 around the H^4 of the cation. A change in the ratio between the intensities of the two contribution is observed in the subsequent 5 ns calculation, in favor of the short distance contribution. This change is confirmed in the third 5 ns calculation. However, in the fourth, the large distance contribution dominates the short distance one. We decided then to characterize the distance between the O1 and H4 using two values associated with the position of the short and the large distance contributions.

2.5.1. Distribution of the AN molecule around the D205 dye in neat AN

In order to characterize the distribution of the solvent around the D205, we calculated the radial distribution functions, $g(r)$, of the N atom of the AN around the hydrogen atoms of the D205 dye, that were selected among donor $H^{(43)}$, bridge

$H^{(2)}$, the acceptor $H^{(3-4)}$ and butyl chain $H^{(24-25)}$ parts (parts of the dye (see Fig. 1 for the number of atoms). These $g(r)$ are given in Figure 10. The corresponding $g^1(r)$ are given in Figure 11. To quantify the changes in the local structure around the D205 after photoexcitation, we calculated the same $g(r)$ and $g^1(r)$ in the excited state. We recall that the photoexcitation is mimicked by changing only the charge distribution on the D205 atom while the geometry of the D205 is unchanged.

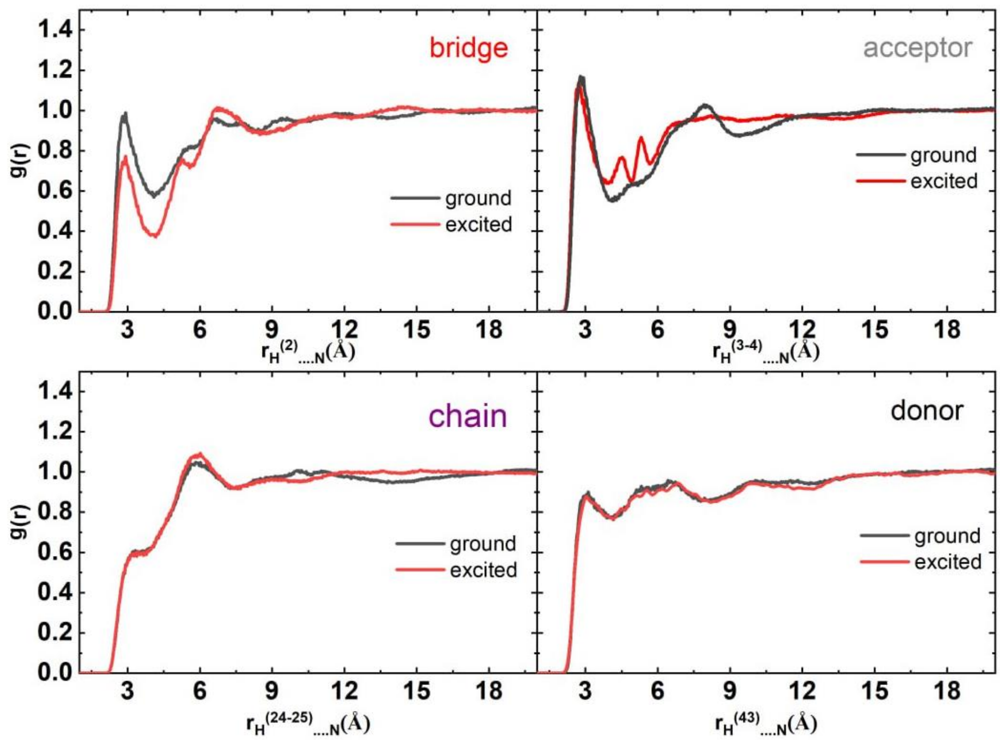

Figure 2.9. Radial distribution function of the N atom of AN around hydrogen atoms chosen in donor $H^{(43)}$, bridge $H^{(2)}$, the acceptor $H^{(3-4)}$ and butyl chain $H^{(24-25)}$ parts of the dye D205 dye. These functions were calculated in the ground and excited states.

Figure 2.9 shows that the position of the first peak (or shoulder) in these $g(r)$ is located around 3 Å and the solvation shell expands up to 4.5 Å. Of note is when we changed the charge distribution to mick the excited state of the dye, the rising part at short distance of the $g(r)$ around the H atoms of the acceptor and bridge parts of the D205 shifts to lower distances in the excited state while the shape of the other $g(r)$ is almost similar in both states. We calculated then the corresponding coordination numbers that are displayed in Figure 2.10. This figure shows that the number of solvent molecules around the H atoms of acceptor and donor parts of D205 is not changed between the ground and excited states, while this number decreases around the H atoms of the chain part (distance higher than 3.2 Å) and increases around that of the bridge part (distance higher than 2.8 Å).

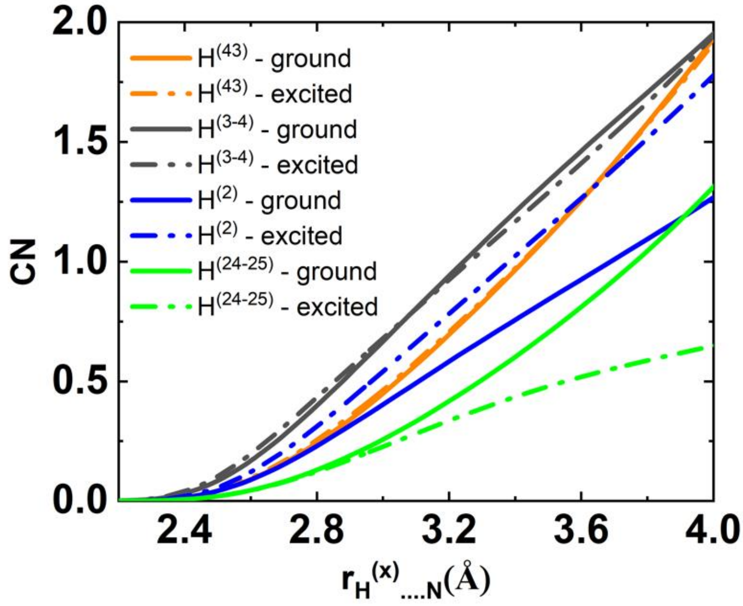

Figure 2.10. Coordination number (CN) of the N atom of AN around hydrogen atoms chosen in the donor $H^{(43)}$, bridge $H^{(2)}$, the acceptor $H^{(3\text{-}4)}$ and butyl chain $H^{(24\text{-}25)}$ parts of the dye D205 dye. These functions were calculated in the ground and excited states.

More insight into the distribution of the solvent around the various part is obtained by analyzing the shape of the corresponding $g^1(r)$. Indeed, Figure 2.11 shows that the position of the solvent molecule, the position of which is described by the N atom, shifts to lower distance around the bridge and acceptor parts of the D205 in comparison those around the donor and chain parts. For the last one, even we notice a slight shift to higher distances. Of note is that spatial distribution of the N atoms around the bridge and acceptor parts of the D205 is reduced in the excited as compared with that in the ground state.

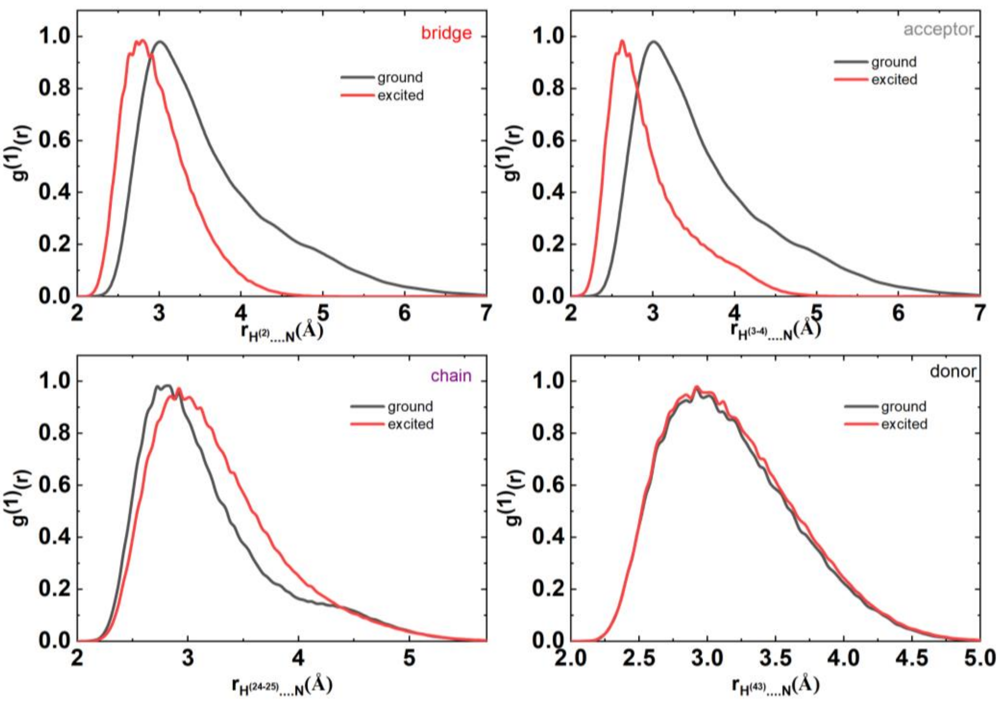

Figure 2.11. Nearest neighbor radial distribution of the N atom of AN around hydrogen atoms chosen in the donor $H^{(43)}$, bridge $H^{(2)}$, the acceptor $H^{(3-4)}$ and butyl chain $H^{(24-25)}$ parts of the dye D205 dye. These functions were calculated in the ground and excited states.

2.5.2. Distribution of the cation and anion around the D205 dye in neat BmimBF4.

In order to investigate the distribution of the cation and anion around the D205, we chose the F atom of the anion, the ring hydrogen atom of the cation, namely $H^{(2)}$, $H^{(4)}$ and $H^{(5)}$ as well as the $H^{(m)}$ and $H^{(b)}$ atoms of the methyl and butyl groups. We then calculated both the radial distribution functions and the coordination number of F atom of the anions around the hydrogen atoms belonging to the acceptor, bridge, donor and chain parts of the D205 dyes. This allows us to characterize the distribution of the anions around the dye. We calculated the radial distribution functions and the corresponding coordination number chosen hydrogen atoms of the cation around the oxygen and sulfur atoms, $O^{(2)}$, $O^{(3)}$, $O^{(4)}$ and $S^{(3)}$ of the D205 dye.

Distribution of the anion around the D205 dye

Figure 2.12 shows clearly that either in the ground state or in the excited state there is no structured radial distribution of the anion around the terminal butyl chain hydrogen atoms. On the contrary the other $g(r)$ are characterized by the occurrence of peaks that suggests that the anion is solvating the H atoms of the acceptor, the bridge and the donor parts of the D205. In general there is small change in the shape of these radial distribution when going from the ground to the excited state. This is confirmed by the behavior of either the corresponding coordination number (see Figure 2.13) and the nearest neighbor radial distribution functions (See Figure 2.14). Indeed, when going from the ground to excited state, the coordination number increases marginally around the H atoms of the chain, the acceptor, the donor parts of the D205 while a noticeable change occurs in that around the bridge H atoms. Of note is that the main changes in the shape of the $g^1(r)$ distribution involving the hydrogen atoms of the acceptor and donor parts of the D205 dyes are localized at large distances and indicates that the F atoms of some anions is expelled to large distances in the excited state with respect to that in the ground states.

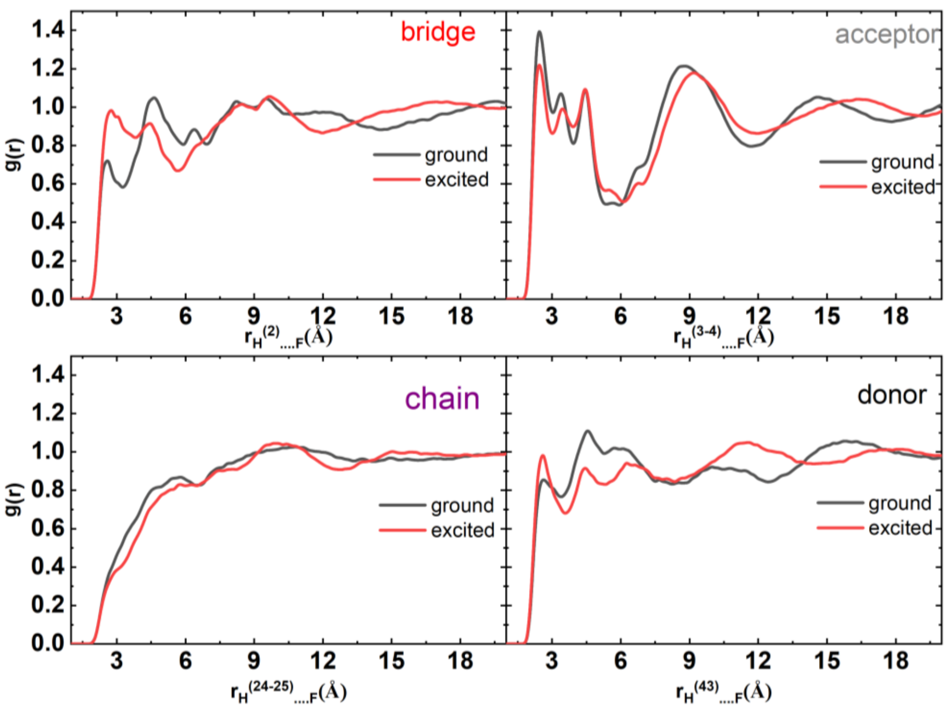

Figure 2.12. Radial distribution function of the F atom of the anion BF_4^- around hydrogen atoms chosen in the donor $H^{(43)}$, bridge $H^{(2)}$, the acceptor $H^{(3-4)}$ and butyl chain $H^{(24-25)}$ parts of the D205 dye. These functions were calculated in the ground and excited states.

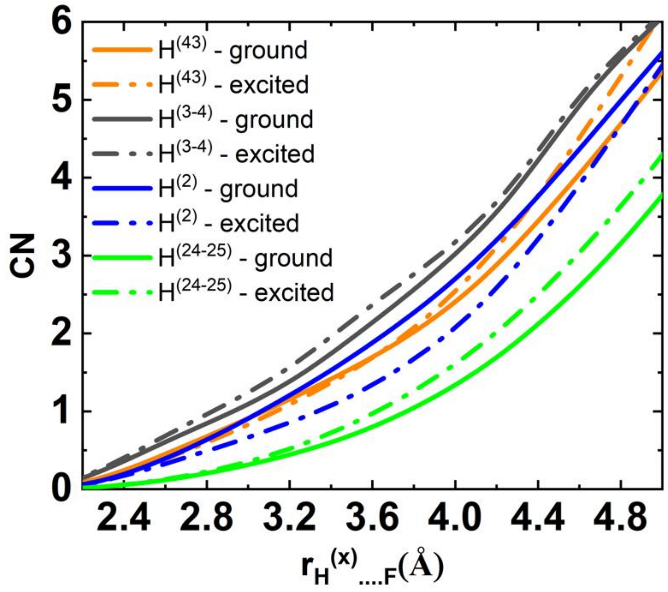

Figure 2.13. Coordination number (CN) of the F atom of the anion BF_4^- around hydrogen atoms chosen in the donor $H^{(43)}$, bridge $H^{(2)}$, the acceptor $H^{(3\text{-}4)}$ and butyl chain $H^{(24\text{-}25)}$ parts of the dye D205 dye. These functions were calculated in the ground and excited states.

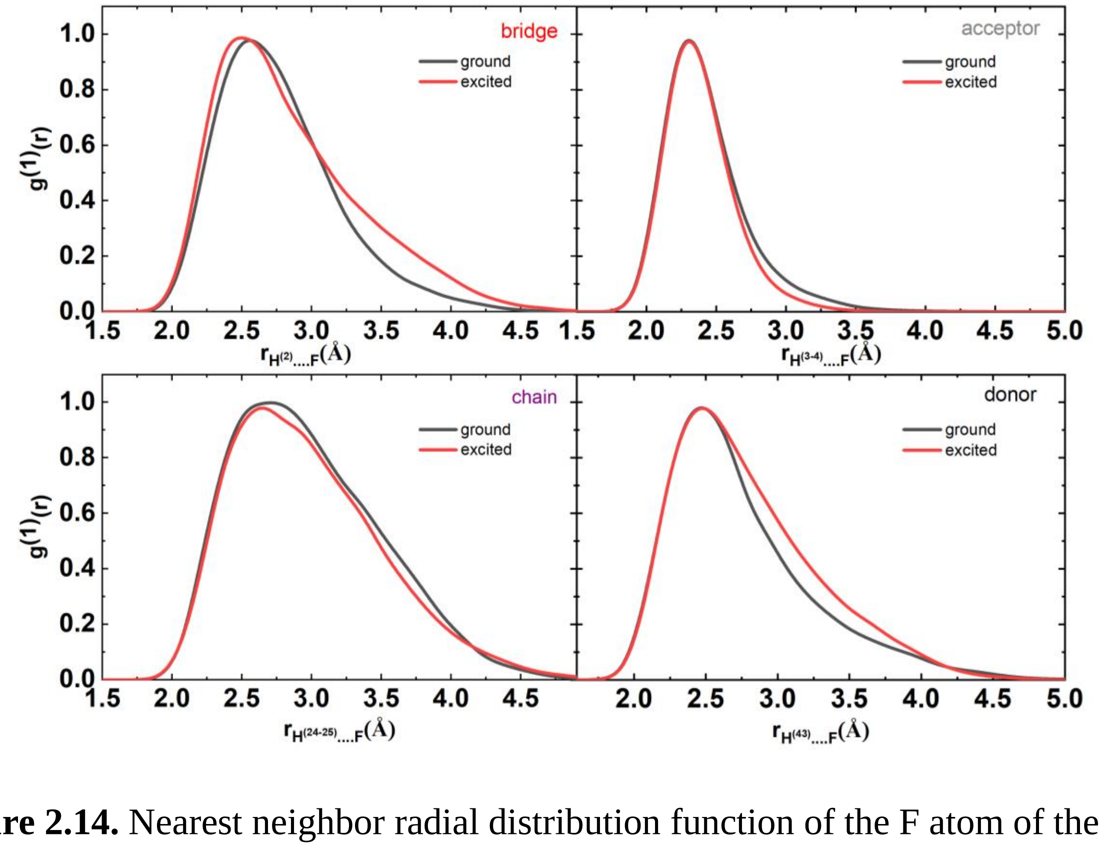

Figure 2.14. Nearest neighbor radial distribution function of the F atom of the anion BF_4^- around hydrogen atoms chosen in the donor $H^{(43)}$, bridge $H^{(2)}$, the acceptor $H^{(3\text{-}4)}$ and butyl chain $H^{(24\text{-}25)}$ parts of the dye D205 dye. These functions were calculated in the ground and excited states.

Distribution of the cations around the D205 dye

Furthermore, we analyzed the distribution of cations around the H atoms of the dye and then calculated the $g(r)$ describing the radial distribution of the H atoms of the cation namely the H atoms of the cation $Bmim^+$, namely $H^{(2)}$, $H^{(4)}$, $H^{(5)}$, $H^{(m)}$ and $H^{(b)}$. (See Figure for numbering) around the electronegative atoms $O^{(2)}$, $O^{(3)}$, $O^{(4)}$, $S^{(3)}$ of the dye D205. These functions, their corresponding coordination number and nearest neighbor distributions are displayed in Figures 2.15, 2.16 and 2.17, respectively.

Figure 2.15 shows that there distribution of the butyl chain H atoms of the cation around the $O^{(2)}$, $O^{(3)}$, $O^{(4)}$, $S^{(3)}$ atoms of the D205 is diffuse as inferred from the absence of any defined peak in the corresponding $g(r)$. The shape of the corresponding $g(r)$ is almost not affected when going from the ground to the excited states. This is also confirmed by the small change in the corresponding coordination number displayed in Figure 2.16. However, the distributions of the methyl $H^{(m)}$ of the cation around these electronegative atoms is well structured as indicated by the occurrence of peaks at short distances. In the excited state the distribution of the $H^{(m)}$ becomes around of $S^{(3)}$and $O^{(4)}$ atoms is more diffuse. This is confirmed by the decease of the corresponding number shown in Fig. 2.16, while in the excited state the distribution of $H^{(m)}$ around $O^{(2)}$, $O^{(3)}$ atoms becomes more structured as indicated by the increase of the intensity of the first peak with respect to that in the ground state. This is also confirmed by the increase of the corresponding coordination number. Small changes are observed in the shape of the $g(r)$ describing the distribution of the $H^{(2)}$ atom around the electronegative atoms of D205 in particular around the $O^{(4)}$, $S^{(3)}$ atoms while a decrease in the intensity is observed for the $g(r)$ involving the $O^{(2)}$, $O^{(3)}$. This confirmed by the small change in the corresponding coordination number. In general, the distribution of $H^{(5)}$ around the electronegative atoms of the D205 follows the same trend as that of $H^{(m)}$. However, the changes (increase/decrease of the intensity of the first peak as well as the coordination number) occur with less extent.

The $g(r)$ of $H^{(4)}$ atom around $O^{(4)}$, $S^{(3)}$and $O^{(3)}$ electronegative atom of the dye seems not bet affected when going in from the ground to the excited states. Also, this is confirmed by the small change in the corresponding coordination number. However, although the shape of $g(r)$ of the $H^{(4)}$ around the $O^{(2)}$ atom is strongly affected when going from the ground to the excited state as indicated by the large increase of the intensity of the first peak , the corresponding coordination number is marginally increasing suggesting that the number of $H^{(4)}$ around $O^{(2)}$ is not strongly affected.

These results indicate that the main changes in the distribution of the cation around the electronegative atoms of the dye involve the methyl $H^{(m)}$.

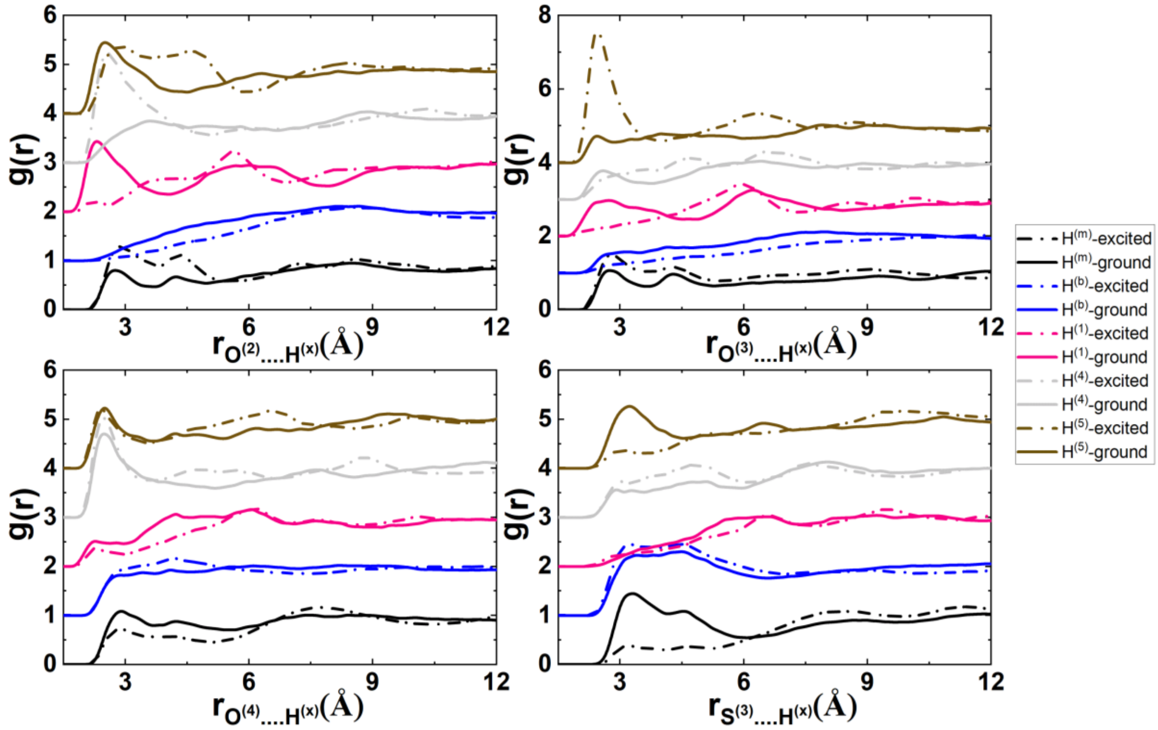

Figure 2.15. Radial distribution function of the $H^{(1)}$, $H^{(4)}$, $H^{(5)}$, $H^{(m)}$ and $H^{(b)}$ atoms of the cation $BMIM^+$ around electronegative atoms $O^{(2)}$, $O^{(3)}$, $O^{(4)}$, $S^{(3)}$ of the dye D205 dye. These functions were calculated in the ground and excited states.

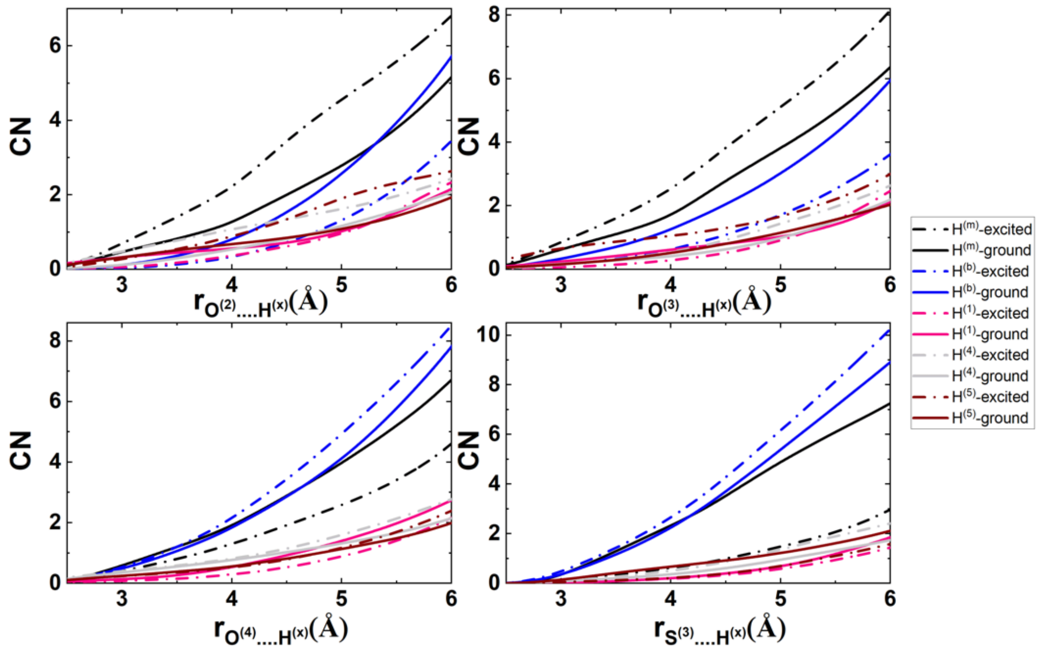

Figure 2.16. Coordination number (CN) of the $H^{(1)}$, $H^{(4)}$, $H^{(5)}$, $H^{(m)}$ and $H^{(b)}$ atoms of the cation $BMIM^+$ around electronegative atoms $O^{(2)}$, $O^{(3)}$, $O^{(4)}$, $S^{(3)}$ of the dye D205 dye. These functions were calculated in the ground and excited states.

The overall changes in the shape of the $g^1(r)$ describing the radial distribution of the H atoms of the cation ring around the electronegative atoms of the D205 are shown in Fig. 2.17 and are consistent with those in the shape of the corresponding $g(r)$. Based on these distributions we calculated the corresponding average distances that are shown in Figure 2.18.

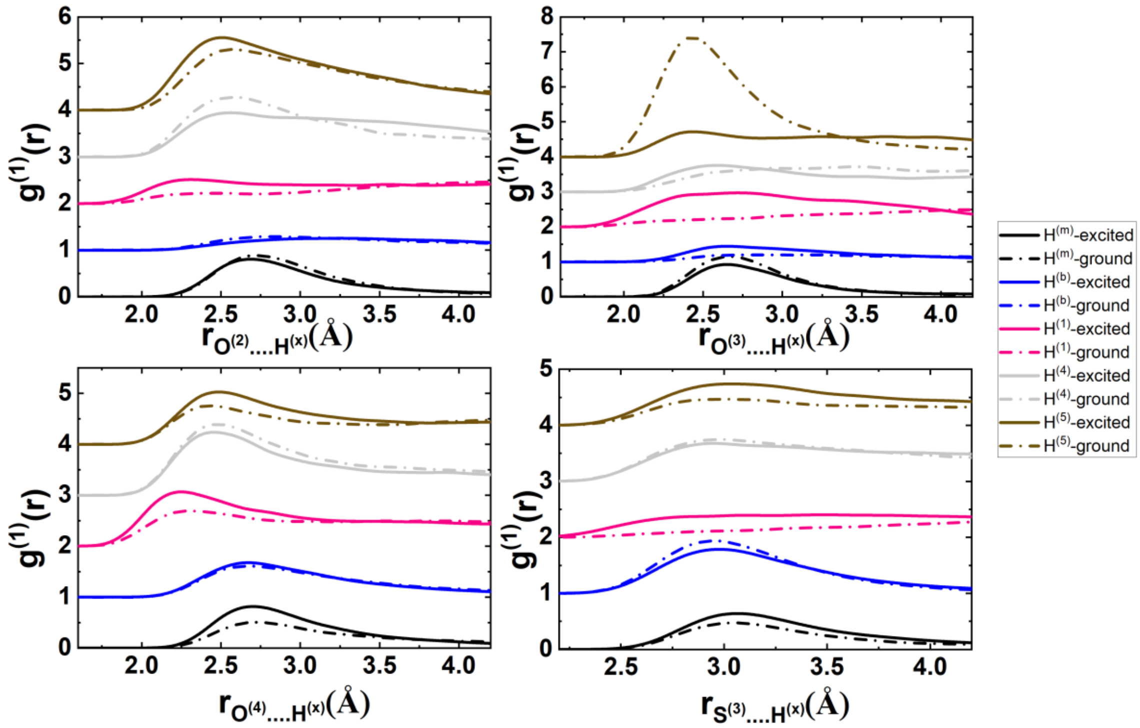

Figure 2.17. Nearest neighbor radial distribution function of the the $H^{(1)}$, $H^{(4)}$, $H^{(5)}$, $H^{(m)}$ and $H^{(b)}$ atoms of the cation $Bmim^{+}$ around electronegative atoms $O^{(2)}$, $O^{(3)}$, $O^{(4)}$, $S^{(3)}$ of the dye D205 dye. These functions were calculated in the ground and excited states.

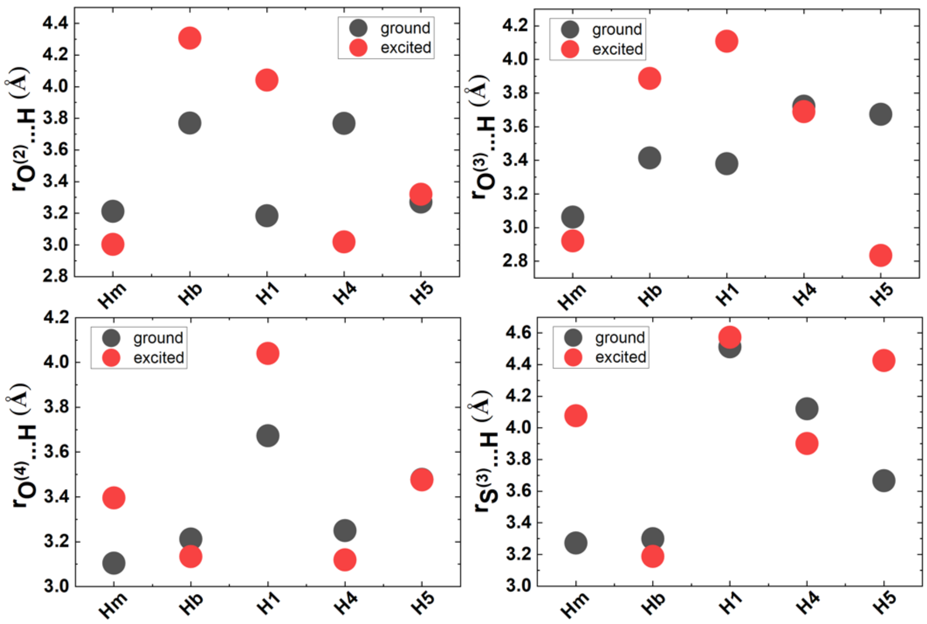

Figure 2.18. Average distance as determined from the earest neighbor radial distribution functions of the the $H^{(1)}$, $H^{(4)}$, $H^{(5)}$, $H^{(m)}$ and $H^{(b)}$ atoms of the cation $Bmim^{+}$ around electronegative atoms $O^{(2)}$, $O^{(3)}$, $O^{(4)}$, $S^{(3)}$ of the D205 dye.

These functions were calculated in the ground and excited states. When going from the ground to the excited state

(i) the average distance between the $H^{(m)}$ and the electronegative atoms of the D205 increases when considering the $O^{(4)}$, $S^{(3)}$ while it decreases when considering the other ones.

(ii) the average distance between $H^{(5)}$ and the $S^{(3)}$ increases and $O^{(3)}$ decreases, while almost no changes are occurring when considering its average distance with respect to the $O^{(3)}$ and $O^{(4)}$ atoms.

(iii) the average distance between $H^{(1)}$ and the electronegative atoms, it increases systematically when considering the O atoms while no change is observed for $S^{(3)}$.

(iv) the average distance between $H^{(b)}$ and $O^{(3)}$ or $O^{(2)}$ increases, while almost no changes are occurring when considering its average distance with respect to the $O^{(2)}$ and $S^{(3)}$ atoms

(v) the average distance between $H^{(4)}$ and $S^{(3)}$ or $O^{(4)}$ or $O^{(3)}$ remains almost the same, while it increase when considering $O^{(2)}$.

2.5.3. Distribution of the cations, anions and solvent around the D205 dye in the D205/BmimBF$_4$/AN mixture

In this part of the thesis, we will investigate how the local distribution of the cation, anion, and solvent molecules around different part of the hydrogen atoms of the D205 is affected by the change in the mixture composition. Following the same scheme that we used for the analysis of the locale structure of the D205 in neat solvent and ionic liquid, we started our analysis by calculating the radial distribution function between different atoms of the D205 and the N atom of the AN. They are displayed in Figure 2.19. This figure shows that in the range of mole fraction of ionic liquid between 0.05 and 0.2 (high solvent content), the shape of these functions is not affected when going from the ground to excited state. However, noticeable differences in the distribution of the N atoms of the solvent are observed at low solvent content, showing that in the case of donor $H^{(43)}$, bridge $H^{(2)}$ and the acceptor $H^{(3\text{-}4)}$ parts the intensity of the first peak is lower, respectively that the corresponding one in the ground state. While in the case of the chain H atoms, this intensity increases.

Due to the statistical uncertainties, we think that the behavior of these $g(r)$ at very low solvent content are difficult to interpret.

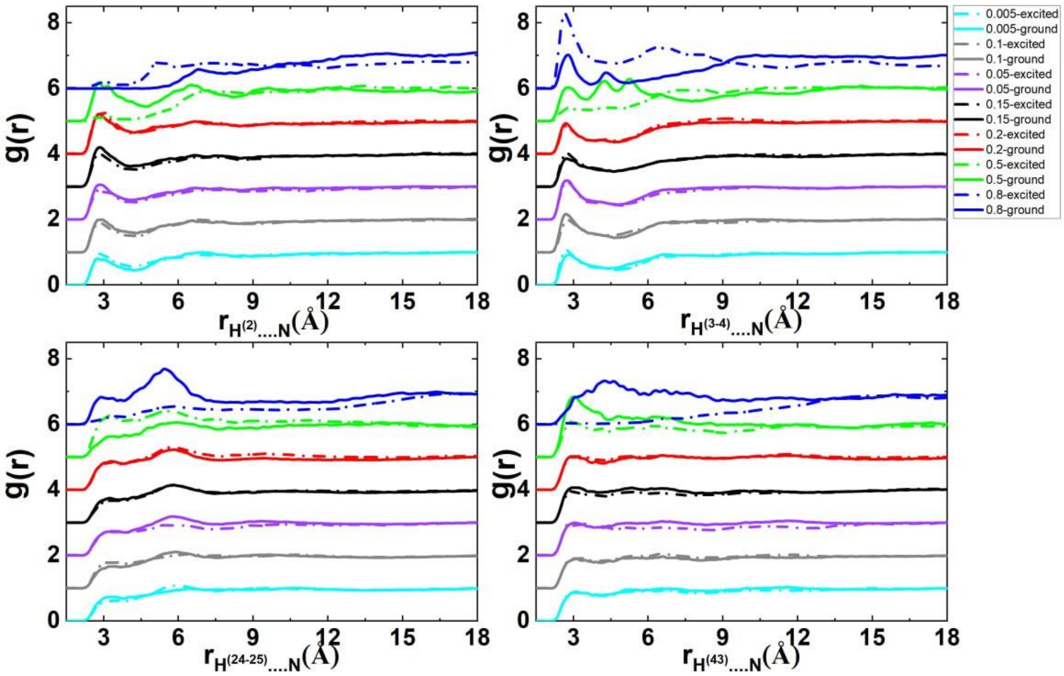

Figure 2.19. The ionic liquid mole fraction dependence of the radial distribution function of the N atom of AN around hydrogen atoms chosen in the donor $H^{(43)}$, bridge $H^{(2)}$, the acceptor $H^{(3-4)}$ and butyl chain $H^{(24-25)}$ of the dye D205 dye. These functions were calculated in the ground and excited states.

If now we look to these $g(r)$ through the mixture composition dependence of the corresponding coordination number (shown in Figure 2.20), we can formulate the following observations:

(i) The coordination number is not affected in the range of mole fraction range of the ionic liquid between 0.05 and 0.2.

(ii) At 0.5, in accordance with our interpretation of the behavior of the $g(r)$, the coordination number of N atom of the solvent around the donor $H^{(43)}$, the bridge $H^{(2)}$, the acceptor $H^{(3-4)}$ decrease in the excited state, while around the butyl chain $H^{(24-25)}$ it increases.

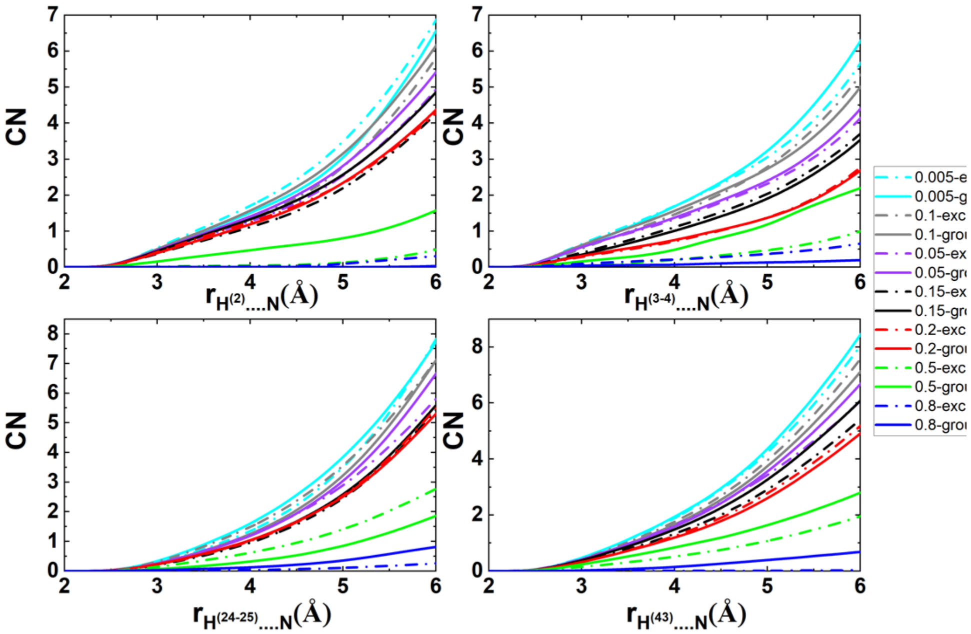

Figure 2.20. The ionic liquid mole fraction dependence of the coordination number (CN) of the N atom of AN around hydrogen atoms chosen in the donor $H^{(43)}$, bridge $H^{(2)}$, the acceptor $H^{(3-4)}$ and butyl chain $H^{(24-25)}$ parts of the dye D205 dye. These functions were calculated in the ground and excited states.

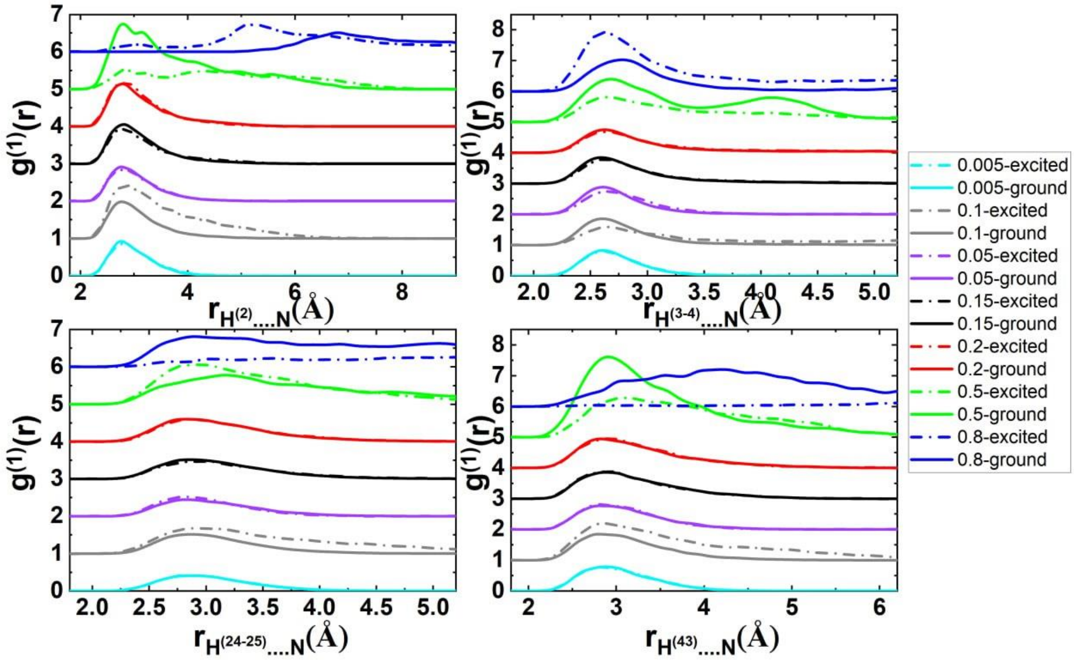

Figure 2.21. The ionic liquid mole fraction dependence of the nearest neighbor radial distribution function radial distribution function of the N atom of AN around hydrogen atoms chosen in the donor $H^{(43)}$, bridge $H^{(2)}$, the acceptor $H^{(3-4)}$ and butyl chain $H^{(24-25)}$ parts of the dye D205 dye. These functions were calculated in the ground and excited states.

The mole fraction dependence of the nearest neighbor distribution of the solvent molecules around the H atoms of the dyes is given in Figure 2.21. Their behavior is in accordance with our previous analysis.

To investigate the mole fraction dependence of the local structure of the anion around the H atoms of the D205, we calculated the radial distribution function, the corresponding coordination number, and the nearest neighbor distribution displayed in Figures 2.22, 2.23 and 2.24 respectively. These figures suggest that there is a small change in the radial distribution of the anion around the Hydrogen atoms of the dye.

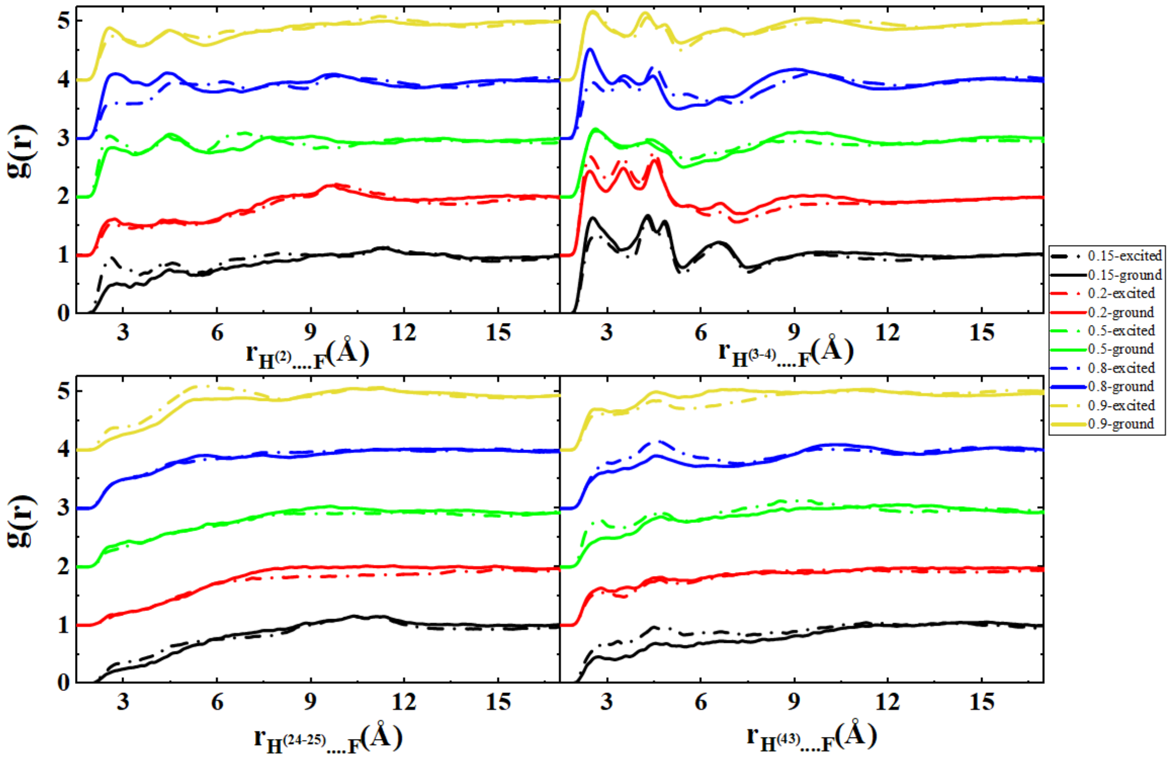

Figure 2.22. The ionic liquid mole fraction dependence of the radial distribution function of the F atom of the anion BF4$^-$ around hydrogen atoms chosen in the donor $H^{(43)}$, bridge $H^{(2)}$, the acceptor $H^{(3-4)}$ and butyl chain $H^{(24-25)}$ parts of the dye D205 dye. These functions were calculated in the ground and excited states.

This affirmation can be affined by investigating the mixture content dependence of the coordination number shown in Fig. 2.24. Indeed, the difference between this parameter in the ground and exited state, is reduce when the ionic liquid is diluted.

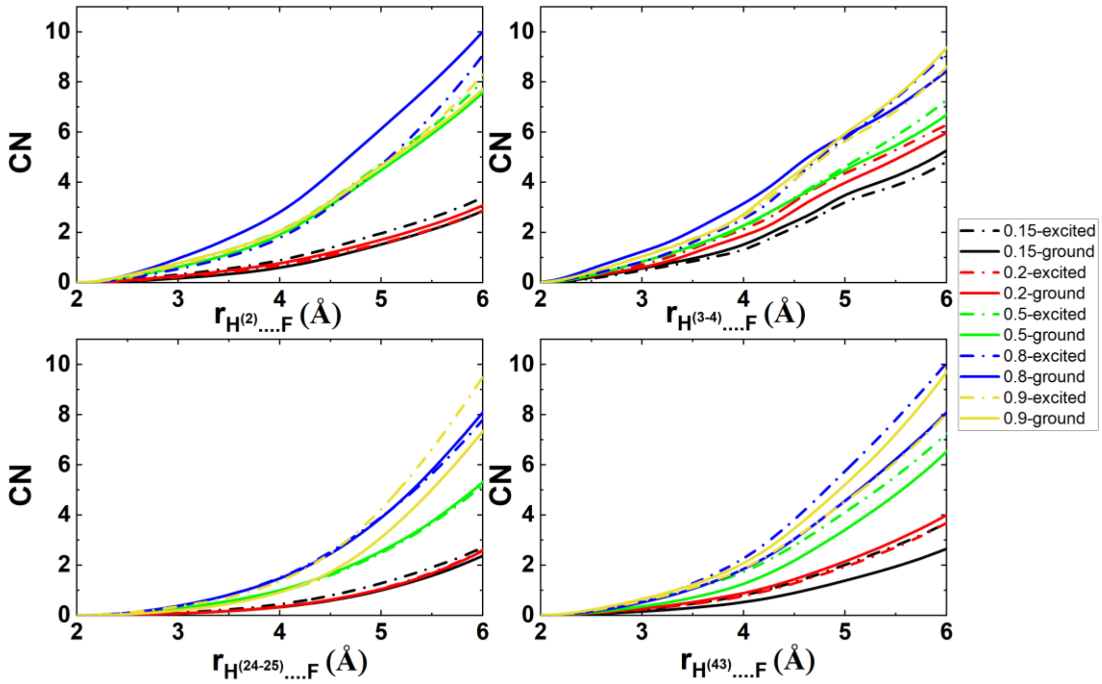

Figure 2.23. The ionic liquid mole fraction dependence of the coordination number (CN) of the F atom of the anion BF_4^- around hydrogen atoms chosen in donor $H^{(43)}$, bridge $H^{(2)}$, the acceptor $H^{(3-4)}$ and butyl chain $H^{(24-25)}$ parts of the dye D205 dye. These functions were calculated in the ground and excited states.

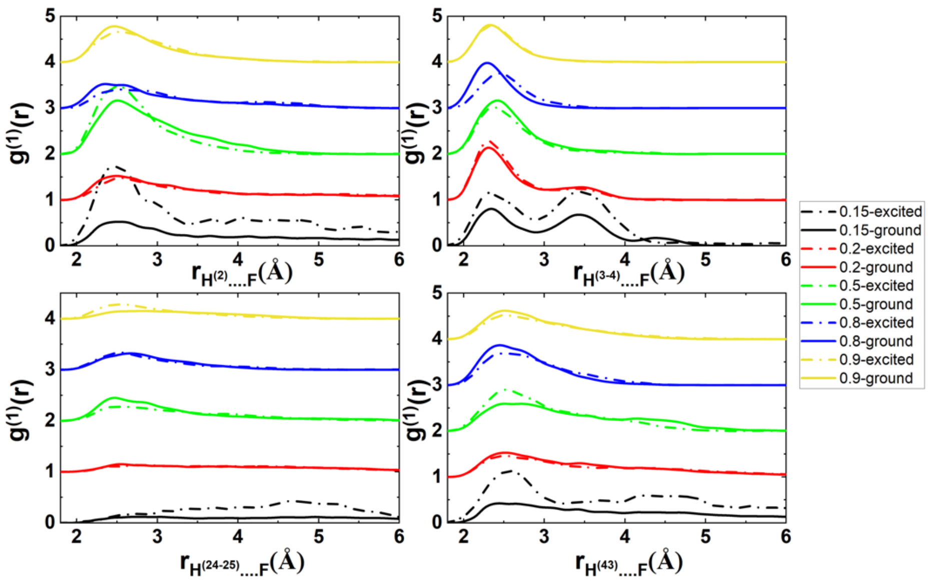

Figure 2.24. The ionic liquid mole fraction dependence of the nearest neighbor radial distribution function F atom of the anion BF_4^- around hydrogen atoms chosen in donor $H^{(43)}$, bridge $H^{(2)}$, the acceptor $H^{(3-4)}$ and butyl chain $H^{(24-25)}$ parts of the dye D205 dye. These functions were calculated in the ground and excited states.

The investigation of the mole fraction dependence of the distribution of the cation around the electronegative atoms of the D205 is analyzed through the calculation of the same statistical distributions namely the $g(r)$, the corresponding coordination function and the $g^1(r)$ that are displayed in the following figures: figures 2.25 for $H^{(b)}$, figure 2.26 for $H^{(m)}$, figure 2.27 for $H^{(1)}$, figure 2.28 for $H^{(4)}$ and figure 2.29 for $H^{(5)}$. Based on the evolution of these distributions according to both the change of the charge distribution of the D205 from the ground to the excited state, and the change of the mixture composition we can formulate the following points:

(i) The distribution of the H^b atom of the cation butyl group around the electronegative atoms of the dye becomes diffuse at low ionic liquid content (around 0.2) and at the same mole ionic liquid mole fraction the shape of these distributions is in general less affected when going from the ground to the excited state. The difference between the coordination numbers of H^b around all the electronegative atoms in ground and excited state becomes smaller in lower mole fraction of ionic liquid. This is confirmed by the behavior of the corresponding $g^1(r)$. Of note is that we don't have any explanation in the change in the shape of this distribution involving the $S^{(3)}$ and $O^{(2)}$ at 0.5 ionic liquid mole fraction.

(ii) The distribution of the $H^{(m)}$ of the cation methyl group is affected by the change of both charge distribution on the D205 and the mixture composition around all the electronegative atoms. In the whole mixture composition, the coordination numbers of $H^{(m)}$ around the $O^{(2)}$ and $O^{(3)}$ atoms is higher in the excited state than in the ground state while the opposite trend is observed for that around $S^{(3)}$ and $O^{(4)}$.

(iii) The distribution of $H^{(1)}$ around the $S^{(3)}$ is diffuse and it is not affected neither by the change of the mixture composition nor by the change in the charge distribution. This also seen in the small difference in the corresponding coordination numbers. Although there are changes in the shape of the describing the distribution of $H^{(1)}$ around $S^{(3)}$, the corresponding coordination number is almost not affected by the change in the charge distribution.

(iv) The distribution of $H^{(4)}$ atom around all the electronegative atoms is more affected by the change in the charge distribution and not by the change in the ionic liquid mole fractions. This is based on the small change of both the position and shape of the peak stay stable for the full concentration range. Minor changes of the coordination number of $H^{(4)}$ around $S^{(3)}$ were observed below 0.8 mole fraction.

(v) The distribution of $H^{(5)}$ atom around $S^{(3)}$ atom shows the changes only due to the transfer from ground to excited state. Minor changes are observed in the corresponding coordination number as well as that around $O^{(4)}$.

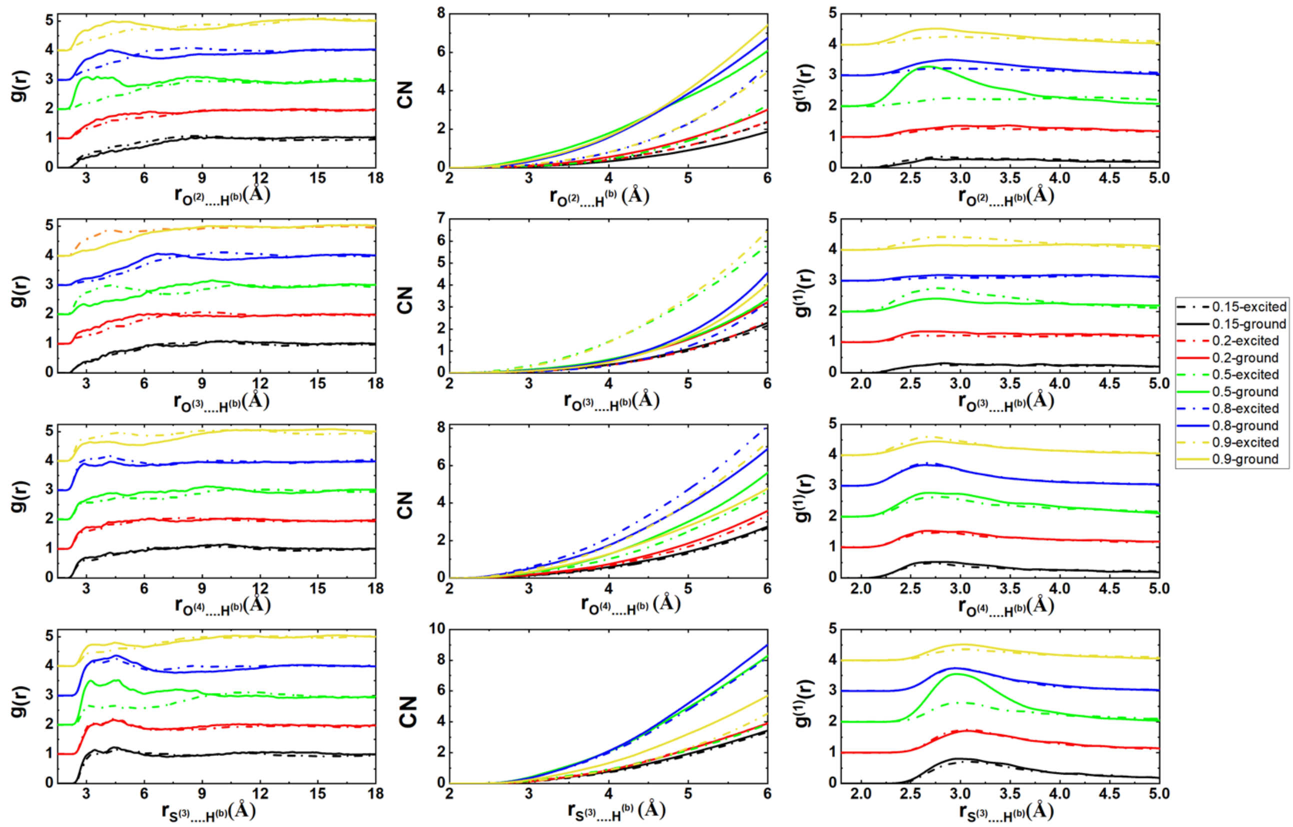

Figure 2.25. The ionic liquid mole fraction dependence of the radial distribution function (left) and coordination number (middle) and the nearest neighbor (right) of the $H^{(b)}$ atom of the cation $Bmim^{+}$ around electronegative atoms $O^{(2)}$, $O^{(3)}$, $O^{(4)}$, $S^{(3)}$ of the D205 dye. These functions were calculated in the ground and excited states.

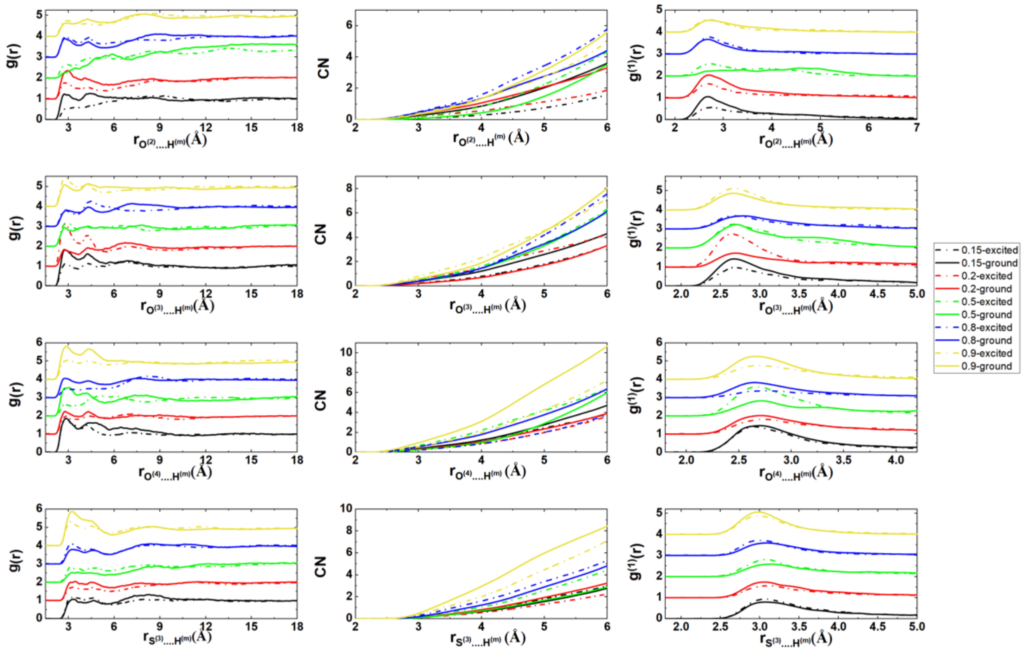

Figure 2.26. The ionic liquid mole fraction dependence of the radial distribution function (left) and coordination number (middle) and the nearest neighbor (right) of the $H^{(m)}$ atom of the cation $Bmim^{+}$ around electronegative atoms $O^{(2)}$, $O^{(3)}$, $O^{(4)}$, $S^{(3)}$ of the D205 dye. These functions were calculated in the ground and excited states.

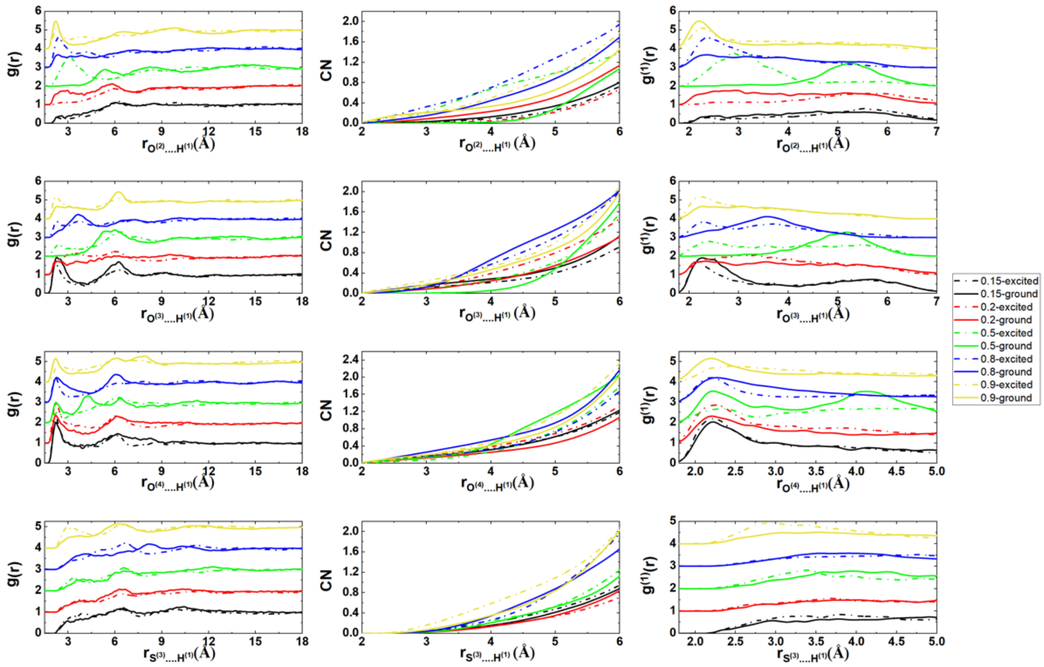

Figure 2.27. The ionic liquid mole fraction dependence of the radial distribution function (left) and coordination number (middle) and the nearest neighbor (right) of the $H^{(1)}$ atom of the cation $Bmim^{+}$ around electronegative atoms $O^{(2)}$, $O^{(3)}$, $O^{(4)}$, $S^{(3)}$ of the D205 dye. These functions were calculated in the ground and excited states.

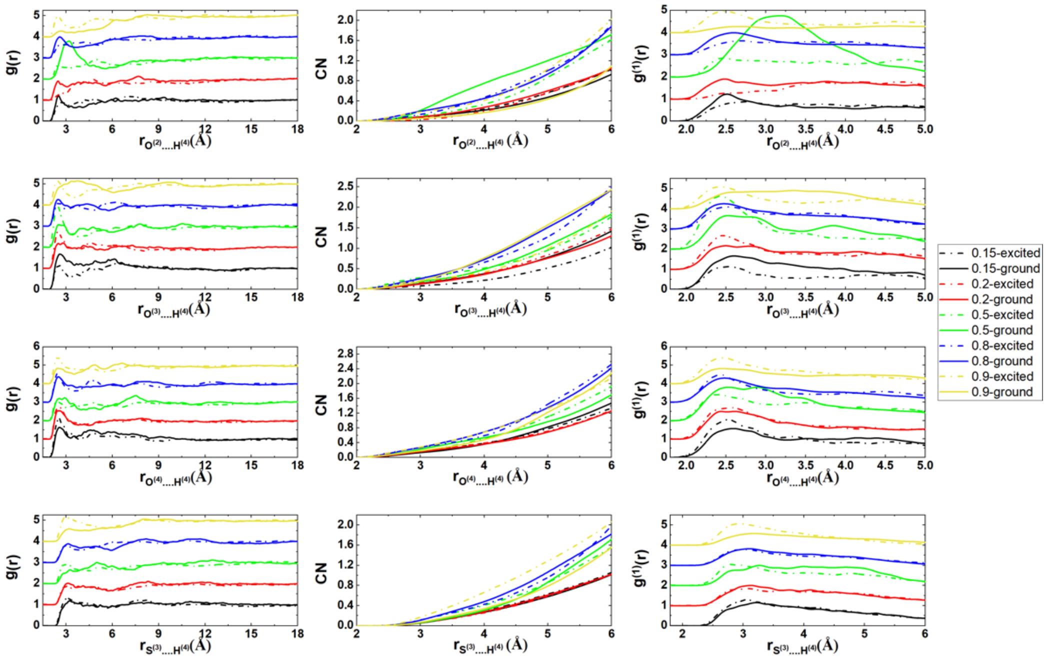

Figure 2.28. The ionic liquid mole fraction dependence of the radial distribution function (left) and coordination number (middle) and the nearest neighbor (right) of the $H^{(4)}$ atom of the cation $Bmim^+$ around electronegative atoms $O^{(2)}$, $O^{(3)}$, $O^{(4)}$, $S^{(3)}$ of the D205 dye. These functions were calculated in the ground and excited states.

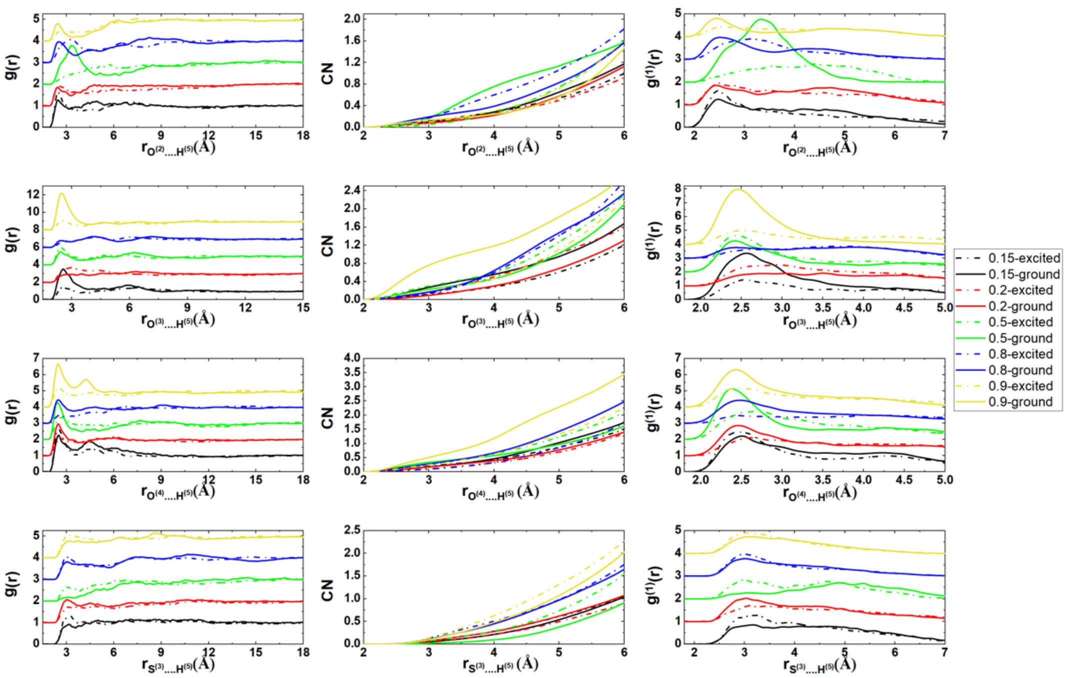

Figure 2.29. The ionic liquid mole fraction dependence of the radial distribution function (left) and coordination number (middle) and the nearest neighbor (right) of the $H^{(4)}$ atom of the cation $Bmim^+$ around electronegative atoms $O^{(2)}$, $O^{(3)}$, $O^{(4)}$, $S^{(3)}$ of the D205 dye. These functions were calculated in the ground and excited states.

In figure 2.30, we gathered the distance average values between the H atoms of the D205 and the N and F atoms of the solvent and anions respectively.

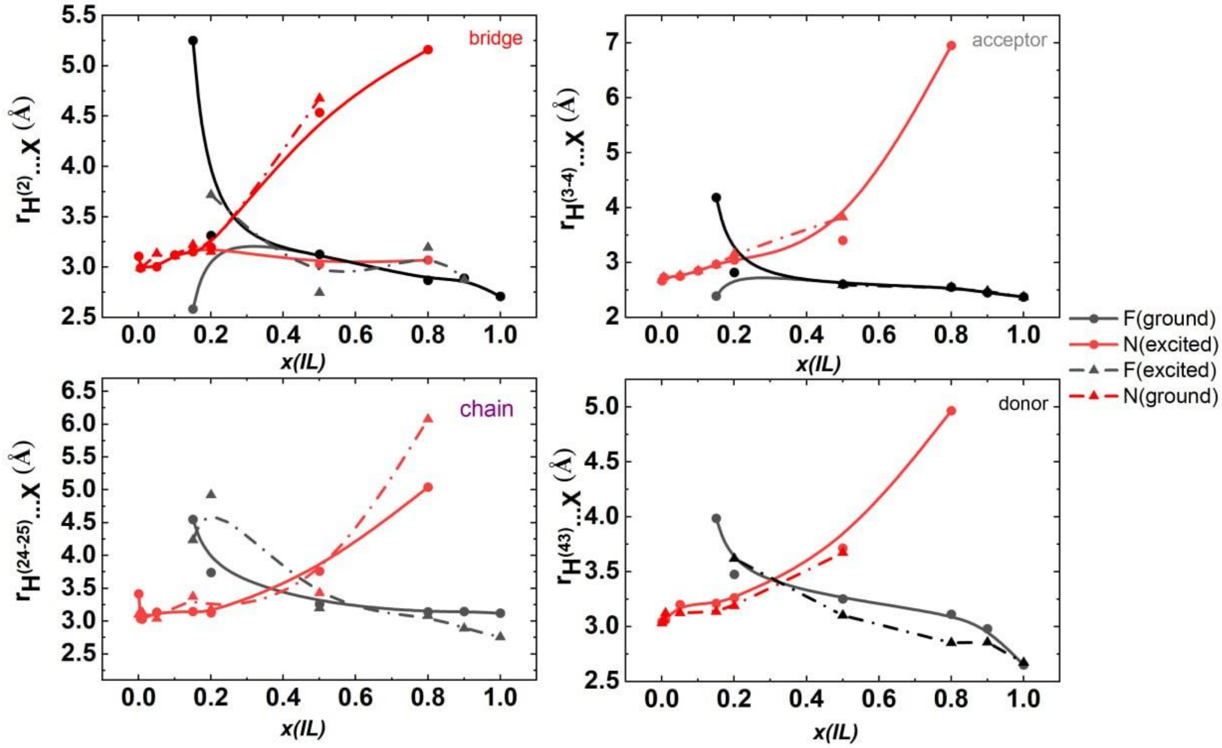

Figure 2.30. The ionic liquid mole fraction dependence of the mean distances between N of AN and F atom of the anion $BF4^-$ around hydrogen atoms chosen in donor $H^{(43)}$, bridge $H^{(2)}$, the acceptor $H^{(3\text{-}4)}$ and butyl chain $H^{(24\text{-}25)}$ parts of the dye D205 dye. These functions were calculated in the ground and excited states.

These average distances values were calculated for the ground and excited state in the while mole fraction range. Fig. 2.30 shows clearly that there is a cross over between one side the distance of the H atoms of the dye and the N atoms of AN and from the other side the distance between the same hydrogen atoms of the dye and the F atom of the anion. This cross over occurs in the mole fraction range between 0.2 and 0.4. In addition, Fig. 2.30 also shows, that the behavior of the average distance involving the H atoms of the chain part and the donor parts of the dye is almost similar to each other.

2.6. Conclusions

In this work we have provided the parameters for the intramolecular part of the force field model of indoline dye D205 as well as the charge distributions that mimic its ground state and excited states. Our quantum calculations show that there is a small change in the geometry of the dye D205 in the ground and excited states. As consequence in our molecular dynamic simulations the geometry of the D205 was not changed between the two states.

Based on the new force field model, the effect of the mixture composition of BmimBF4/AN on the local structure of D205 was analyzed in the whole mixture composition including the neat components. The is analysis was based the radial distribution function, the corresponding nearest neighbor, and the coordination numbers. Our results show that in neat ionic liquid, there is no difference between the ground and excited states in the distribution of the anion around the H atoms of the donor, bridge, acceptor, and the chain parts, while there a large difference for the distribution of the H atom of the methyl group of the cation around these atoms. Our results also show that there is a difference between the ground and excited states in the distribution of the N atom of AN around both the bridge and the acceptor parts.

The investigation of the mixture composition of the solvent and ions around the H atoms of the dye indicates that:

(i) the distribution of the solvent is only affected at low solvent content and that the coordination number of N atom of the solvent around the donor $H^{(43)}$, the bridge $H^{(2)}$, the acceptor $H^{(3-4)}$ decrease in the excited state, while around the butyl chain $H^{(24-25)}$ it increases.

ii) The distribution of the anions undergoes a small change when going from the ground to the excited state.

Because of the large number of possible ways to describe the distribution of the cation around the electronegative atoms of the D205, it was difficult to come with a clear conclusion on this issue, however our results show that because the $O^{(3)}$

and $O^{(4)}$ atoms are close to each other the distribution of the cation around these atoms is quiet similar in the ground and excited states. While differences are observed the distribution of the cation around the $O^{(2)}$ and $S^{(3)}$ atoms.

2.7. References for Chapter 2

1. Barone, V., et al., *Fluorescence spectra of organic dyes in solution: a time dependent multilevel approach.* Phys Chem Chem Phys, 2011. **13**(6): p. 2160-6.
2. Bevilaqua, T., D.C. da Silva, and V.G. Machado, *Preferential solvation of Brooker's merocyanine in binary solvent mixtures composed of formamides and hydroxylic solvents.* Spectrochimica Acta Part A: Molecular and Biomolecular Spectroscopy, 2004. **60**(4): p. 951-958.
3. Khodadadi-Moghaddam, M., A. Habibi-Yangjeh, and M.R. Gholami, *Solvatochromic parameters for binary mixtures of an ionic liquid with various protic molecular solvents.* Monatshefte für Chemie - Chemical Monthly, 2009. **140**(3): p. 329-334.
4. Kurnikova, M.G., et al., *Rotational Relaxation in Polar Solvents. Molecular Dynamics Study of Solute−Solvent Interaction.* Journal of the American Chemical Society, 1998. **120**(24): p. 6121-6130.
5. Li, W., et al., *Effect of water and organic solvents on the ionic dissociation of ionic liquids.* J Phys Chem B, 2007. **111**(23): p. 6452-6.
6. Monti, S., et al., *Theoretical Investigation of Adsorption, Dynamics, Self-Aggregation, and Spectroscopic Properties of the D102 Indoline Dye on an Anatase (101) Substrate.* The Journal of Physical Chemistry C, 2016. **120**(5): p. 2787-2796.
7. Oliveira, C.S., et al., *Solvent and concentration effects on the visible spectra of tri-para-dialkylamino-substituted triarylmethane dyes in liquid solutions.* Spectrochim Acta A Mol Biomol Spectrosc, 2002. **58**(13): p. 2971-82.
8. Rauf, M.A., A.A. Soliman, and M. Khattab, *Solvent effect on the spectral properties of Neutral Red.* Chemistry Central Journal, 2008. **2**(1): p. 19.
9. Trivedi, S., A. Sarkar, and S. Pandey, *Solvatochromic absorbance probe behavior within 1-butyl-3-methylimidazolium hexafluorophosphate+propylene carbonate: Preferential solvation or solvent–solvent interaction?* Chemical Engineering Journal, 2009. **147**(1): p. 36-42.
10. Graen, T., M. Hoefling, and H. Grubmüller, *AMBER-DYES: Characterization of Charge Fluctuations and Force Field Parameterization of Fluorescent Dyes for Molecular Dynamics Simulations.* Journal of Chemical Theory and Computation, 2014. **10**(12): p. 5505-5512.
11. Jacquemin, D., et al., *Accurate Simulation of Optical Properties in Dyes.* Accounts of Chemical Research, 2009. **42**(2): p. 326-334.
12. Madkour, L.H., et al., *Quantum chemical calculations, molecular dynamics simulation and experimental studies of using some azo dyes as corrosion inhibitors for iron. Part 1: Mono-azo dye derivatives.* Journal of the Taiwan Institute of Chemical Engineers, 2016.
13. Selvaraj, A.R. and S. Hayase, *Molecular dynamics simulations on the aggregation behavior of indole type organic dye molecules in dye-sensitized solar cells.* J Mol Model, 2012. **18**(5): p. 2099-104.
14. Baryshnikov, G.V., B.F. Minaev, and V.A. Minaeva, *Quantum-chemical study of the structure and optical properties of sensitized dyes of an indoline-thiazolidine series.* Optics and Spectroscopy, 2010. **108**(1): p. 16-22.
15. Fakis, M., et al., *A time resolved fluorescence and quantum chemical study of the solar cell sensitizer D149.* Dyes and Pigments, 2013. **96**(1): p. 304-312.
16. Jacquemin, D., et al., *TD-DFT Performance for the Visible Absorption Spectra of Organic Dyes: Conventional versus Long-Range Hybrids.* Journal of Chemical Theory and Computation, 2008. **4**(1): p. 123-135.
17. Lambert, C., et al., *Characterization of high-performance organic dyes for dye-sensitized solar cell: a DFT/TDDFT study.* Canadian Journal of Chemistry, 2016. **94**(12): p. 1109-1118.

18. Le Bahers, T., et al., *A TD-DFT investigation of ground and excited state properties in indoline dyes used for dye-sensitized solar cells.* Phys Chem Chem Phys, 2009. **11**(47): p. 11276-84.
19. Nazeeruddin, M.K., et al., *Combined Experimental and DFT-TDDFT Computational Study of Photoelectrochemical Cell Ruthenium Sensitizers.* Journal of the American Chemical Society, 2005. **127**(48): p. 16835-16847.
20. Sánchez-de-Armas, R., et al., *Real-Time TD-DFT Simulations in Dye Sensitized Solar Cells: The Electronic Absorption Spectrum of Alizarin Supported on TiO2 Nanoclusters.* Journal of Chemical Theory and Computation, 2010. **6**(9): p. 2856-2865.
21. Martins, L., et al., *Solvation dynamics of coumarin 153 in dimethylsulfoxide-water mixtures: Molecular dynamics simulations.* The Journal of Chemical Physics, 2003. **118**: p. 5955-5963.
22. Banik, D., et al., *Picosecond Solvation and Rotational Dynamics: An Attempt to Reinvestigate the Mystery of Alcohol–Water Binary Mixtures.* The Journal of Physical Chemistry B, 2015. **119**(30): p. 9905-9919.
23. Yalcin, D., et al., *Solvation properties of protic ionic liquid–molecular solvent mixtures.* Physical Chemistry Chemical Physics, 2020. **22**(19): p. 10995-11011.
24. Nandi, S., et al., *Local environment of organic dyes in an ionic liquid-water mixture: FCS and MD simulation.* The Journal of Chemical Physics, 2018. **149**: p. 054501.
25. Smortsova, Y., et al., *Interrogating the mechanism of the solvation dynamics in BmimBF4/PC mixtures: A cooperative study employing time-resolved fluorescence and molecular dynamics.* Journal of Molecular Liquids, 2021. **340**: p. 117163.
26. Smortsova, Y., et al., *Solvation dynamics and rotation of coumarin 153 in a new ionic liquid/molecular solvent mixture model: [BMIM][TFSI]/propylene carbonate.* Journal of Molecular Liquids, 2017. **226**: p. 48-55.
27. Annapureddy, H.V.R., et al., *How Does Water Affect the Dynamics of the Room-Temperature Ionic Liquid 1-Hexyl-3-methylimidazolium Hexafluorophosphate and the Fluorescence Spectroscopy of Coumarin-153 When Dissolved in It?* The Journal of Physical Chemistry B, 2008. **112**(6): p. 1770-1776.
28. Ambade, S.B., et al., *Indoline-dye immobilized ZnO nanoparticles for whopping 5.44% light conversion efficiency.* Journal of Photochemistry and Photobiology A: Chemistry, 2011. **222**(2–3): p. 366-369.
29. El-Zohry, A.M., D. Roca-Sanjuán, and B. Zietz, *Ultrafast Twisting of the Indoline Donor Unit Utilized in Solar Cell Dyes: Experimental and Theoretical Studies.* The Journal of Physical Chemistry C, 2015. **119**(5): p. 2249-2259.
30. Fan, W., et al., *Computational study of diketopyrrolopyrrole-based organic dyes for dye sensitized solar cell applications.* Journal of Molecular Graphics and Modelling, 2015. **57**: p. 62-69.
31. Ham, H.W. and Y.S. Kim, *Theoretical study of indoline dyes for dye-sensitized solar cells.* Thin Solid Films, 2010. **518**(22): p. 6558-6563.
32. Huang, L., L. Jiang, and M. Wei, *Metal-free indoline dye sensitized solar cells based on nanocrystalline Zn2SnO4.* Electrochemistry Communications, 2010. **12**(2): p. 319-322.
33. Ito, S., et al., *High-conversion-efficiency organic dye-sensitized solar cells with a novel indoline dye.* Chemical Communications, 2008(41): p. 5194-5196.
34. Kim, J.Y., Y.H. Kim, and Y.S. Kim, *Indoline dyes with various acceptors for dye-sensitized solar cells.* Current Applied Physics, 2011. **11**(1): p. S117-S121.
35. Kuang, D., et al., *Organic Dye-Sensitized Ionic Liquid Based Solar Cells: Remarkable Enhancement in Performance through Molecular Design of Indoline Sensitizers.* Angewandte Chemie International Edition, 2008. **47**(10): p. 1923-1927.

36. Liu, Z., et al., *Solution-processed organic photovoltaics based on indoline dye molecules developed in dye-sensitized solar cells.* Molecules, 2013. **18**(3): p. 3107-17.
37. Matsui, M., et al., *Highly efficient substituted triple rhodanine indoline dyes in zinc oxide dye-sensitized solar cell.* Tetrahedron, 2010. **66**(37): p. 7405-7410.
38. Matsui, M., et al., *Substituent effects in a double rhodanine indoline dye on performance of zinc oxide dye-sensitized solar cell.* Dyes and Pigments, 2010. **86**(2): p. 143-148.
39. Xu, J., et al., *DFT studies on the electronic structures of indoline dyes for dye-sensitized solar cells.* Journal of the Serbian Chemical Society, 2010. **75**(2): p. 259-269.
40. Zhang, C.R., et al., *Comparative study on electronic structures and optical properties of indoline and triphenylamine dye sensitizers for solar cells.* J Mol Model, 2013. **19**(4): p. 1553-63.
41. Suzuka, M., et al., *A Quasi-Solid State DSSC with 10.1% Efficiency through Molecular Design of the Charge-Separation and -Transport.* Sci Rep, 2016. **6**: p. 28022.
42. Smortsova, Y., *Thèse de Yevheniia Smortsova*. 2018, Université de Lille,.
43. Maity, N., *Thèse de Nishith Maity*. 2022, Université de Lille.
44. Maity, N., et al., *Effect of the Mixture Composition of BmimBF4–Acetonitrile on the Excited-State Relaxation Dynamics of a Solar-Cell Dye D149: An Ultrafast Transient Absorption Study.* The Journal of Physical Chemistry C, 2021. **125**(32): p. 17841-17852.
45. El-Zohry, A., A. Orthaber, and B. Zietz, *Isomerization and Aggregation of the Solar Cell Dye D149.* J Phys Chem C Nanomater Interfaces, 2012. **116**(50): p. 26144-26153.
46. Pastore, M. and F. De Angelis, *Aggregation of Organic Dyes on TiO2 in Dye-Sensitized Solar Cells Models: An ab Initio Investigation.* ACS Nano, 2010. **4**(1): p. 556-562.
47. Selvaraj, A.R.K. and S. Hayase, *Molecular dynamics simulations on the aggregation behavior of indole type organic dye molecules in dye-sensitized solar cells.* Journal of Molecular Modeling, 2012. **18**(5): p. 2099-2104.
48. Blazhynska, M.M., et al., *Structure and dynamics of TiO2-anchored D205 dye in ionic liquids and acetonitrile.* Journal of Molecular Liquids, 2021. **332**: p. 115811.
49. Stepaniuk, D.S., et al., *Solvatochromism of a D205 indoline dye at the interface of a small TiO2-anatase nanoparticle in acetonitrile: a combined molecular dynamics simulation and DFT calculation study.* Molecular Simulation, 2022. **48**(2): p. 99-107.
50. Patil, M.K., M.G. Kotresh, and S.R. Inamdar, *A combined solvatochromic shift and TDDFT study probing solute-solvent interactions of blue fluorescent Alexa Fluor 350 dye: Evaluation of ground and excited state dipole moments.* Spectrochimica Acta Part A: Molecular and Biomolecular Spectroscopy, 2019. **215**: p. 142-152.
51. Bevilaqua, T., et al., *Solute–solvent and solvent–solvent interactions in the preferential solvation of 4-[4-(dimethylamino)styryl]-1-methylpyridinium iodide in 24 binary solvent mixtures.* Spectrochimica Acta Part A: Molecular and Biomolecular Spectroscopy, 2006. **65**(3): p. 535-542.
52. Shaw, R.A., et al., *CHARMM-DYES: Parameterization of Fluorescent Dyes for Use with the CHARMM Force Field.* Journal of Chemical Theory and Computation, 2020. **16**(12): p. 7817-7824.
53. Rappe, A.K., et al., *UFF, a full periodic table force field for molecular mechanics and molecular dynamics simulations.* Journal of the American Chemical Society, 1992. **114**(25): p. 10024-10035.

54. Jorgensen, W.L., D.S. Maxwell, and J. Tirado-Rives, *Development and Testing of the OPLS All-Atom Force Field on Conformational Energetics and Properties of Organic Liquids.* Journal of the American Chemical Society, 1996. **118**(45): p. 11225-11236.
55. Ponder, J.W. and D.A. Case, *Force fields for protein simulations.* Adv Protein Chem, 2003. **66**: p. 27-85.
56. Jiang, S., et al., *Double D–π–A branched organic dye isomers for dye-sensitized solar cells.* J. Mater. Chem. A, 2014. **2**(40): p. 17153-17164.
57. Comba, P. and R. Remenyi, *A new molecular mechanics force field for the oxidized form of blue copper proteins.* Journal of computational chemistry, 2002. **23**(7): p. 697-705.
58. Turner, E.A., C.C. Pye, and R.D. Singer, *Use of ab Initio Calculations toward the Rational Design of Room Temperature Ionic Liquids.* The Journal of Physical Chemistry A, 2003. **107**(13): p. 2277-2288.
59. Shimin, H., et al., *Investigation of triptycene-based surface-mounted rotors.* Nanotechnology, 2003. **14**(5): p. 566.
60. Sebesta, F., et al., *Estimation of Transition-Metal Empirical Parameters for Molecular Mechanical Force Fields.* J Chem Theory Comput, 2016. **12**(8): p. 3681-8.
61. Koverga, V.A., et al., *A new potential model for acetonitrile: Insight into the local structure organization.* Journal of Molecular Liquids, 2017. **233**: p. 251-261.
62. Graen, T., M. Hoefling, and H. Grubmüller, *AMBER-DYES: Characterization of Charge Fluctuations and Force Field Parameterization of Fluorescent Dyes for Molecular Dynamics Simulations.* J Chem Theory Comput, 2014. **10**(12): p. 5505-12.
63. Oliveira, B.G. and M.L.A.A. Vasconcellos, *Hydrogen bonds in alcohols:water complexes: A theoretical study about new intramolecular interactions via CHELPG and AIM calculations.* Journal of Molecular Structure: THEOCHEM, 2006. **774**(1): p. 83-88.
64. Sorour, M.I., et al., *Accurate Modeling of Excitonic Coupling in Cyanine Dye Cy3.* The Journal of Physical Chemistry A, 2021. **125**(36): p. 7852-7866.
65. Mondal, A. and S. Balasubramanian, *Quantitative Prediction of Physical Properties of Imidazolium Based Room Temperature Ionic Liquids through Determination of Condensed Phase Site Charges: A Refined Force Field.* The Journal of Physical Chemistry B, 2014. **118**(12): p. 3409-3422.

Chapter 3. Structure and properties of TiO2-anchored D205 dye in different solvent: TDDFT and MD simulation study

The material presented in this chapter forms the basis of publication

1. Stepaniuk, D. S.; Blazhynska, M. M.; Koverga, V.; Kyrychenko, A.; Miannay, F.-A.; Idrissi, A.; Kalugin, O. N. (2022) Solvatochromism of a D205 indoline dye at the interface of a small TiO_2-anatase nanoparticle in acetonitrile: a combined molecular dynamics simulation and DFT calculation study. Molecular Simulation, 48 (2), 99-107.

2. Blazhynska, M. M.; Stepaniuk, D. S.; Koverga, V.; Kyrychenko, A.; Idrissi, A.; Kalugin, O. N. (2021). *Structure and dynamics of TiO_2-anchored D205 dye in ionic liquids and acetonitrile.* Journal of Molecular Liquids, 332, 115811.

The conformational dynamics of a dye molecule anchored to TiO_2 is the key to understanding the mechanical aspects of the photovoltaic performance of dye-sensitized solar cell devices. In this chapter joint molecular dynamics (MD) simulations and density functional theory (DFT) calculations to investigate the structure and dynamics of an indoline D205 dye anchored at the solid-liquid interface of small TiO_2 anatase nanoparticle solvated with explicit acetonitrile (AN) solution was present. DFT calculations were carried out to estimate the equilibrium geometry of a small $Ti_{30}O_{62}H_4$ anatase nanoparticle and to derive interaction parameters for bidentate binding of a D205 dye to TiO_2. The effect of the different solvent on the conformation of the anatase-anchored D205 dye and the resulting solvatochromic shift was investigated by MD simulations, demonstrating that an explicit solvent representation is vital to reproduce the optical spectra of a D205 dye.

3.1. Introduction

Dye-sensitized solar cells (DSSCs), which are based on dyes adsorbed (or covalently bonded) onto a TiO_2 surface, have many promising features, such as high efficiency of solar energy conversion and the low cost of structural elements [1]. Dye-sensitizers are the most critical component in a DSSCs part because they govern key processes, regulating the power conversion efficiency, such as light absorption, charge injection, dye regeneration, and charge recombination, respectively [2]. Therefore, the rapid development of DSSC technologies demands continuous tuning of the chemical properties of organic dyes because the light conversion efficiency is crucially governed by dye photophysics [1]. Moreover, significant efforts have still to be applied in order to overcome the major technological challenges, including the design of an anchoring moiety and a binding mode of a dye onto a TiO_2 surface [3-5].

It has been found that indoline dyes exhibit greater power conversion efficiency compared to available organic dye sensitizers [6]. A D205 dye has a push-pull system, in which an indoline moiety acts as an electron donor, and a rhodamine ring operates as an electron acceptor. Several lines of evidence suggested that the sensitizing efficiency of a D205 dye could be enhanced by the chemical anchoring to the TiO_2 semiconductor active layer [7-9]. Therefore, for practical application, a functional anchoring group, such as carboxylic one –COOH, can be introduced into the rhodanine-acceptor moiety [3].

Besides the proper design of the dye-TiO_2 interface, the environment also affects the DSSC overall performance. Due to the unique properties of ionic liquids (ILs), such as low vapor pressure, non-flammability, high conductivity, and thermal and chemical stability, ILs have become promising electrolytes for DSSC devices capable of passivation of active surfaces of DSSC devices [10]. In addition, some molecular solvents with a large dipole moment, such as acetonitrile (AN), may also be utilized as a perspective electrolyte for DSSC applications. However, understanding the microstructure of an liquid/electrode interface requires atomic-level investigations of the interaction between an electrolite and an electrode surface [11].

Modern quantum-chemical methodologies, such as those based on density functional theory (DFT) and its time-dependent extension (TDDFT), can provide the theoretical framework to describe most of the crucial properties of the individual components of dye/semiconductor systems, such as the dye geometry, optical absorption spectra, and the semiconductor bandgap [12-15]. However, the reliable prediction of absorption spectra and solvatochromic shifts of organic dyes attached to small TiO_2 nanoparticles and solvated by polar liquids is still challenging from a computational point of view [16-21]. It is crucial to accurately compute the excited states of a dye molecule and reproduce correctly an electronic bandgap of TiO_2 semiconductor utilizing the same DFT approach [9, 14, 18, 22, 23]. On the other hand, the solvent-induced conformational changes of a dye molecule due to the polar environment, dye aggregation, and specific hydrogen-bonding interactions with solvent molecules also need to be correctly accounted for [24-27].

Recently, classical molecular dynamics (MD) simulations have proven itself a powerful computational tool for studying the structure of electrolyte/TiO_2 interfaces, which may guide the rational design of a dye and save synthetic and experimental resources [9, 28, 29]. Moreover, MD simulations may complement experimental results of conformational dynamics and spectroscopic properties of a dye attached to TiO_2 [19]. Nonetheless, most of previous efforts were focused on electrolyte-TiO_2 interactions [9], so that phenomena and mechanisms related to TiO_2-dye interactions have not been well understood, especially on the nanoscale.

3.2. Molecular Dynamics Simulation Setup

3.2.1 DFT Structure of D205 Dye anchored to $Ti_{30}O_{62}H_4$

The structure of the indoline D205 dye attached to a $Ti_{30}O_{62}H_4$ anatase nanoparticle was first studied by the density functional theory (DFT) approach at the HSEH1PBE/TZV[84] level of theory. The $Ti_{30}O_{62}H_4$ nanoparticle was truncated from a perfect anatase slab, and its size was sufficient to approximate the electronic structure and the bandgap of the bulk TiO_2 [14, 30, 31]. For simplicity, the long N-octyl tail in the D205 dye was truncated to the ethyl moiety (Figure 3.1 *right*), mimicking structurally similar indoline D149 dye. It has been demonstrated that organic dyes used for DSSC devices were commonly anchored to TiO_2 by the carboxylic group. The latter prefers the chemical bonding to TiO_2 by the bidentate mode. The structure of the D205 dye, bonded to the surface of a $Ti_{30}O_{62}H_4$ anatase nanoparticle by the deprotonated carboxylic group $–COO^-$, was fully optimized at the HSEH1PBE/TZV level, as shown in Figure 3.1(*right*). The proton dissociated from the carboxylic group was bound to the nearest uncoordinated Ti atom. This proton bonding allows keeping electroneutrality so that the total change of D205-$Ti_{30}O_{62}H_4$ conjugate was equal to zero. This procedure is commonly used to avoid DFT optimization of adsorption of open-shell systems and charged dyes onto TiO_2 [13, 19, 30, 32-35].

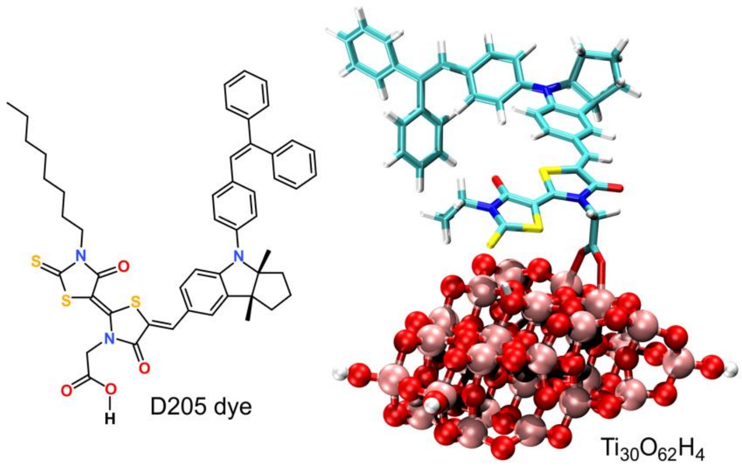

Figure 3.1. The structure of a free D205 dye (*left)* and of the D205 dye anchored to a $Ti_{30}O_{62}H_4$ nanoparticle optimized at the HSEH1PBE/TZV theory level (*right*). For computational reasons, the N-octyl chain in the D205 dye was truncated to the ethyl one.

UV-vis absorption spectra of a free D205 dye and the D205-$Ti_{30}O_{62}H_4$ conjugate were calculated using the time-dependent DFT (TDDFT) at the hybrid CAM-B3LYP functional [36] and the TZV basis set [37]. To estimate a UV-vis absorption spectrum, up to 30 vertical transition $S_0 \rightarrow S_n$ were calculated. To heed the spectral band broadening in solution, the excited-state transitions possessing non-zero oscillator strength were approximated by the Gaussian function. The resulting TDDFT spectra were represented as a superposition of a sum of single Gaussian bands. All DFT calculations were performed with the Gaussian 09 software package [38].

3.2.2 MD force field for all the components

A TiO_2 (001) surface was approximated by the perfect passivized anatase slab composed of 12×12×1 unit cells. The slab was cut from the perfect anatase crystal with the lattice parameters a=0.373 nm and c=0.937 nm using the VESTA software package [39]. Figure 3.2 shows a supercell organized into the two (001) layers with the size of 4.54 nm along x and y-axes, respectively.

Most of MD simulations of bulk TiO_2 are commonly carried out with the empirical force-field (FF) developed by Matsui and Akaogi (MA) [40]. In the MA-FF, the non-bonded interaction parameters between Ti and O were determined by reproducing the crystal structure of various polymorphic forms of TiO_2. The energetic interactions in TiO_2 were assumed to be completely non-covalent. The dispersion and repulsion interactions were represented by the Buckingham potential [40], whereas the electrostatic contributions were treated with the pairwise additive Coulomb potential.

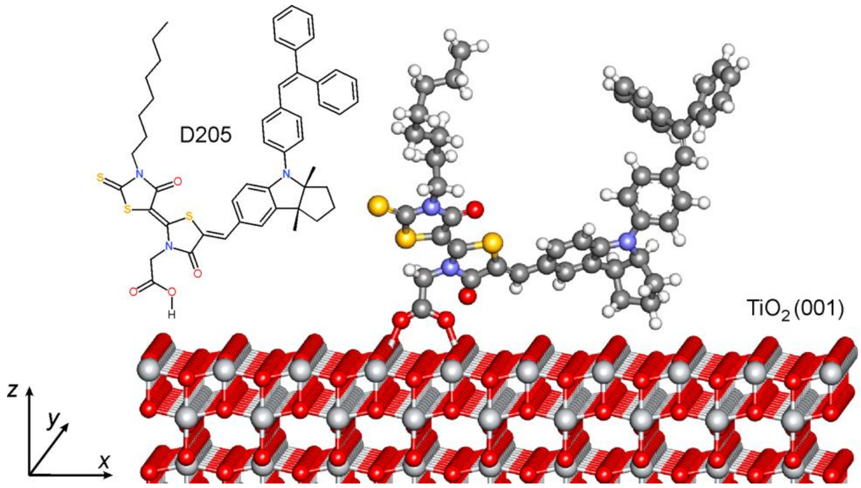

Figure 3.2. Chemical structure of a free D205 dye and the illustration of the D205 dye, anchored covalently to TiO_2 (001) slab by the carboxylic group, as shown with *ball-and-stick* representation.

Recently, Zhou and co-workers [41] re-parameterized the MA parameters for TiO_2 by re-fitting the Buckingham potential parameters for TiO_2 by the 12-6 Lennard-Jones (LJ) potential energy function. These 12-6 LJ potential parameters adopted for Ti and O atoms were subsequently validated by MD simulations in terms of the TiO_2 interactions with solvents and small ligands [41-44]. Therefore, we used these LJ parameters to simulate TiO_2 anatase, as summarized in Table 3.1. Van der Waals interactions were calculated using r_{cutoff}=1.4 nm. Electrostatic interactions were calculated using the particle mesh Ewald (PME) technique beyond a real-space cutoff of r_{cutoff}=1.4 nm. The coordinates of all TiO_2 atoms were kept rigidly fixed in their crystal lattice positions. For mixed non-bonded interactions between TiO_2, the dye, and solvent molecules, the Lorentz-Berthelot combination rules were used [45].

Table 3.1. Non-bonded 12-6 LJ potential parameters for TiO_2 anatase [41].

Interactions	ε_{ij} (kJ/mol)	σ_{ij} (nm)
Ti-Ti	2.427	0.220
Ti-O	1.757	0.272
O-O	1.297	0.324

The all-atom force field for the D205 dye was derived in this work. The DFT optimized length of the Ti-O and angle Ti-O-C bonds in the D205-TiO_2 conjugate were used to set up classical MD simulations. The FF stretching constants for the Ti-O bonds were adapted from ref. [24]. In MD simulations, the D205 dye possesses the full-length octyl chain, as shown in Figure 3.2.

Many ionic liquids have very attractive electrochemical properties for DSSC devices as electrolytes. Therefore, the structure and dynamics of most popular ILs were systematically examined with MD simulations [9, 46-49]. Mondal and Balasubramanian quantitatively predicted the physicochemical properties of the set of 1-butyl-3-methylimidazolium-based ILs, such as $BmimPF_6$ and BmimTFO, by using classical MD simulations, where the non-bonded interactions are described with the 12-6 LJ potential [50]. The partial charges were derived from the well-established CLaP force field, developed by Lopes et al. [51]. A good quantitative agreement with experimental measurements for the density, surface tension, enthalpy of vaporization, and ion diffusion coefficients allowed us to use these potential models for our MD simulations.

3.2.3 MD simulation setup

All the MD simulations were carried out in the canonical (*NVT*) ensemble. Each system was firstly energy-minimized and then pre-equilibrated for 5 ns before accumulating productive MD runs. After which, the system was sampled for 100 ns. The reference temperature of 298.15 K was kept constant using the velocity rescaling weak coupling scheme [52] with the coupling constant τ_T of 0.1 ps. The initial atomic velocities were generated with a Maxwellian distribution at the given absolute temperature. Periodic boundary conditions were applied to all three directions of the rectangular box. Electrostatic interactions were described by the particle mesh Ewald (PME) approach [53] using the long-range cutoff of 1.4 nm. The cutoff distance of Lennard-Jones interactions was also equal to 1.4 nm. The MD simulation time-step was set to 0.5 fs, with the neighbor list updates every 10 fs. The MD simulations were carried out by using the GROMACS 2016.3 software package [54]. Molecular graphics and visualization were performed using VMD 1.9.3 [55]. On the figure 3.3 these is the simulation box provided.

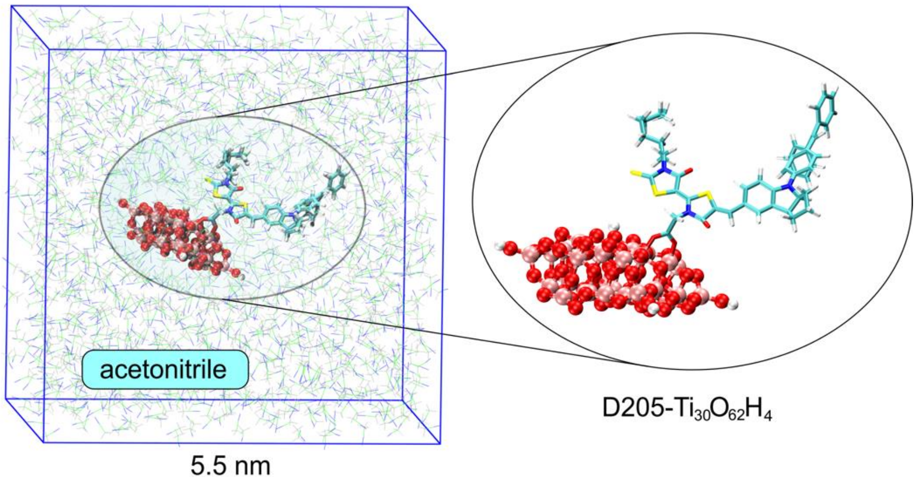

Figure 3.3. Example of a MD simulation box, containing the D205-$Ti_{30}O_{62}H_4$ conjugate in explicit AN solution (*left*). The representative snapshot of the equilibrated D205-$Ti_{30}O_{62}H_4$ conjugate (*right*).

3.3. Results and Discussion

Theoretical and computational modeling is a powerful tool to investigate and characterize the structural, electronic, and optical properties of dye-TiO_2 conjugates as the main components of dye-sensitized solar cells (DSCs). Therefore, we first performed the benchmarking of available DFT methods to select the theory level, enabling us to resemble electronic properties and photovoltaic characteristics of small-sized TiO_2 anatase nanoparticles.

3.3.1. Structure and Electronic Properties of Isolated $Ti_{30}O_{62}H_4$ Anatase Nanoparticle

A TiO_2 anatase nanoparticle was represented by means of a $Ti_{30}O_{62}H_4$ cluster. The starting geometry for the structural optimization of the cluster was cut from the X-ray structure of the bulk anatase. It has been shown that $(TiO_2)_n$ clusters with n≥24 resemble electronic properties and the bandgap between occupied and unoccupied molecular orbitals of bulk anatase [12, 14, 21, 56, 57]. The geometry of $Ti_{30}O_{62}H_4$ was optimized at the HSEH1PBE/TZV theory level. This structure was further used as a starting configuration for MD simulations.

The optical energy bandgap for $Ti_{30}O_{62}H_4$ was computed at various levels of theory in the PCM-acetonitrile solution evaluated as (*i*) vertical excitation energy

($S_0 \rightarrow S_1$) and (*ii*) one-electron Kohn-Sham eigenvalues HOMO and LUMO difference, as summarized in Table 3.2.

Table 3.2. Electronic properties of HSEH1PBE/TZV-optimized $Ti_{30}O_{62}H_4$ nanoparticle calculated in the PCM-acetonitrile solution with various TDDFT levels.

Theory Level	Electronic Transition	Excitation energy (eV, nm)	Oscillator strength (*f*)	Configuration (HOMO = H, LUMO = L)	HOMO-LUMO Energy Difference (eV)
CAM-B3LYP/TZV	$S_0 \rightarrow S_1$	3.6031 (344)	0.0086	H→L (0.19230) H→L+1 (-0.13050) H→L+6 (0.42827)	7.40
CAM-B3LYP/TZVP	$S_0 \rightarrow S_1$	3.6130 (343)	0.0085	H→L (0.21306) H→L+1 (-0.11177) H→L+6 (0.44282)	7.42
B3LYP/ TZV	$S_0 \rightarrow S_1$	2.7330 (454)	0.0001	H→L (0.68720)	4.51
HSEH1PBE/ TZV	$S_0 \rightarrow S_1$	2.9100 (426)	0.0002	H→L (0.69126)	4.23
M06-2X/ TZV	$S_0 \rightarrow S_1$	4.1116 (302)	0.0010	H→L+1 (0.19881)	7.67
LC-wPBE/ TZV	$S_0 \rightarrow S_1$	3.8894 (318.8)	0.0092	H→L (0.17818) H→L+6 (0.37052)	9.73

Considering the small size of the $Ti_{30}O_{62}H_4$ nanoparticle, we expect some overestimation of the energy bandgap compared to the experimental value for bulk anatase (3.2 eV) [14, 31]. As can be noted from Table 3.2, the CAM-B3LYP value of 3.60 eV for the optical transition $S_0 \rightarrow S_1$ is in reasonably good agreement with the experiment. In contrast, the B3LYP and HSEH1PBE functionals result in some underestimation of the energy gap to be at 2.73-2.91 eV, respectively. Significant overestimation of the optical bandgap up to 3.89-4.11 eV was found by the LC-wPBE and M06-2X functionals. We also noted that the excitation energy $S_0 \rightarrow S_1$ has only minor basis set dependence, as seen from comparing the CAM-B3LYP/TZV and CAM-B3LYP/TZVP results. It should also be pointed out that the low intensity calculated for the $S_0 \rightarrow S_1$ oscillator strength confirms the optically symmetry forbidden character of the electronic transition in $Ti_{30}O_{62}H_4$, as expected for an indirect bandgap semiconductor [14]. To sum up, these results suggest that the TD-CAM-B3LYP/TZV method is one of the available reliable tools for estimating the electronic properties of small TiO_2 particles.

3.3.2. Structure of D205-$Ti_{30}O_{62}H_4$ Conjugate in Acetonitrile

To elucidate the role of the acetonitrile environment on the structure and conformational dynamics of a TiO_2-anchored D205 dye, we carried out classical MD simulations. The $Ti_{30}O_{62}H_4$ nanoparticle was placed in the middle of the MD box so that its geometry was rigidly fixed during MD sampling. The D205 indoline dye was covalently bound to two uncoordinated Ti surface atoms of the $Ti_{30}O_{62}H_4$ nanoparticle, as shown in Figure 3.2, *right*. The geometry of the D205 dye was free to relax during MD sampling.

Figure 3.4 shows a series of the D205-$Ti_{30}O_{62}H_4$ structures taken at different times along the MD trajectory. Since the coordinates of the $Ti_{30}O_{62}H_4$ nanoparticle were rigidly fixed, these MD snapshots represent the time-evolution of conformational dynamics of the D205 dye during the MD sampling. It can be noted that the most conformationally labile fragments of the D205 dye were localized at the peripheral diaryl-substituted ethylene moiety (Figure 3.4).

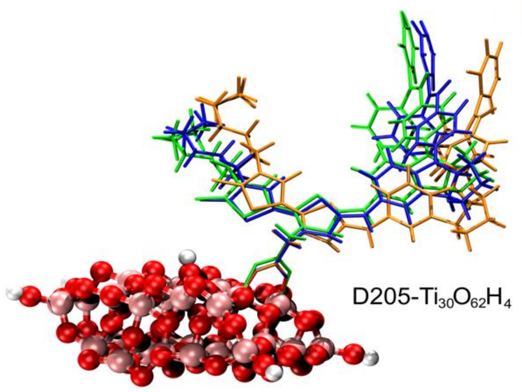

Figure 3.4. Superpositions of a series of MD snapshots of a D205 dye anchored to the $Ti_{30}O_{62}H_4$ nanoparticle taken at 10 ns time intervals.

It has been shown that the spectral properties of indoline-based dyes depend on the environment [8, 19, 58-61]. Therefore, we used a series of MD-equilibrated structures of the D205-$Ti_{30}O_{62}H_4$ conjugate to study how environment-induced conformational changes can further govern the electronic structure and a solvatochromic shift in absorption spectra of a D205 dye at the TiO_2/AN interfaces. For computational reasons, acetonitrile molecules were omitted upon TDDFT calculations.

3.3.3. Absorption Spectra and Solvatochromic Shift of D205 Dye

Although the B3LYP exchange−correlation functional is commonly employed in investigating the absorption spectra of the organic dyes [62-64]. However, it is also well-recognized that it fails with excited-state calculations involving charge-transfer excitations, which is crucial for dye-TiO_2 conjugates [12, 22, 65, 66]. Therefore, TDDFT calculations were done using exchange−correlation functionals combined with the Coulomb−attenuating method (CAM-B3LYP) [36]. It has been shown that the TD-CAM-B3LYP approach performed well for indoline-based dyes [67].

Figure 3.5 shows the optical spectra of a free D205 dye calculated by the TD-CAM-B3LYP/TZV method using the PCM model for the acetonitrile solution. In the region of 250-700 nm, we observe two absorption bands located at 328 nm and 423 nm, respectively. The wavelength positions of the peaks and the relative intensity (related to the oscillator strength) agree with those reported in the literature both for the experiment and for previous calculations [58]. We found a small redshift of the long-wavelength band upon anchoring a D205 dye to the $Ti_{30}O_{62}H_4$ nanoparticle. For the HSEH1PBE/TZV-optimized D205-$Ti_{30}O_{62}H_4$ conjugate, the two long-wavelength absorption bands were found at 328 nm and 439 nm, respectively. Thus, the long-wavelength band of the D205 dye was redshifted up to 860 cm^{-1} upon the bonding to TiO_2.

The averaged absorption spectrum of a D205 dye in explicit acetonitrile solution was generated from the six MD snapshots of the D205-$Ti_{30}O_{62}H_4$ conjugate taken from classical MD trajectory, some of which are shown in Fig. 3.5. It can be noted an increasing redshift of the absorption maximum upon going from vacuum to the acetonitrile solution is in accordance with experimental results [58]. For the MD-relaxed D205-$Ti_{30}O_{62}H_4$ conjugate, the absorption bands were shifted to 339 nm and 479 nm, respectively. Therefore, the solvatochromic shift of the D205 at the TiO_2/AN interface, estimated as the energy difference between the maximum of the long-wavelength absorption band of the DFT-optimized and MD-relaxed D205-$Ti_{30}O_{62}H_4$ conjugates, was found to be 1900 cm^{-1}.

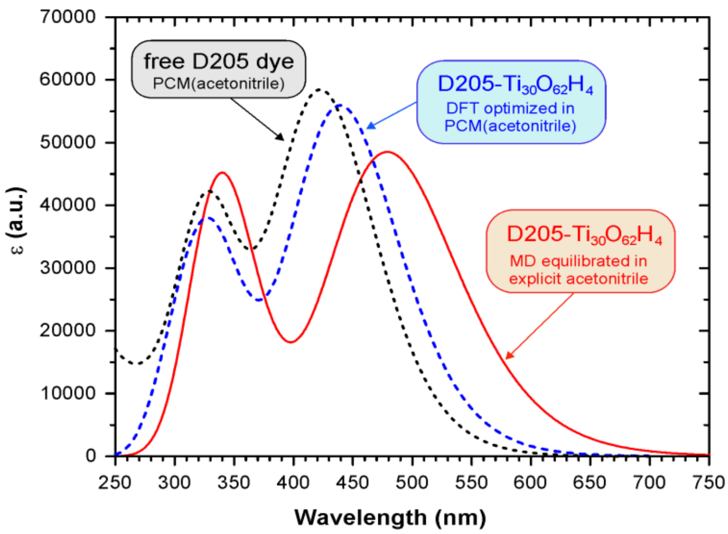

Figure 3.5. Comparison of UV–vis absorption spectra for DFT-optimized and MD-relaxed D205-$Ti_{30}O_{62}H_4$ conjugate, as predicted by TD-CAM-B3LYP/TZV calculations, demonstrating a redshift of the long-wavelength absorption band in the acetonitrile solution. An analogous spectrum corresponding to the free D205 dye is also provided for comparison.

To elucidate the mechanism underlying electron injection in the D205-$Ti_{30}O_{62}H_4$ conjugate, the excitation energies, oscillator strengths, and configurations for the most relevant excited states of the MD-relaxed D205-$Ti_{30}O_{62}H_4$ conjugate were evaluated using the CAM-B3LYP functional and the TZV basis set, as summarized in Table 3.3. The corresponding isosurfaces of frontier molecular orbitals are shown in Figure 3.6. The molecular orbitals were calculated for the representative D205-$Ti_{30}O_{62}H_4$ structure taken from MD simulations, in which AN molecules were omitted.

Table 3.3. Electronic properties of MD-relaxed D205-$Ti_{30}O_{62}H_4$ conjugate calculated by TD-CAM-B3LYP/TZV(PCM-acetonitrile).

Transition	Excitation energy (eV, nm)	Oscillator strength (*f*)	Configuration (HOMO = H, LUMO = L)
$S_0 \rightarrow S_1$	2.5657 (483)	1.1342	H→L+5 (0.59844)
			H-1→L+5 (0.27803)
$S_0 \rightarrow S_2$	3.3330 (372)	0.0000	H→L (0.68975)
$S_0 \rightarrow S_3$	3.4223 (362)	0.0005	H→L+3 (0.47701)
			H→L+2 (0.24271)
			H→L+1 (-0.27776)
$S_0 \rightarrow S_4$	3.4414 (360)	0.0001	H→L+1 (0.63685)
			H→L+2 (0.19562)
$S_0 \rightarrow S_5$	3.4670 (357)	0.0021	H→L+3 (0.60009)
			H→L+2 (0.30231)
$S_0 \rightarrow S_6$	3.4887 (355)	0.0083	H-3→L+5 (-0.49974)
$S_0 \rightarrow S_7$	3.5571 (348)	0.8574	H-2→L+5 (0.32725)
			H-1→L+5 (0.37590)
			H→L+5 (-0.11016)

3.3.4. Nature of Excited-States of D205-$Ti_{30}O_{62}H_4$

A crucial feature of an efficient organic sensitizer is its intramolecular charge-transfer property, so that there should be an efficient transfer of charges from the electron-rich donor dye moiety into the electron acceptor semiconductor band [17, 68, 69]. It has been well established that, in a DSSC cell, efficient photoelectronic conversion can occur when the following criteria are met [9, 17]: (*1*) To achieve efficient light harvesting, the energy level of the highest occupied molecular orbital (HOMO) of a dye must be located above the HOMO energy level of TiO_2; (*2*) The HOMO energy level of a dye must be established below the redox couple of the I^-/I_3^- electrolyte; (*3*) To enhance efficient charge injection, the energy level of the lowest unoccupied molecular orbital (LUMO) of a dye must be situated above, and close to, the conduction band of TiO_2.

Figure 3.6 compares the Kohn–Sham (KS) orbital energy diagram of a free D205 dye and the $Ti_{30}O_{62}H_4$ nanoparticle. The energy levels of HOMO and LUMO of the dye were calculated to be –7.9278 eV and –1.7712 eV, respectively, while the corresponding energy for the MOs of $Ti_{30}O_{62}H_4$ was found to be -9.5477 eV and -2.1497 eV by the TD-CAM-B3LYP/TZV calculation. Thus, the HOMO-LUMO alignment of the dye and TiO_2 suggests the favorable migration direction for a photoexcited electron from the D205 donor toward the $Ti_{30}O_{62}H_4$ acceptor.

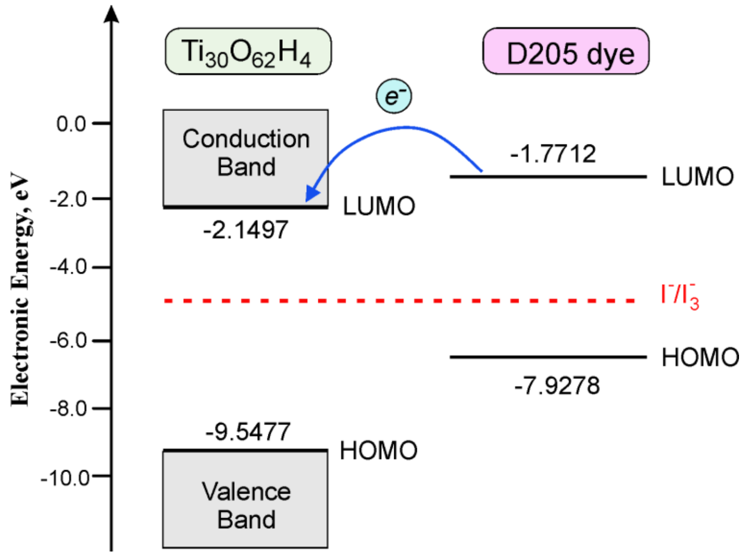

Figure 3.6. Orbital energy diagram of the $Ti_{30}O_{62}H_4$ nanoparticle and a free D205 dye calculated by the TD-CAM-B3LYP/TZV(PCM-acetonitrile) method.

Figure 3.7 shows the frontier MOs and their energy in eV for the representative MD-equilibrated D205-$Ti_{30}O_{62}H_4$ conjugate calculated by the TD-CAM-B3LYP/TZV method using the PCM model for the acetonitrile solution. As can be seen, in the D205-$Ti_{30}O_{62}H_4$ conjugate, the HOMOs are predominantly located at the D205 dye, while the LUMOs are mainly delocalized over the $Ti_{30}O_{62}H_4$ nanoparticle. The calculated MO alignment in the D205-$Ti_{30}O_{62}H_4$ conjugate illustrates how an electron is transferred from a D205 moiety towards the TiO_2 semiconductor. The TD-DTF calculations clearly show that when the dye is adsorbed onto the TiO_2 surface, the HOMOs of the D205-$Ti_{30}O_{62}H_4$ conjugate are exclusively localized on the dye moieties. The electronic π-π coupling between the dye and TiO_2 is weak due to the presence of the saturated methylene group CH_2 in the anchoring moiety. In contrast, the LUMOs of the D205-$Ti_{30}O_{62}H_4$ conjugate are delocalized over the energy levels of the $Ti_{30}O_{62}H_4$ nanoparticle, which should allow electrons to transfer efficiently from the dye to the semiconductor.

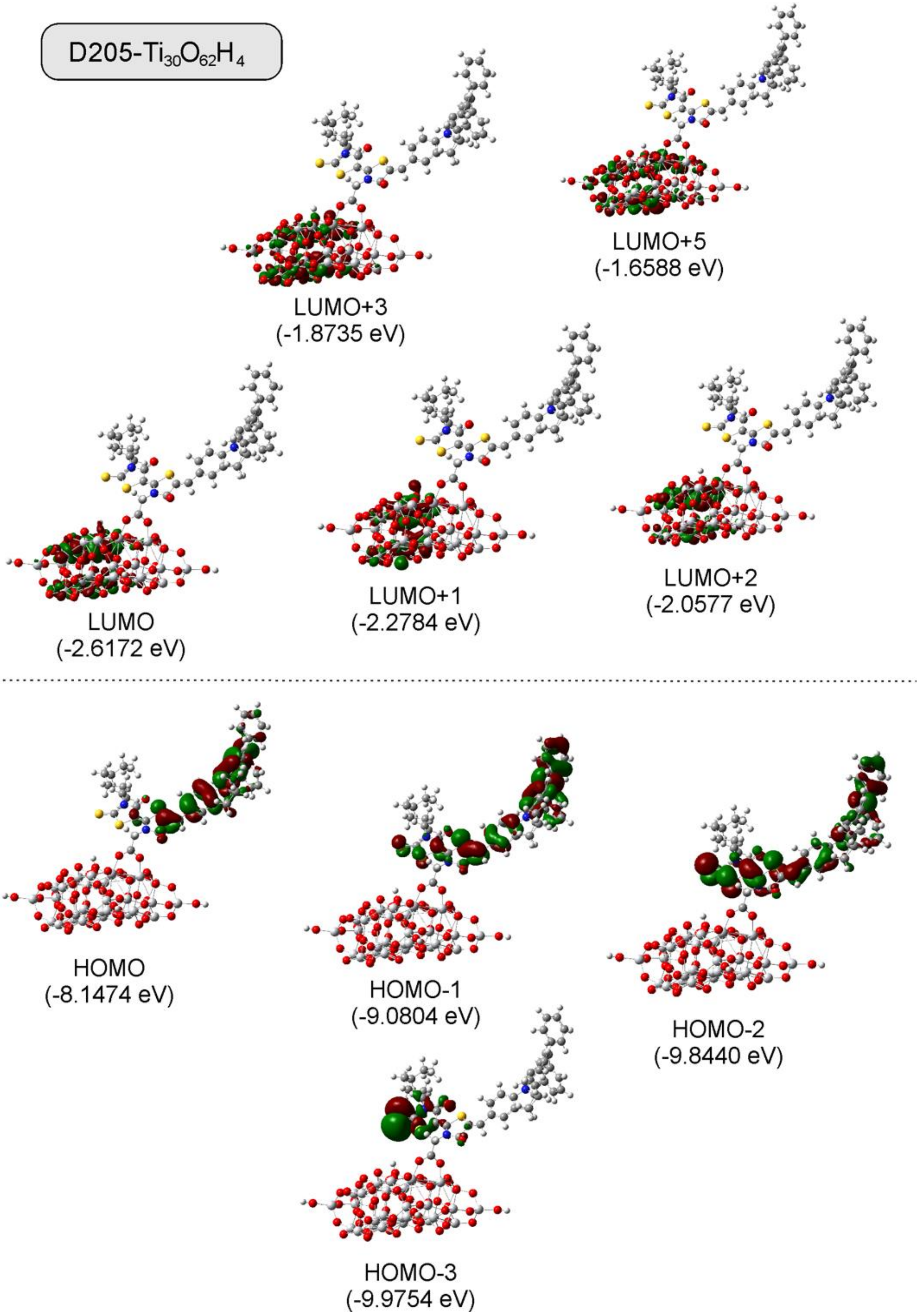

Figure 3.7. Frontier molecular orbitals of a MD-equilibrated D205-$Ti_{30}O_{62}H_4$ conjugate calculated by the TD-CAM-B3LYP/TZV(PCM-acetonitrile) method. The MO energy level in eV is given in the brackets.

3.3.5. Mass density profiles of ionic liquids (ILs) and acetonitrile (AN) at TiO_2 interface

To elucidate the adsorption behavior of ILs and AN on TiO_2 surface, we first studied solvent–TiO_2 interactions and the structure of adsorbed solvent layers at the TiO_2 surface. Bulk $BmimPF_6$ (365 ion pairs) and BmimTFO (352 ion pairs) (see Figure 3.8.*a* for molecular structure) were simulated at contact with the rigid TiO_2 slab. The systems were sampled at the *NVT* ensemble up to 50 ns and the last 20 ns were taken for the analysis. The MD snapshots of the final configurations of $Bmim/PF_6TiO_2$, BmimTFO/TiO_2, and AN/TiO_2 are shown in Figure 3.8.*b-d*. The MD simulations reveal that both ILs form the ordered adsorption layers of $Bmim^+$ and either PF_6^- or TFO^- counterions, respectively. The IL ordering was observed up to several layers from the TiO_2 surface towards the bulk IL phase. This adsorption behavior is consistent with the data published for other ILs [28, 29, 46-48, 50, 70, 71].

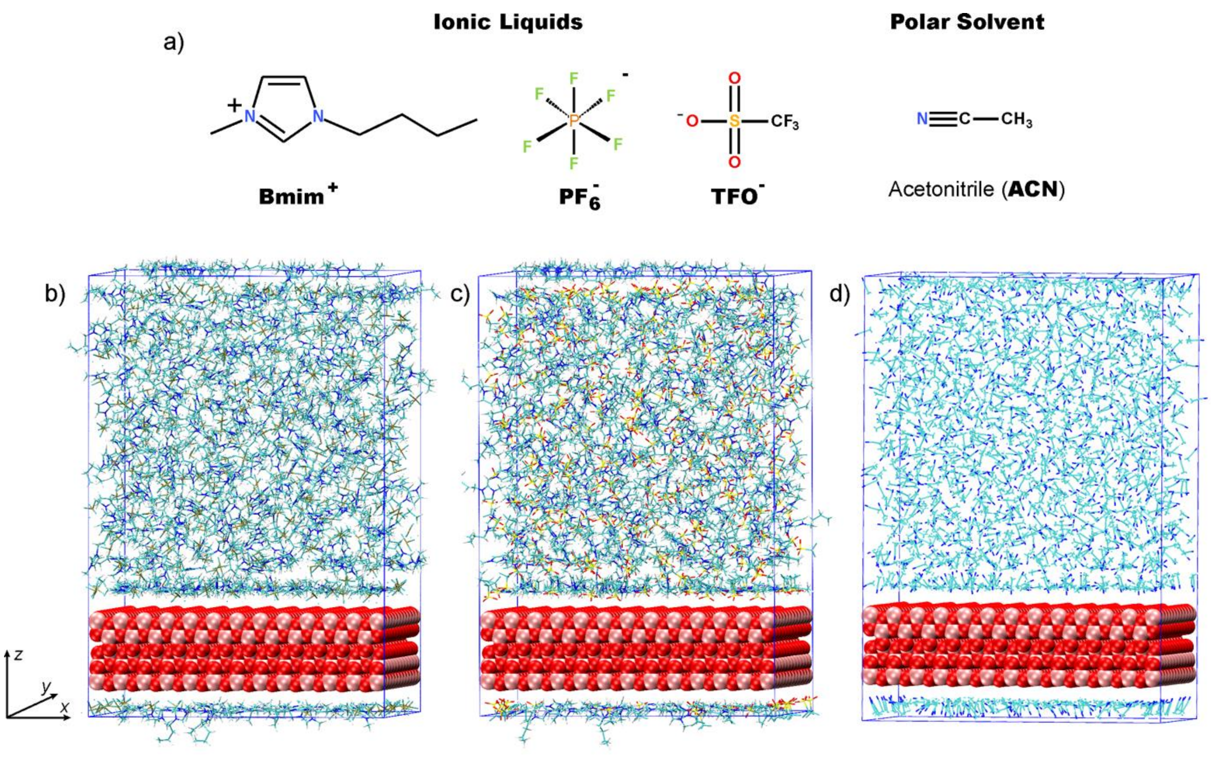

Figure 3.8. Molecular structures of the studied ionic liquids and acetonitrile AN (*a*). The snapshots of the equilibrated rectangular simulation cells containing 1-butyl-3-methylimidazolium hexafluorophosphate $BmimPF_6$ (*b*) and trifluoromethanesulfonate BmimTFO (*c*), and AN (*d*) equilibrated at the TiO_2 anatase interface.

Figure 3.9. shows MD snapshots and the mass density profiles calculated along the *z*-axis of the simulated box normal to the TiO_2 slab (Fig. 3.9*b*) solvated with $BmimPF_6$, BmimTFO, and AN, respectively. We found that the density of $BmimPF_6$ and BmimTFO depend strongly on distance calculated from the TiO_2 surface along the z-axis, as shown in Figure 3.9. At the distances from 0 up to 1.5 nm from the surface, three density peaks could be identified. For $BmimPF_6$, the position of these peaks was found to be at 0.50, 0.87, and 1.28 nm, respectively. In the case of BmimTFO, the peak positions are at 0.48, 0.64, and 0.94 nm, respectively. The position of these peaks coincides with the ordered layers of the imidazolium cations, as seen in the top panels of Figures 4*a* and 4*c*. These finding are in the agreement with published results of MD simulations of similar systems, where authors reported that strong adsorption of IL ions onto charged TiO_2 surface, leading to the interfacial ions ordering and dense packing of adsorbed species [28, 29, 46, 72]. Our MD simulations demonstrate that at distances over 1.5 nm, the bulk mass density of the studied ILs agrees well with the experimental values. The experimental density values of $BmimPF_6$ and BmimTFO are reported to be 1368 and 1297 kg/m^3 at 298.15 K, respectively [50, 73-75]. Moreover, these simulated mass densities of the ILs agree well with the density of the pure ILs, simulated for the *NPT* ensemble (Figures 3.9*b* and 3.9*d*).

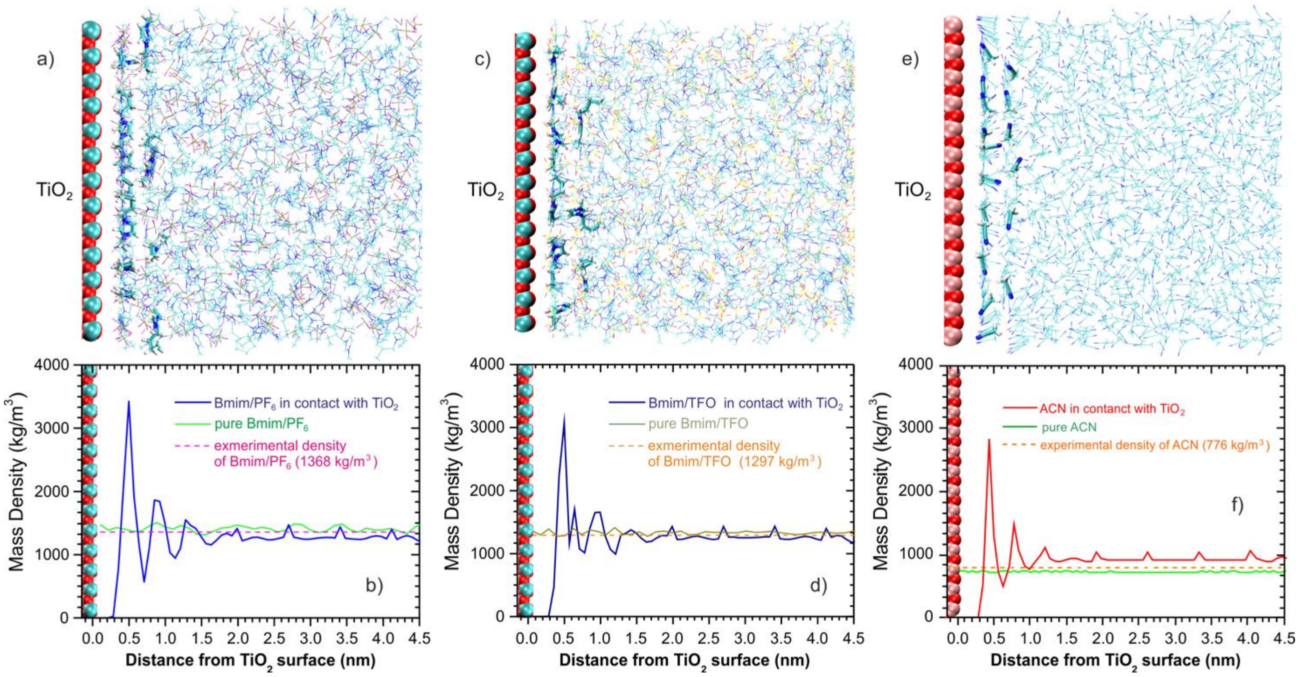

Figure 3.9. The comparison of the MD estimated mass density of pure $BmimPF_6$, BmimTFO, and AN and the mass density of these solvents at the TiO_2 interface. Panels *a*, *c*, and *e* show snapshots of $BmimPF_6/TiO_2$, $BmimTFO/TiO_2$, and AN/TiO_2 interfaces. Some solvent molecules located at the two ordered interfacial layers are highlighted. Comparison of the MD estimated and experimental mass densities of $BmimPF_6$ (*b*), BmimTFO (*d*), and AN (*f*), respectively. The mass density of pure ILs and AN were taken from the control MD simulations carried out at the *NPT* ensemble. The dotted lines represent the experimental mass density of the bulk ILs and AN, respectively.

According to the experimental data, the mass density of AN at 298.15 K is reported to be 775.9 kg/m^3 [76]. These data can be used for comparison and validation of our MD results, as shown in Figure 3.9*f*. One can see that the mass density of pure AN simulated at the isothermal-isobaric ensemble is in perfect agreement with the experimental values. We also noted some 5-7 % increase in the mass density of AN due to its contacts with the polar TiO_2 surface. In addition, similarly to the above-discussed density distributions of the ILs, the density plot of AN revealed up to three peaks close to the TiO_2 interface. The peak position is at 0.42 nm, 0.78 nm, and 1.21 nm, respectively. These density peaks can be attributed to the three ordered layers of AN molecules, as shown in Figure 4*e*.

3.3.6. Microscopic structure of solvent molecules at TiO_2 interface

The local microscopic structure of ILs and AN at the TiO_2 interface was examined by the calculation of the radial distribution functions (RDFs). To identify preferred absorption mode, the RDF's plots between some selected atoms of either $BmimPF_6$ or BmimTFO and all titanium and oxygen atoms of the anatase slab were calculated as shown in Figs. 3.10 and 3.11, respectively.

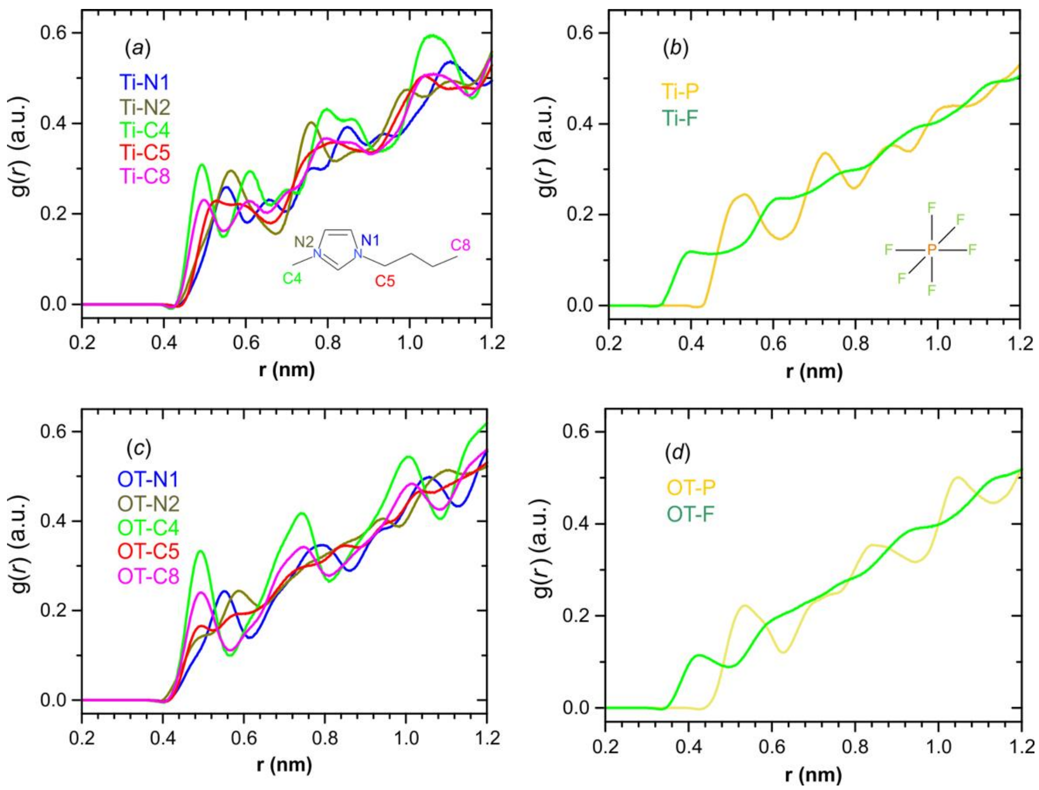

Figure 3.10. The RDFs plots calculated between the selected atoms of $BmimPF_6$ and the Ti and O (OT) atoms of TiO_2, respectively.

The RDF plots show well-defined peaks at the short distance 0.4-0.5 nm from the TiO_2 surface, indicating that the atomic structure is characterized by the short-range order. The analysis of the RDF peaks calculated between BmimTFO and the TiO_2 slab shows that the anion of TFO^- is coordinated onto the inorganic interface through the interactions between Ti atoms of the anatase slab and oxygen atoms of the anion. In this case, the center-of-mass is spread between the sulfur atom and the trifluoromethyl group as the electron-withdrawing group. As in the case of $BmimPF_6$, the $Bmim^+$ and oxygen atoms of TiO_2 coordinate by the imidazolium ring as the center of mass of the cation. Table 3.4. summarizes the RDF positions of the first two coordination shells for the $BmimPF_6$ and BmimTFO - composed systems.

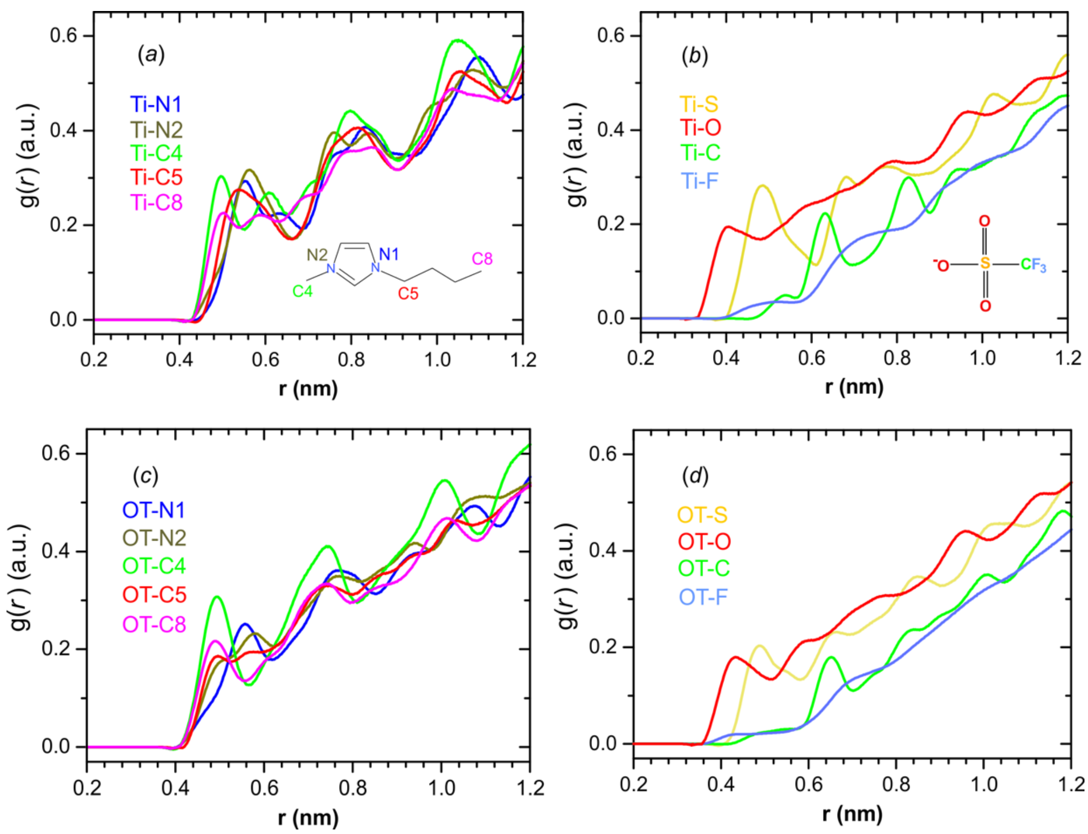

Figure 3.11. The RDFs plots calculated between the selected atoms of BmimTFO and the anatase Ti and O (OT) atoms, respectively.

As can be noted from Table 3.4., the strongest interactions occur between the Ti atoms and the fluorine atoms of PF_6^-. The difference of the peak intensities related to the PF_6^- could be explained by the position of the phosphorous atom as a center-of-mass of the anion. Besides, the interactions of the $Bmim^+$ ions and the OT atom are driven by the interaction of the imidazolium ring, mimicking interactions with the aromatic π^+-ring in real sytems. These results are in agreement with Malali and Foroutan [46]. It was shown that the arrangement of the $Bmim^+$ cations could be explained by the electrostatic and van der Waals interactions between the imidazolium ring and the TiO_2 surface.

The RDF plots for TiO_2/AN are shown in Figure 3.12. The position of the first RDF peaks is summarized in Table 3.5. It could be noted from Figure 3.12 and Table 3.5 that the essential interactions occur between the nitrogen atom of the cyano group of AN and Ti atoms of anatase. This type of interaction originates from the nature of an AN molecule, where the electronegativity difference between the triple bond of carbon and nitrogen produces a dipole moment.

Table 3.4. The peak positions of the first two coordination shells based on RDFs between TiO_2 and $BmimPF_6$ and BmimTFO.

Interactions	$BmimPF_6$		BmimTFO	
	First peak (nm)	Second peak (nm)	First peak (nm)	Second peak (nm)
Ti – N1	0.56	0.66	0.55	0.76
Ti – N2	0.55	0.75	0.55	0.75
Ti – C4	0.49	0.61	0.49	0.61
Ti – C5	0.52	0.59	0.54	0.75
Ti – C8	0.49	0.60	0.49	0.58
Ti – F	0.40	0.60	–	–
Ti – P	0.51	0.71	–	–
Ti – S	–	–	0.48	0.66
Ti – O	–	–	0.40	0.58
Ti – C	–	–	0.53	0.62
Ti – F	–	–	0.50	0.71
OT – N1	0.55	0.79	0.55	0.75
OT – N2	0.49	0.58	0.50	0.56
OT – C4	0.49	0.68	0.49	0.68
OT – C5	0.49	0.57	0.49	0.55
OT – C8	0.49	0.69	0.49	0.75
OT – F	0.42	0.59	–	–
OT – P	0.52	0.72	–	–
OT – S	–	–	0.48	0.66
OT – O	–	–	0.43	0.58
OT – C	–	–	0.50	0.65
OT – F	–	–	0.42	0.71

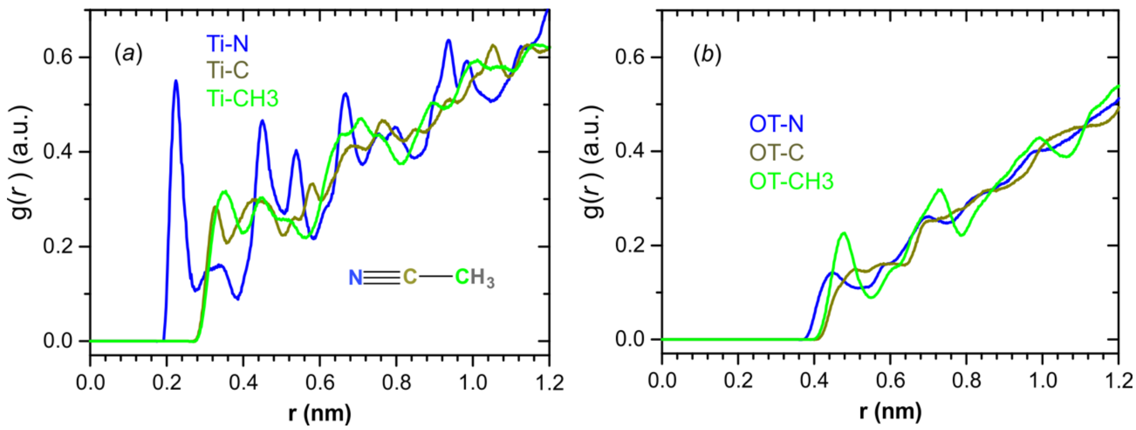

Figure 3.12. The RDFs plots calculated between AN heavy atoms and the anatase Ti (*a*) and OT (*b*) atoms, respectively.

Table 3.5. The RDF peak positions of the first coordination shells of AN/TiO_2.

Interactions	Acetonitrile	
	First peak (nm)	Second peak (nm)
Ti – N	0.22	0.33
Ti – C	0.32	0.43
Ti – CH_3	0.36	0.45
OT – N	0.45	0.59
OT – C	0.50	0.57
OT – CH_3	0.47	0.73

These MD results of AN molecules layering at the TiO_2 anatase meet the results of recent quasi-elastic neutron scattering (QENS) experiments, where the 3–4 immobile layers of AN molecules were also identified [77].

It should be noted that the observed alignment of the first layers of AN molecules agrees with the previous MD studies [9, 78]. Kislenko and co-authors studied the electrolyte/TiO_2 interface as the key element for a DSSC device. They showed that adsorbed AN molecules form a self-assembled monolayer at the anatase (101) surface. The effective dipole moments of acetonitrile molecules in the monolayer are directed away from the surface and produce a potential drop across the interface of ∼1.3 V [79].

3.3.7. Structure of surface-anchored D205 dye at TiO_2 interface

Indoline dyes are one of the highly efficient organic sensitizers used in dye-sensitized solar cells (DSSCs) [59, 80]. A D205 dye is an amphiphilic derivative of a D149 dye (Figure 1) [17], in which the ethyl chain is replaced by an octyl chain. D205 shows improved open-circuit photovoltage and gave higher conversion efficiency than D149 [81]. A lot of effort in the molecular design has been devoted to improving the cell performance of indoline dye-based solar cells [59, 60].

A D205 dye has push-pull systems with indoline derivative as donor and rhodanine units carrying anchor groups as acceptors. It is characterized by excellent performances since the presence of the long alkyl chain facilitates the self-assembly of a dye monolayer on the oxide surface that blocks the recapture of the photoinjected electrons by the triiodide ions. It has an efficiency of 8.43%, and according to the literature data, its efficiency could be enhanced by the usage of the TiO_2 interface as the active layer semiconductor and ionic liquids as the electrolyte for the regeneration of the dye [61, 80, 82].

It has been shown that the spectral properties of a D205 dye depend on the environment [58]. Therefore, it is crucial to understand how environmental effects can further govern the structure and dynamics of a D205 dye at the TiO_2/IL and TiO_2/AN interfaces.

The TiO_2 slab with the covalently bound D205 dye was first solvated with $BmimPF_6$ (376 cations of $Bmim^+$ and 376 anions of PF_6^-) and BmimTFO (363 cations of $Bmim^+$ and 363 anions of TFO^-). In our MD model, a D205 dye is anchored to TiO_2 by its carboxylic group attached to the rhodanine ring, as shown in Figure 3.1. Typical MD snapshots of the D205 dye attached to the flat TiO_2 (100) surface are shown in two different orientations in Figure 3.13.

Monti et al. characterized the adsorption of the D102 dye on an anatase (101) surface in the gas phase using classical MD simulations based on the reactive force field [19]. They showed that the most stable adsorbates were bound to the substrate through bidentate coordination of their carboxylic groups to the available Ti sites of the surface. In some rare cases, tridentate coordination was also observed, in which the carboxylic anchoring is reinforced by direct contacts between the sulfur atom protruding out of the acceptor ring and the outer atoms of the anatase slab. These types of binding determined the orientation of the dye in relation to the surface (which was around 60° as already observed by other authors) [33, 64, 83].

During our MD sampling, we found that the D205 dye favored being faced towards the bulk IL phase. Figure 8 shows that the rhodanine ring of the TiO_2-bound D205 is located within the first two adsorption layers of the ILs. The densely ordered layers of the adsorbed IL cations shield the direct contact of the D205 with the TiO_2 surface. Therefore, any surface stacking of the TiO_2-anchored D205 in ILs was not observed, which is often seen in control MD simulations of this system in a vacuum.

Figures 3.13*e-f* show the typical conformations of the TiO_2-anchored D205 dye in AN. The conformation of the D205 dye was similar in many aspects to those observed in the environment of $BmimPF_6$ and BmimTFO (Figures 3.13*a-d*). The rhodanine rings of the D205 dye were also located within the two interfacial layers of adsorbed AN molecules.

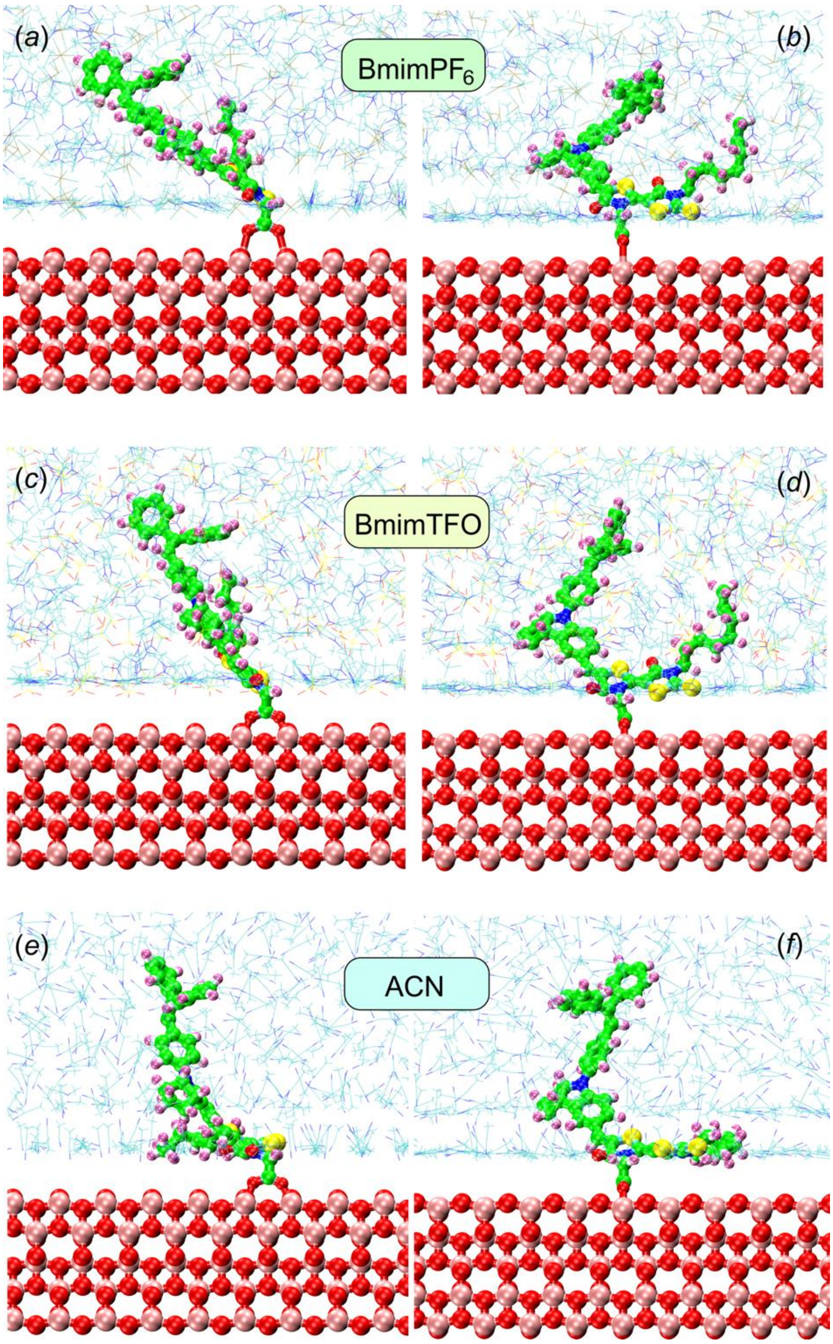

Figure 3.13. The MD snapshots of a D205 dye anchored to the TiO_2 anatase (100) surface and solvated with $BmimPF_6$ (*a-b*), BmimTFO (*c-d*), and AN (e-f) are given in positions of face (*right*) and sideways (*left*), respectively.

The D205 location at the TiO_2 interface is also estimated by averaging its mass density along the *z*-axis of the MD box. Figure 3.14 shows the overlap of the D205 mass density with the density plots of the studied ILs and AN. It can be seen that the D205 density spans a range from 0.35 nm up to 2.2 nm. Therefore, these data also suggest that the dye moiety of the TiO_2-anchored D205 favors residing within the IL/TiO_2 interfacial region. These findings are crucial for the rational design of DSSC devices because, from the experimental point of view, the physicochemical properties of the IL/TiO_2 interfacial layers differ from those in bulk in terms of local density, viscosity, polarity, etc.

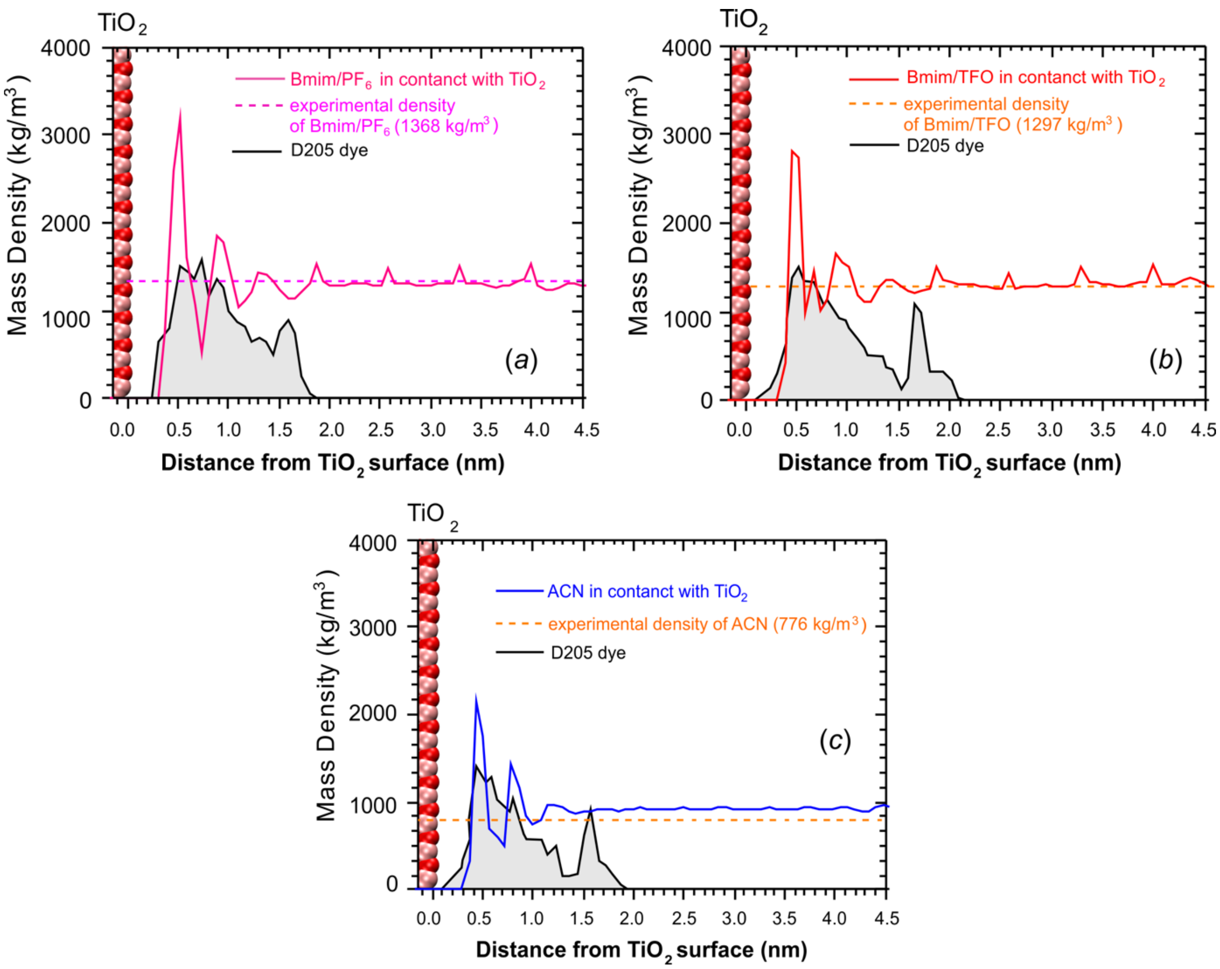

Figure 3.14. The comparison of the mass density distribution of the TiO_2-anchored D205 dye (*shaded area*) with the density of $BmimPF_6$ (*a*), BmimTFO (*b*), and AN (*c*), respectively. The mass densities were calculated along the *z* axis of the TiO_2 slab (see Fig. 3.3 for the axes defintion). For clarity, the D205 density was scaled by a factor of 20.

The structure and conformational dynamics of the TiO_2-anchored D205 dye play an essential role in operating a dye sensitizer for the dye-to-TiO_2 electron transfer process. Figure 3.15 shows overlaps of initial and final conformations of a D205 dye taken during MD simulations in $BmimPF_6$ and BmimTFO, respectively. One can notice that despite the rigid chemical anchoring to the TiO_2 surface, the D205 moiety remains conformational labile, and flexible. The most conformationally labile fragments of the D205 dye were localized at the octyl tail and peripheral diaryl-substituted ethylene moiety (Figure 3.15).

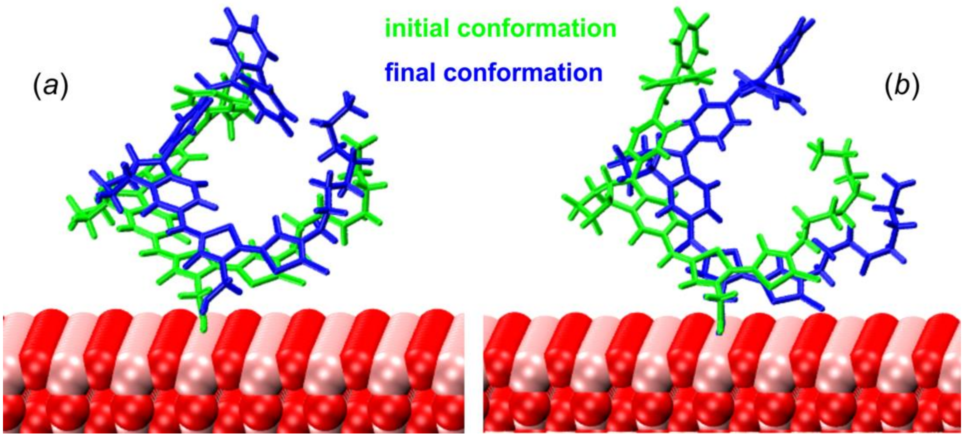

Figure 3.15. The conformational dynamics of the TiO_2-anchored D205 dye solvated in $BmimPF_6$ (*a*) and BmimTFO (*b*), respectively. The MD snapshots are shown for the initial structure (*green*) and the final conformation (*blue*) of D205 taken at the end of the 50 ns sampling.

To characterize the D205 location at the TiO_2/BmimTFO interface quantitatively, we plotted time-traces of the *z*-distance of some selected atoms of the dye from the TiO_2 surface (Figure 3.16). The time-traces of the *z*-distance of some selected atoms of D205 from the TiO_2 surface reveal that the dye molecule retains the well-defined geometry during the long-scale MD sampling. The sulfur atom of the thiazole moiety is found to be the closest to the TiO_2 slab. The location of the nitrogen atom of imidazole is around 1.09 nm, and the carbon atom of the peripheral ethenyl group is around 1.63 nm from the TiO_2 surface.

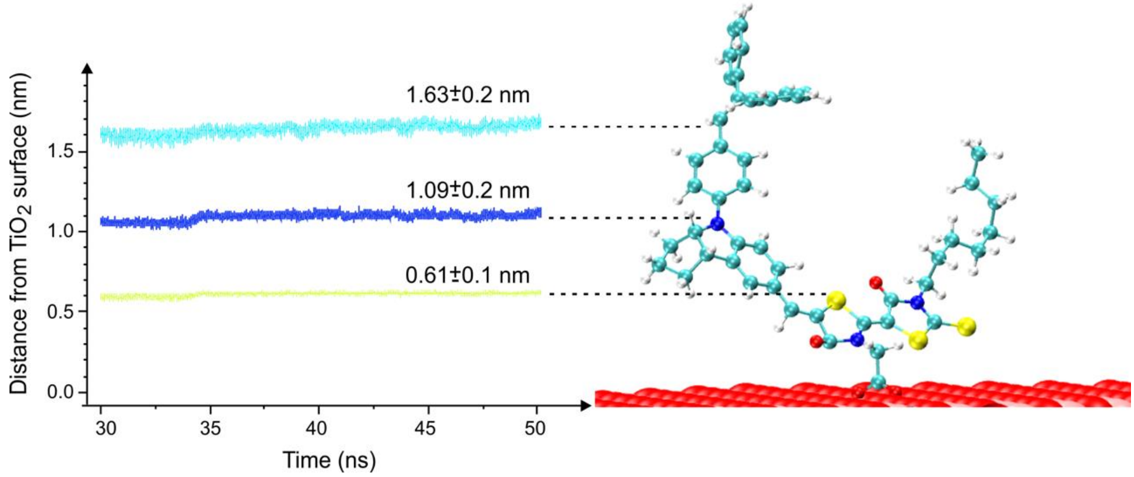

Figure 3.16. The time-traces of the *z*-axis position of some selected atoms of the TiO_2-anchored D205 dye plotted for the last 20 ns of the MD sampling. The system was solvated in BmimTFO. For clarity, a MD snapshot of TiO_2-bound D205 is also shown.

It has been shown that dye molecules anchored to TiO_2, are unlikely to undergo significant motions articulated from the anchoring point [77]. The QENS data for two small dyes, isonicotinic acid and bis-isonicotinic acid, attached to TiO_2 nanoparticles via carboxylate groups, revealed that the dye moieties were immobile and did not rotate around the anchoring groups on the time-scale between around 10 picoseconds and a few nanoseconds [77].

3.3.8. Adsorption and structure of free D205 dye at TiO_2 interface

To examine the role of the covalent anchoring of the D205 dye to the Ti_2O surface, we carried out a series of control MD simulations, in which a free dye molecule was adsorbed to the anatase surface by non-covalent interactions. It is well recognized that dye molecules bearing the protonated group –COOH has a low binding affinity to TiO_2 [3, 4, 82], so that the carboxylic group of the D205 dye was modelled at the deprotonated form $–COO^-$.

MD simulations demonstrated that a free dye, placed in a solvent at distances 0.4-0.6 nm from the TiO_2 interface, does not diffuse to bulk solvent and favors adsorption onto the anatase surface. We observed that the adsorbed D205 molecule shows significant variations in adsorption modes, which also depends on the environment.

In $BmimPF_6$, the D205 dye is found to be weakly bound to the anatase surface via the dissociated carboxylic group (Figures 3.17*a*-*b*). The D205 chromophore is centered above the $BmimPF_6/TiO_2$ interface. In contrast, the surface binding of the dye molecule occurs due to the adsorption of the rhodanine moiety flat to the $BmimTFO/TiO_2$ and AN/TiO_2, respectively (Figures 3.17*c*-*f*). The dissociated carboxylic group does not interact with the anatase surface and is faced towards bulk solvent. In addition, the non-polar aliphatic octyl chain of the rhodanine moiety favors interactions with solvent molecules instead of the TiO_2 binding, as seen in Figures 3.17*d* and 3.17*f*.

These findings suggest that, in the absence of the chemical anchoring of a dye onto the TiO_2 surface, the dye adsorption is characterized by significant heterogeneity in bound conformations, the degree, and the strength of dye-to-TiO_2 interactions. Moreover, the adsorption modes could be altered by the physicochemical properties of the environment. Altogether, MD simulations suggest that the appropriate chemical anchoring of the D205 dye to TiO_2 is crucial for its application in DSSC devices. The physical adsorption of a free dye may strongly affect the photovoltaic performance of a DSSC device due to broad variations of the distance and orientation between a dye and a TiO_2 surface, which in turn play a decisive role in the performance and rate of dye-to-semiconductor electron injection [3].

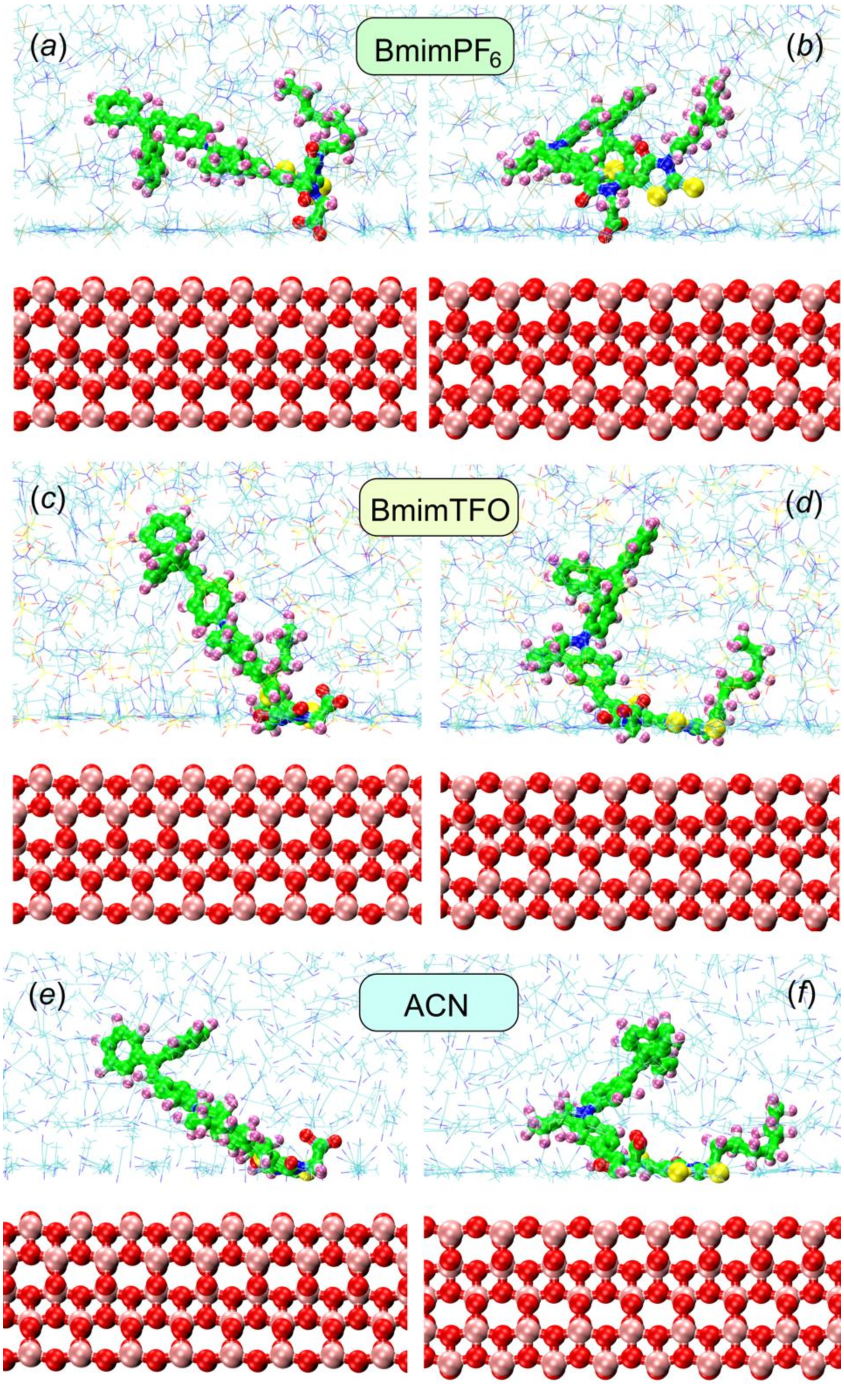

Figure 3.17. The MD snapshots of a free D205 dye adsorbed onto the TiO_2 anatase (100) surface and solvated with $BmimPF_6$ (*a*-*b*), BmimTFO (*c*-*d*), and AN (e-f) are shown with face (*right*) and sideways (*left*) orientations, respectively.

3.4. Conclusions

In this chapter, the effect of the various environments, such as 1-butyl-3-methylimidazolium-based ionic liquids with hexapluorophophate and trifluoromethanesulfonate anions, and polar organic solvent, acetonitrile, on the microscopic structure and dynamics of a D205 dye bonded covalently into the TiO_2-anatase surface were examined by using classical molecular dynamics simulations.

The structure and conformational dynamics of the D205 dye bonded covalently into the small-sized $Ti_{30}O_{62}H_4$-anatase nanoparticle were examined by using classical MD simulations combined with TDDFT excited-state calculations. It was investigated conformational dynamics and electronic properties of the D205 dye anchored to the TiO_2 anatase nanoparticle immersed in the AN solution as a representative electrolyte for DSSC devices. TD-CAM-B3LYP calculations of a series of MD-relaxed D205-$Ti_{30}O_{62}H_4$ conjugates were used to take into account the role of the AN environment on conformational heterogeneity of the dye chromophore.

It was determined that anchoring of the D205 to a TiO_2 nanoparticle induces an 860 cm^{-1} redshift of its long-wavelength band, as calculated by the TD-CAM-B3LYP/TZV approach using the PCM model of the acetonitrile solution. MD simulations in explicit AN revealed that the polar environment affects conformational dynamics of the TiO_2-anchored D205 dye. Its peripheral diaryl-substituted ethylene moiety shows essential conformational flexibility, which plays a critical role in tuning electronic π-π conjugation across an indoline chromophore. These environment-induced conformational changes lead to solvatochromic shifts in UV-vis absorption spectra of the D205 dye, so that its long-wavelength absorption band is further redshifted up to 1900 cm^{-1}.

The analysis of the excited-state properties and electronic structure of a free D205 dye and a $Ti_{30}O_{62}H_4$ nanoparticle revealed that the alignment between HOMO and LUMO energy levels of the dye and the semiconductor suggests the favorable driving force for photoinduced dye-to-TiO_2 electron transfer. These findings were also supported by the analysis of the frontier MOs of a D205-$Ti_{30}O_{62}H_4$ conjugate, providing further evidence for favorable energetics for electron ejection from the dye to the TiO_2 conduction band. Finally, the combined MD/TDDFT approach outlined in this work opens up the computationally reasonable alternative for reliable predictions of sensitizing properties of other dye-TiO_2 structures in an explicit solution.

It was found that counterions of $BmimPF_6$ and BmimTFO, and molecules of polar AN interact strongly with polar TiO_2 anatase (001) surface to form the well-ordered interfacial region composed of up to three solvent layers. The mass density distribution of the adsorbed $BmimPF_6$ and BmimTFO species allows estimating the thickness of the IL/TiO_2 interfacial region, which span a range from 0 up to 1.5 nm, respectively. Similarly, the TiO_2/AN interfacial region was found to be in a range of 0.0-1.3 nm, respectively.

MD simulations revealed that the densely ordered layers of the adsorbed IL cations and AN molecules shield the direct contact of the TiO_2-anchored D205 chromophore with the TiO_2 surface. The rhodanine ring of the D205 is located within the first two adsorption layers of the ILs and AN. Despite the rigid chemical anchoring of D205 to the TiO_2 surface, the dye moiety remained conformational labile, and flexible. The most conformationally labile fragments of the D205 dye were localized at the octyl tail and peripheral diaryl-substituted ethylene moiety. Control MD simulations of adsorption of a free dye revealed that the D205 dye molecule prefers binding onto TiO_2. Its adsorption is characterized by significant heterogeneity in bound conformations and the strength of dye-to-TiO_2 interactions. Therefore, the lack of the appropriate anchoring of the D205 dye may lead to a broad distribution of the distance and orientation between a dye and a TiO_2 surface, which may decrease the overall photovoltaic performance of a dye-sensitized solar cell device.

3.5. References for Chapter 3

1. Hagfeldt, A., et al., *Dye-Sensitized Solar Cells.* Chemical Reviews, 2010. **110**(11): p. 6595-6663.
2. De Angelis, F., et al., *Theoretical Studies on Anatase and Less Common TiO_2 Phases: Bulk, Surfaces, and Nanomaterials.* Chemical Reviews, 2014. **114**(19): p. 9708-9753.
3. Zhang, L. and J.M. Cole, *Anchoring Groups for Dye-Sensitized Solar Cells.* ACS Applied Materials & Interfaces, 2015. **7**(6): p. 3427-3455.
4. Ambrosio, F., N. Martsinovich, and A. Troisi, *What Is the Best Anchoring Group for a Dye in a Dye-Sensitized Solar Cell?* The Journal of Physical Chemistry Letters, 2012. **3**(11): p. 1531-1535.
5. Gao, Y., et al., *Photoinduced Charge Separation in Retinoic Acid on TiO_2: Comparison of Three Anchoring Modes.* The Journal of Physical Chemistry C, 2019. **123**(40): p. 24634-24642.
6. Tyagi, H., et al., *Introduction to Advances in Solar Energy Research*, in *Advances in Solar Energy Research*, H. Tyagi, et al., Editors. 2019, Springer Singapore: Singapore. p. 3-11.
7. Liu, X., et al., *Light controlled assembling of iodine-free dye-sensitized solar cells with poly(3,4-ethylenedioxythiophene) as a hole conductor reaching 7.1% efficiency.* Physical Chemistry Chemical Physics, 2012. **14**(19): p. 7098-7103.
8. Ito, S., et al., *High-conversion-efficiency organic dye-sensitized solar cells with a novel indoline dye.* Chemical Communications, 2008(41): p. 5194-5196.
9. Blazhynska, M.M., et al., *Recent advances in theoretical investigation of titanium dioxide nanomaterials. A review.* Kharkiv University Bulletin. Chemical Series., 2020. **34**: p. 6-56.
10. Fabregat-Santiago, F., et al., *Correlation between Photovoltaic Performance and Impedance Spectroscopy of Dye-Sensitized Solar Cells Based on Ionic Liquids.* The Journal of Physical Chemistry C, 2007. **111**(17): p. 6550-6560.
11. Gorlov, M. and L. Kloo, *Ionic liquid electrolytes for dye-sensitized solar cells.* Dalton Transactions, 2008(20): p. 2655-2666.
12. Berardo, E., et al., *Modeling Excited States in TiO_2 Nanoparticles: On the Accuracy of a TDDFT Based Description.* Journal of Chemical Theory and Computation, 2014. **10**(3): p. 1189-1199.
13. De Angelis, F., S. Fantacci, and R. Gebauer, *Simulating Dye-Sensitized TiO_2 Heterointerfaces in Explicit Solvent: Absorption Spectra, Energy Levels, and Dye Desorption.* The Journal of Physical Chemistry Letters, 2011. **2**(7): p. 813-817.
14. Nunzi, F., et al., *Structural and Electronic Properties of Photoexcited TiO_2 Nanoparticles from First Principles.* Journal of Chemical Theory and Computation, 2015. **11**(2): p. 635-645.
15. Valero, R., Á. Morales-García, and F. Illas, *Theoretical Modeling of Electronic Excitations of Gas-Phase and Solvated TiO_2 Nanoclusters and Nanoparticles of Interest in Photocatalysis.* Journal of Chemical Theory and Computation, 2018. **14**(8): p. 4391-4404.
16. Zhang, W., et al., *Rational Design of High-Efficiency Organic Dyes in Dye-Sensitized Solar Cells by Multiscale Simulations.* The Journal of Physical Chemistry C, 2018. **122**(44): p. 25219-25228.
17. Labat, F., et al., *First-Principles Modeling of Dye-Sensitized Solar Cells: Challenges and Perspectives.* Accounts of Chemical Research, 2012. **45**(8): p. 1268-1277.
18. Monti, A., et al., *A Dynamic View of Proton-Coupled Electron Transfer in Photocatalytic Water Splitting.* The Journal of Physical Chemistry C, 2016. **120**(40): p. 23074-23082.

19. Monti, S., et al., *Theoretical Investigation of Adsorption, Dynamics, Self-Aggregation, and Spectroscopic Properties of the D102 Indoline Dye on an Anatase (101) Substrate.* The Journal of Physical Chemistry C, 2016. **120**(5): p. 2787-2796.
20. Feng, J., et al., *First Principles Design of Dye Molecules with Ullazine Donor for Dye Sensitized Solar Cells.* The Journal of Physical Chemistry C, 2013. **117**(8): p. 3772-3778.
21. Oprea, I.C., et al., *Density Functional Theory (DFT) Study of Coumarin-based Dyes Adsorbed on TiO_2 Nanoclusters—Applications to Dye-Sensitized Solar Cells.* Materials, 2013. **6**(6): p. 2372-2392.
22. Luppi, E., I. Urdaneta, and M. Calatayud, *Photoactivity of Molecule–TiO_2 Clusters with Time-Dependent Density-Functional Theory.* The Journal of Physical Chemistry A, 2016. **120**(27): p. 5115-5124.
23. Yang, Z., et al., *Rational Design of Dithienopicenocarbazole-Based Dyes and a Prediction of Their Energy-Conversion Efficiency Characteristics for Dye-Sensitized Solar Cells.* ACS Applied Energy Materials, 2018. **1**(4): p. 1435-1444.
24. Milanese, J.M., et al., *Convergence of Computed Aqueous Absorption Spectra with Explicit Quantum Mechanical Solvent.* Journal of Chemical Theory and Computation, 2017. **13**(5): p. 2159-2171.
25. Zuehlsdorff, T.J. and C.M. Isborn, *Modeling absorption spectra of molecules in solution.* International Journal of Quantum Chemistry, 2019. **119**(1): p. e25719.
26. García-Iriepa, C., et al., *Simulation and Analysis of the Spectroscopic Properties of Oxyluciferin and Its Analogues in Water.* Journal of Chemical Theory and Computation, 2018. **14**(4): p. 2117-2126.
27. Feng, S., et al., *Dynamic Characteristics of Aggregation Effects of Organic Dyes in Dye-Sensitized Solar Cells.* ACS Applied Materials & Interfaces, 2015. **7**(40): p. 22504-22514.
28. Weber, H., M. Salanne, and B. Kirchner, *Toward an Accurate Modeling of Ionic Liquid–TiO_2 Interfaces.* The Journal of Physical Chemistry C, 2015. **119**(45): p. 25260-25267.
29. Weber, H., T. Bredow, and B. Kirchner, *Adsorption Behavior of the 1,3-Dimethylimidazolium Thiocyanate and Tetracyanoborate Ionic Liquids at Anatase (101) Surface.* The Journal of Physical Chemistry C, 2015. **119**(27): p. 15137-15149.
30. De Angelis, F., et al., *Absorption Spectra and Excited State Energy Levels of the N719 Dye on TiO_2 in Dye-Sensitized Solar Cell Models.* The Journal of Physical Chemistry C, 2011. **115**(17): p. 8825-8831.
31. Dette, C., et al., *TiO_2 Anatase with a Bandgap in the Visible Region.* Nano Letters, 2014. **14**(11): p. 6533-6538.
32. Mosconi, E., A. Selloni, and F. De Angelis, *Solvent Effects on the Adsorption Geometry and Electronic Structure of Dye-Sensitized TiO_2: A First-Principles Investigation.* The Journal of Physical Chemistry C, 2012. **116**(9): p. 5932-5940.
33. Pastore, M. and F. De Angelis, *Computational modelling of TiO_2 surfaces sensitized by organic dyes with different anchoring groups: adsorption modes, electronic structure and implication for electron injection/recombination.* Physical Chemistry Chemical Physics, 2012. **14**(2): p. 920-928.
34. De Angelis, F., *Modeling Materials and Processes in Hybrid/Organic Photovoltaics: From Dye-Sensitized to Perovskite Solar Cells.* Accounts of Chemical Research, 2014. **47**(11): p. 3349-3360.
35. De Angelis, F., et al., *First-Principles Modeling of the Adsorption Geometry and Electronic Structure of Ru(II) Dyes on Extended TiO_2 Substrates for Dye-Sensitized Solar Cell Applications.* The Journal of Physical Chemistry C, 2010. **114**(13): p. 6054-6061.

36. Yanai, T., D.P. Tew, and N.C. Handy, *A new hybrid exchange–correlation functional using the Coulomb-attenuating method (CAM-B3LYP).* Chemical Physics Letters, 2004. **393**(1): p. 51-57.
37. Schäfer, A., H. Horn, and R. Ahlrichs, *Fully optimized contracted Gaussian basis sets for atoms Li to Kr.* The Journal of Chemical Physics, 1992. **97**(4): p. 2571-2577.
38. Frisch, M.J., et al., *Gaussian 09, Revision B.01*. 2009, Gaussian, Inc.: Wallingford CT.
39. Momma, K. and F. Izumi, *VESTA 3 for three-dimensional visualization of crystal, volumetric and morphology data.* Journal of Applied Crystallography, 2011. **44**(6): p. 1272-1276.
40. Matsui, M. and M. Akaogi, *Molecular Dynamics Simulation of the Structural and Physical Properties of the Four Polymorphs of* TiO_2. Molecular Simulation, 1991. **6**(4-6): p. 239-244.
41. Luan, B., T. Huynh, and R. Zhou, *Simplified* TiO_2 *force fields for studies of its interaction with biomolecules.* The Journal of Chemical Physics, 2015. **142**(23): p. art. no. 234102.
42. Wu, X., et al., *Molecular dynamics simulations of BSA absorptions on pure and formate-contaminated rutile (110) surface.* Applied Surface Science, 2020. **533**: p. 147574.
43. Hong, H., S.A. Song, and S.S. Kim, *Phase transformation of poly (vinylidene fluoride)/*TiO_2 *nanocomposite film prepared by microwave-assisted solvent evaporation: An experimental and molecular dynamics study.* Composites Science and Technology, 2020. **199**: p. Art. no. 108375.
44. Liu, S., et al., *An In Silico study of* TiO_2 *nanoparticles interaction with twenty standard amino acids in aqueous solution.* Scientific Reports, 2016. **6**: p. Art. no. 37761.
45. Van Der Spoel, D., et al., *GROMACS: Fast, Flexible, and Free.* Journal of Computational Chemistry, 2005. **26**(16): p. 1701-1718.
46. Malali, S. and M. Foroutan, *Study of Wetting Behavior of* $BMIM^+/PF_6^-$ *Ionic Liquid on* TiO_2 *(110) Surface by Molecular Dynamics Simulation.* The Journal of Physical Chemistry C, 2017. **121**(21): p. 11226-11233.
47. Singh, R., et al., *Molecular dynamics simulations of the ionic liquid* $[EMIM^+][TFMSI^-]$ *confined inside rutile (110) slit nanopores.* Physical Chemistry Chemical Physics, 2013. **15**(38): p. 16090-16103.
48. Yan, T., et al., *Adsorption of* CO_2 *on the Rutile (110) Surface in Ionic Liquid. A Molecular Dynamics Simulation.* The Journal of Physical Chemistry C, 2009. **113**(45): p. 19389-19392.
49. Marekha, B.A., et al., *Local Structure in Terms of Nearest-Neighbor Approach in 1-Butyl-3-methylimidazolium-Based Ionic Liquids: MD Simulations.* The Journal of Physical Chemistry B, 2016. **120**(22): p. 5029-5041.
50. Mondal, A. and S. Balasubramanian, *Quantitative Prediction of Physical Properties of Imidazolium Based Room Temperature Ionic Liquids through Determination of Condensed Phase Site Charges: A Refined Force Field.* The Journal of Physical Chemistry B, 2014. **118**(12): p. 3409-3422.
51. Canongia Lopes, J.N., A.A.H. Pádua, and K. Shimizu, *Molecular Force Field for Ionic Liquids IV: Trialkylimidazolium and Alkoxycarbonyl-Imidazolium Cations; Alkylsulfonate and Alkylsulfate Anions.* The Journal of Physical Chemistry B, 2008. **112**(16): p. 5039-5046.
52. Bussi, G., D. Donadio, and M. Parrinello, *Canonical Sampling through Velocity Rescaling* Journal of Chemical Physics, 2007. **126**(1): p. 014101.
53. Darden, T., D. York, and L. Pedersen, *Particle mesh Ewald: An N x log(N) method for Ewald sums in large systems.* The Journal of Chemical Physics, 1993. **98**(12): p. 10089-10092.

54. Abraham, M.J., et al., *GROMACS: High performance molecular simulations through multi-level parallelism from laptops to supercomputers.* SoftwareX, 2015. **1–2**: p. 19-25.
55. Humphrey, W., A. Dalke, and K. Schulten, *VMD: Visual Molecular Dynamics.* Journal of Molecular Graphics, 1996. **14**(1): p. 33-38.
56. Oprea, I.C. and A.M. Gîrțu, *Structure and Electronic Properties of TiO_2 Nanoclusters and Dye–Nanocluster Systems Appropriate to Model Hybrid Photovoltaic or Photocatalytic Applications.* Nanomaterials, 2019. **9**(3): p. art. no. 357.
57. Oprea, C.I., et al., *DFT Study of Binding and Electron Transfer from a Metal-Free Dye with Carboxyl, Hydroxyl, and Sulfonic Anchors to a Titanium Dioxide Nanocluster.* International Journal of Photoenergy, 2013. **2013**: p. 893850.
58. Smortsova, Y., et al., *Solvatochromic effects on a class of indoline derivatives organic photosensitizers: About the influence of hydrogen-bond acceptor and donor abilities parameters.* Journal of Molecular Liquids, 2017. **245**: p. 76-84.
59. El-Zohry, A.M., *The origin of slow electron injection rates for indoline dyes used in dye-sensitized solar cells.* Dyes and Pigments, 2019. **160**: p. 671-674.
60. Matsui, M., et al., *Effects of alkyl-, polyfluoroalkyl-, and perfluoroalkyl carboxylic acids on the performance of D205 in dye-sensitized solar cells.* Journal of Photochemistry and Photobiology A: Chemistry, 2017. **348**: p. 134-138.
61. Le Bahers, T., et al., *A TDDFT investigation of ground and excited state properties in indoline dyes used for dye-sensitized solar cells.* Physical Chemistry Chemical Physics, 2009. **11**(47): p. 11276-11284.
62. Kyrychenko, A. and B. Albinsson, *Conformer-dependent electronic coupling for long-range triplet energy transfer in donor-bridge-acceptor porphyrin dimers.* Chemical Physics Letters, 2002. **366**(3-4): p. 291-299.
63. Pettersson, K., et al., *Singlet energy transfer in porphyrin-based donor-bridge-acceptor systems: Interaction between bridge length and bridge energy.* Journal of Physical Chemistry A, 2006. **110**(1): p. 310-318.
64. Pastore, M., et al., *A Computational Investigation of Organic Dyes for Dye-Sensitized Solar Cells: Benchmark, Strategies, and Open Issues.* The Journal of Physical Chemistry C, 2010. **114**(15): p. 7205-7212.
65. Ali, A., et al., *TDDFT benchmark for UV-visible spectra of fused-ring electron acceptors using global and range-separated hybrids.* Physical Chemistry Chemical Physics, 2020. **22**(15): p. 7864-7874.
66. Jungsuttiwong, S., et al., *Theoretical study on novel double donor-based dyes used in high efficient dye-sensitized solar cells: The application of TDDFT study to the electron injection process.* Organic Electronics, 2013. **14**(3): p. 711-722.
67. Lambert, C., et al., *Characterization of high-performance organic dyes for dye-sensitized solar cell: a DFT/TDDFT study.* Canadian Journal of Chemistry, 2016. **94**(12): p. 1109-1118.
68. Akimov, A.V., A.J. Neukirch, and O.V. Prezhdo, *Theoretical Insights into Photoinduced Charge Transfer and Catalysis at Oxide Interfaces.* Chemical Reviews, 2013. **113**(6): p. 4496-4565.
69. Duncan, W.R. and O.V. Prezhdo, *Theoretical Studies of Photoinduced Electron Transfer in Dye-Sensitized TiO_2.* Annual Review of Physical Chemistry, 2007. **58**(1): p. 143-184.
70. Ji, X. and H. Adidharma, *Thermodynamic modeling of ionic liquid density with heterosegmented statistical associating fluid theory.* Chemical Engineering Science, 2009. **64**(9): p. 1985-1992.
71. Sambasivarao, S.V. and O. Acevedo, *Development of OPLS-AA Force Field Parameters for 68 Unique Ionic Liquids.* Journal of Chemical Theory and Computation, 2009. **5**(4): p. 1038-1050.

72. Zhou, G. and L. Huang, *A review of recent advances in computational and experimental analysis of first adsorbed water layer on solid substrate.* Molecular Simulation, 2020: p. doi: 10.1080/08927022.2020.1786086.
73. Widegren, J.A. and J.W. Magee, *Density, Viscosity, Speed of Sound, and Electrolytic Conductivity for the Ionic Liquid 1-Hexyl-3-methylimidazolium Bis(trifluoromethylsulfonyl)imide and Its Mixtures with Water.* Journal of Chemical & Engineering Data, 2007. **52**(6): p. 2331-2338.
74. Qiao, Y., et al., *Densities and Viscosities of [Bmim][PF$_6$] and Binary Systems [Bmim][PF$_6$] + Ethanol, [Bmim][PF$_6$] + Benzene at Several Temperatures and Pressures: Determined by the Falling-Ball Method.* Journal of Chemical & Engineering Data, 2011. **56**(5): p. 2379-2385.
75. Fredlake, C.P., et al., *Thermophysical Properties of Imidazolium-Based Ionic Liquids.* Journal of Chemical & Engineering Data, 2004. **49**(4): p. 954-964.
76. Moumouzias, G., D.K. Panopoulos, and G. Ritzoulis, *Excess properties of the binary liquid system propylene carbonate + acetonitrile.* Journal of Chemical & Engineering Data, 1991. **36**(1): p. 20-23.
77. Vaissier, V., et al., *How mobile are dye adsorbates and acetonitrile molecules on the surface of TiO_2 nanoparticles? A quasi-elastic neutron scattering study.* Scientific Reports, 2016. **6**(1): p. 39253.
78. Schiffmann, F., J. Hutter, and J. VandeVondele, *Atomistic simulations of a solid/liquid interface: a combined force field and first principles approach to the structure and dynamics of acetonitrile near an anatase surface.* Journal of Physics: Condensed Matter, 2008. **20**(6): p. art. no. 064206.
79. Kislenko, S.A., R.H. Amirov, and I.S. Samoylov, *Effect of Cations on the TiO_2/Acetonitrile Interface Structure: A Molecular Dynamics Study.* The Journal of Physical Chemistry C, 2013. **117**(20): p. 10589-10596.
80. Ham, H.W. and Y.S. Kim, *Theoretical study of indoline dyes for dye-sensitized solar cells.* Thin Solid Films, 2010. **518**(22): p. 6558-6563.
81. Fakis, M., et al., *A time resolved fluorescence and quantum chemical study of the solar cell sensitizer D149.* Dyes and Pigments, 2013. **96**(1): p. 304-312.
82. Ma, T., et al., *Effect of functional group on photochemical properties and photosensitization of TiO_2 electrode sensitized by porphyrin derivatives.* Journal of Photochemistry and Photobiology A: Chemistry, 2002. **152**(1): p. 207-212.
83. Agrawal, S., et al., *Modeling the effect of ionic additives on the optical and electronic properties of a dye-sensitized TiO_2 heterointerface: absorption, charge injection and aggregation.* Journal of Materials Chemistry A, 2013. **1**(46): p. 14675-14685.
84. Krukau, A.V., et al., *Influence of the exchange screening parameter on the performance of screened hybrid functionals.* The Journal of Chemical Physics, 2006. **125**(22): p. 224106.

Conclusions and perspectives

In this thesis the theoretical investigation of dyes was performed. In the case, when it is necessary to carry out virtual screening, the PPP/CIS and ZINDO methods can provide the necessary information at the cost of a small computer resources. Among the all TDDFT method, the results of the B3LYP and CAM-B3LYP methods give the upper and lower limits of the absorption wavelength, respectively. However, the results, obtained with the method M06-2X is still reliable and close to B3LYP. Additionally, to this, the absorbance spectrum of D205 dye was calculated on the different level of theory. It was shown that only the atomic basis set with the diffusion functions can reproduce the experimental shape of the spectrum. As a result of virtual screening 6 new dye molecules were proposed as a promising candidate for the further synthesis and using in DSSC.

In the Chapter 2 with the quantum-chemical method the force field for dye D205 was parametrized. It was shown that there is a big change in the HOMO-LUMO structure and due to this it is necessary to calculate and analyze both ground and excited states. Electron density move from donor part in ground state to acceptor in excited state. The difference in dipole moments and consequently partial charges between excited state with geometry, optimized in ground state and excited state with geometry relaxation is tiny, so it is possible to use geometry, obtained on ground state. From the result of MD simulation D205 in the mixture of $BmimBF_4$ and AN for the range of molar fraction 0-1 there is noticeable, that interaction between electronegative atoms of D205 and selected atoms H of Bmim is weaker than between cation and anion of IL. However, these atoms can interact with AN. It was presented that in the case of acetonitrile the difference between local structure in ground and excited states observed, while for the pure $BmimBF_4$ the shape of rdf for the 1st neighbor is similar. For the chain and donor part the equiprobable interactions occurs near the mole fraction 0.4, while in 0.5 the distance between D205 and BF_4 less than for D205 and acetonitrile. For the bridge part in 0.5 the interaction with AN stronger, that with anion.

Finally, the TDDFT studies and MD simulation of D205 on the $Ti_{30}O_{62}H_4$-anatase nanoparticle surface were performed. It was determined that anchoring of the D205 to a TiO_2 nanoparticle induces an 860 cm^{-1} redshift of its long-wavelength band, as calculated by the TD-CAM-B3LYP/TZV approach using the PCM model of the acetonitrile solution. MD simulations in pure AN revealed that the polar environment affects conformational dynamics of the TiO_2-anchored D205 dye. These environment-induced conformational changes effect to solvatochromic shifts in UV-vis absorption spectra of the D205 dye. The analysis of the excited-state properties and electronic structure of a free D205 dye and a $Ti_{30}O_{62}H_4$ nanoparticle revealed that the alignment between HOMO and LUMO energy levels of the dye and the semiconductor suggests the favorable driving force for photoinduced dye-to-TiO_2 electron transfer. It was found that counterions of $BmimPF_6$ and BmimTFO, and molecules of polar AN interact strongly with polar TiO_2 anatase (001) surface to form the well-ordered interfacial region composed of up to three solvent layers. MD simulations revealed that the densely ordered layers of the adsorbed IL cations and AN molecules shield the direct contact of the TiO_2-anchored D205 chromophore with the TiO_2 surface. The most conformationally labile fragments of the D205 dye were localized at the octyl tail and peripheral diaryl-substituted ethylene moiety. Control MD simulations of adsorption of a free dye revealed that the D205 dye molecule prefers binding onto TiO_2.

In perspectives, the work presented in this thesis can be the cause of these further developments:

- The methodology used for the developing new potential models for the D205 used in this work may be applied for the organic dye molecules, in particular indoline ones (e.g. D102, D149, etc) both in mixture and on TiO_2.

- The local structure analysis of the MD simulation results in the terms of NNA can be used for the analysis D205 in other solutions, especially combination, which consist of IL and molecular solvent.
- The proposed method of finding “hits” with the further analysis can be applied for the wider library of different compounds with the aim to choose the molecules with requested properties, not only absorption spectra. It can be useful for the molecular design of new compound before its synthesis.
- MD simulation and TDDFT analysis of dyes on another surfaces or nanoparticles, like ZnO, in ternary systems containing IL-molecular solvent mixtures and dye molecules as electrolytes for dye-sensitized solar cells. The microscopic environment, in terms of its polarity, viscosity and possible specific intermolecular interactions, can significantly alter the photodynamics of the dye molecule which is, in turn, reflected in the performance of the entire device.

Appendices

Appendix A

Table A1. Comparison of the partial charges in ground (S0) and excited (S1) states of dye D205, ordered by the biggest S1-S0 difference.

#	Atom	S0	S1	S1-S0
51	C	0,203947	0,287585	0,084
67	C	-0,03464	0,0441	0,079
66	S	-0,14419	-0,09067	0,054
49	N	-0,48918	-0,44391	0,045
61	C	-0,04915	-0,00975	0,039
80	C	-0,00579	0,028249	0,034
26	C	0,137303	0,170258	0,033
12	C	-0,20767	-0,18552	0,022
75	S	-0,10966	-0,08969	0,020
30	C	-0,26916	-0,25622	0,013
52	C	-0,07814	-0,06755	0,011
74	C	-0,20866	-0,19847	0,010
60	H	0,128439	0,13836	0,010
38	H	-0,02514	-0,01551	0,010
48	H	-0,03491	-0,02543	0,009
44	H	0,050379	0,058419	0,008
45	C	0,011194	0,019206	0,008
56	H	0,12574	0,13328	0,008
31	C	-0,22657	-0,21904	0,008
39	C	0,000269	0,007778	0,008
95	C	-0,1029	-0,09585	0,007
89	C	-0,05387	-0,04731	0,007
6	C	-0,13909	-0,13308	0,006
43	H	0,014305	0,019886	0,006
46	H	0,007441	0,012885	0,005
14	C	-0,12045	-0,11502	0,005
32	H	0,051524	0,056608	0,005
33	H	0,117092	0,122144	0,005
20	H	0,00569	0,010668	0,005
58	H	0,146085	0,150659	0,005
40	H	-0,00196	0,002561	0,005
41	H	0,010867	0,015243	0,004
25	H	0,085242	0,089416	0,004
7	C	-0,15819	-0,15456	0,004
47	H	-0,00382	-0,00049	0,003
17	C	-0,11519	-0,11238	0,003
11	H	0,109824	0,112317	0,002
83	C	-0,06614	-0,06372	0,002
35	H	0,125807	0,128161	0,002
99	H	-0,0891	-0,08707	0,002

Table A1. Comparison of the partial charges in ground (S0) and excited (S1) states of dye D205, ordered by the biggest S1-S0 difference.

18	C	-0,1065	-0,10454	0,002
2	C	-0,16721	-0,16528	0,002
8	H	0,112792	0,114525	0,002
19	H	0,094682	0,096385	0,002
9	H	0,106676	0,108329	0,002
3	C	-0,09283	-0,09119	0,002
73	H	0,433233	0,434722	0,001
88	H	0,024108	0,02558	0,001
10	H	0,054642	0,056018	0,001
22	H	0,104312	0,105591	0,001
23	H	0,101544	0,102703	0,001
21	H	0,116355	0,117038	0,001
90	H	0,014838	0,015163	0,000
76	C	0,187739	0,188005	0,000
101	C	-0,27307	-0,27283	0,000
93	H	-0,01921	-0,01925	0,000
34	H	0,145286	0,14506	0,000
94	H	0,010347	0,009894	0,000
103	H	0,05687	0,05636	-0,001
27	C	0,339361	0,338851	-0,001
104	H	0,048015	0,047444	-0,001
100	H	-0,05309	-0,05368	-0,001
50	C	0,289936	0,28917	-0,001
91	H	0,021032	0,01994	-0,001
15	C	-0,12079	-0,12193	-0,001
85	H	0,021422	0,020145	-0,001
97	H	0,011261	0,009857	-0,001
102	H	0,058312	0,056833	-0,001
5	C	-0,11389	-0,11565	-0,002
1	H	0,064727	0,062862	-0,002
87	H	0,022929	0,021029	-0,002
84	H	0,021782	0,01955	-0,002
96	H	0,017379	0,014833	-0,003
98	C	0,299009	0,296303	-0,003
13	C	0,138952	0,136082	-0,003
72	O	-0,64167	-0,64509	-0,003
54	C	-0,19834	-0,20177	-0,003
53	C	-0,20871	-0,21225	-0,004
16	C	-0,06078	-0,06453	-0,004
92	C	0,021697	0,0168	-0,005
28	C	-0,08113	-0,08702	-0,006
82	H	0,057466	0,05045	-0,007
29	C	-0,13511	-0,14217	-0,007
81	H	0,03899	0,031182	-0,008
37	C	0,172488	0,164611	-0,008

Table A1. Comparison of the partial charges in ground (S0) and excited (S1) states of dye D205, ordered by the biggest S1-S0 difference.

70	C	0,816254	0,807586	-0,009
71	O	-0,58668	-0,5962	-0,010
57	H	0,203241	0,193243	-0,010
86	C	0,051518	0,039949	-0,012
42	C	-0,11215	-0,12373	-0,012
4	C	0,42904	0,415627	-0,013
36	C	0,283984	0,269342	-0,015
68	H	0,088574	0,073331	-0,015
105	N	-0,12454	-0,14024	-0,016
24	C	-0,16546	-0,18615	-0,021
69	H	0,08638	0,064832	-0,022
65	C	0,187893	0,163937	-0,024
55	C	-0,26213	-0,28971	-0,028
78	C	0,56501	0,535086	-0,030
79	O	-0,45013	-0,4813	-0,031
77	S	-0,25482	-0,28877	-0,034
62	C	0,513482	0,477705	-0,036
63	O	-0,50036	-0,53967	-0,039
64	N	-0,12189	-0,16521	-0,043
59	C	-0,18068	-0,30037	-0,120